CAPACITY AND SIGNALING FOR FREE-SPACE OPTICAL CHANNELS

CAPACITY AND SIGNALING FOR FREE-SPACE OPTICAL CHANNELS

By

Ahmed A. Farid Youssef

2009

A Thesis

Submitted to the Department of Electrical & Computer Engineering

and the School of Graduate Studies

of McMaster University

in Partial Fulfilment of the Requirements

for the Degree of

Doctor of Philosophy

McMaster University

DOCTOR OF PHILOSOPHY (2009) McMaster University

(Electrical & Computer Engineering) Hamilton, Ontario, Canada

TITLE:	Capacity and Signaling for Free-Space Optical Channels
AUTHOR:	Ahmed A. Farid Youssef B.Sc. (Electrical Engineering), M.Sc. (Electrical Engineering), Alexandria University, Alexandria, Egypt M.A.Sc. (Electrical Engineering), McMaster University, Hamilton, Canada.
SUPERVISOR:	Steve Hranilovic, Associate Professor
NUMBER OF PAGES:	xxiii, 194

Dedications

To my parents

My wife

My son and daughter.

Abstract

Wireless optical communication systems have the potential of establishing secure high data rate communication links. In order to realize the ultimate promise of these links, channel modeling and communication algorithms must be developed. This thesis addresses free-space optical (FSO) system design and provides novel contributions in four major areas: 1) channel modeling, 2) channel capacity and optimal signal design, 3) signaling algorithms, and 4) formal methods to jointly design code rate and beamwidth for FSO systems.

A novel statistical channel model taking into account atmospheric and misalignment fading is developed that generalizes the existing models and accounts for transmitter beamwidth. The channel capacity is analyzed under average and peak optical power constraints and a new class of non-uniform discrete input distributions are developed with mutual information that closely approaches the channel capacity. Algorithms to realize the proposed non-uniform signaling and achieve the promising rates are also presented. Numerical simulations are conducted with finite length low density parity check codes showing significant improvement in system performance. Finally, the developed signaling is applied to FSO channels considering the above impairments. Beamwidth optimization is considered to maximize the channel capacity subject to outage. It is shown that a rate gain of 80% can be achieved with beamwidth optimization.

Acknowledgements

This thesis would not have been possible without the support, guidance and contributions of many individuals. I would like to express my gratitude and deep thanks to them, however, this will not be enough to give them the full merit of their contributions.

First, I would like to express my sincere gratitude to my advisor Dr. Steve Hranilovic for his consistent guidance, encouragement, support and insightful discussions throughout this thesis. His knowledge and logical thinking have been of great value. His insight and logical discussions have led the work through all the difficulties, and solved many problems when a deadline is approaching soon!.

I would also like to express my appreciation to Dr. T. N. Davidson for his valuable comments and discussions. I am also grateful to Dr. Shiva Kumar for his insightful comments and valuable suggestions. In addition, I want to thank the staff in the ECE department and in particular Cheryl Gies who always helped me.

I owe a huge debt of gratitude to my professors at Alexandria University and McMaster University for all that I have learned from them during my B.Sc., M.Sc., M.A.Sc, and Ph.D. studies. Specifically, I would like to express my gratitude to Prof. Said El-Khamy, my M.Sc. supervisor, for his guidance and support both on academic and non-academic matters. He contributed greatly towards building my background .

I would also like to thank the family and friends I have found in Canada. Their help and support made me feel at home from the first day. I owe too much to Canada which provides me the chance to learn and enjoy life.

I would like to dedicate sincere feelings of devotion to my wonderful country Egypt.

I would like to express may sincere and deep thanks to my father and mother for their love and endless support through my life.

Finally, I am very grateful to my wife who was always there when I needed her support and encouragement. Thanks to my son, Youssef, and my daughter, Malak, who made my life full of happiness.

List of Acronyms

BAC	Binary asymmetric channel
BER	Bit-error rate
CSI	Channel state information
DD	Direct detection
EPI	Entropy power inequality
FSO	Free-space optical
Gbps	Gigabits per second
IM	Intensity modulation
LDPC	Low density parity check
LOS	Line-of-sight
Mbps	Megabits per second
MLC	Multi-level coding
MSD	Multi-stage decoding
NMSE	Normalized mean square error
OOK	On-off keying
PAM	Pulse amplitude modulation
PAR	Peak-to-average ratio
pdf	Probability density function
PPM	Pulse position modulation
RF	Radio frequency
SNR	Signal-to-noise ratio

List of Notations

a	detector radius	$\langle\cdot\rangle$	ensemble average
a_k	the k^{th} mass point amplitude	2^N	number of quantization levels
A	peak optical power	P	average optical power
$\mathcal{B}_n$	n-dimensional unit ball	$P_{\text{out}}(R_0)$	probability of outage at R_0
C_n	refractive-index structure parameter	$q_\ell(x)$	maxentropic distribution
C_{L}	capacity lower bound	r	radial displacement
C_{U}	capacity upper bound	R_0	code rate
$\mathcal{C}(h)$	instantaneous capacity at h	R_v	responsivity
$\mathbb{E}\{\cdot\}$	expectation operator	$V(\cdot)$	volume
$f_{H_{\text{a}}}(\cdot)$	pdf of atmosphere	w_o	beam waist at transmitter
$f_{H_{\text{p}}}(\cdot)$	pdf of misalignment	w_z	beam waist at receiver
$f_H(h)$	pdf of optical channel	$\boldsymbol{W}$	input vector to mapper
$f_X(x)$	input distribution	$x(t)$	transmitted optical intensity
F_o	radius of curvature	X	discrete time intensity
$h(t)$	channel gain	$y(t)$	photodetector current
h_ℓ	attenuation factor	Y	discrete time current
H_{a}	atmospheric fading	z	optical link range
H_{p}	misalignment fading	Z	discrete time noise
H	discrete channel gain	η	optics efficiency
$\mathbb{H}(X)$	discrete source entropy	λ	wavelength
$I(r,z)$	optical intensity	σ^2	noise variance
$\mathbb{I}(X;Y)$	mutual information	σ_{R}^2	Rytov variance
k	wave number	$\sigma_{I_{\text{a}}}^2$	scintillation index
$K+1$	number of mass points	σ_s^2	misalignment (sway) variance
ℓ	mass points spacing	ν	attenuation coefficient
$\mathcal{M}$	mapper function	ϕ	weather condition
$n(t)$	Gaussian noise	$\Phi(P,\varrho)$	outer parallel body
$\mathcal{N}(\mathrm{v},\zeta^2)$	Gaussian dist. mean=v, variance=ζ^2	$\Psi(P)$	regular n-simplex

Contents

Abstract v

Acknowledgements vii

List of Acronyms x

List of Notations xii

List of Tables xvii

List of Figures xxiii

1 Introduction 1

1.1 Wireless Optical Systems 6

1.2 System Model and Definitions 8

1.3 Channel Fading and Attenuation 10

1.3.1 Atmospheric Turbulence Fading 12

1.3.2 Misalignment Fading (Jitter) 13

1.4 Channel Capacity 14

1.4.1 Input Signal Constraints 15

1.4.2 Channel Capacity: Average Power Constraint 16

1.4.3 Channel Capacity: Peak and Average Power Constraints . . . 18

1.5 Signaling Design and Implementation 20
1.6 Thesis Contributions 22
1.7 Thesis Structure 24

2 Statistical Channel Model: Atmosphere and Misalignment 27

2.1 Gaussian-Beam Wave 28
2.2 Atmosphere and Irradiance Fluctuations 30
2.3 Irradiance Statistical Models Overview 33
2.3.1 Log-normal density function 35
2.3.2 Gamma-Gamma density function 36
2.4 Gaussian-Beam Wave Parameters 38
2.4.1 Gaussian Beam Off-axis Statistics 39
2.5 Atmospheric Attenuation 41
2.6 Misalignment Fading 43
2.7 Channel Statistical model 47
2.8 Conclusion 48

3 Capacity Bounds Under an Average Optical Power Constraint 49

3.1 Introduction 50
3.2 Channel Capacity Lower Bound 51
3.3 Channel Capacity Upper Bound 55
3.3.1 Set of Received Codewords and Volumes 55
3.3.2 Volume Approximation 58
3.3.3 Uniqueness of α^* 61
3.4 Results 63
3.4.1 Capacity Bounds: Discussion and Comparisons 63
3.4.2 Discussions on the Lower Bound 65
3.4.3 Interpretations for the Upper Bound 68

3.5 Conclusion 71

4 **Channel Capacity with Peak and Average Optical Power Constraints** **73**

4.1 Introduction 74

4.2 Channel Capacity 75

4.3 Capacity-Approaching Distributions 76

4.3.1 Definition of Distributions 77

4.3.2 Estimate of $\bar{K}(\rho, \mathrm{SNR})$ 79

4.3.2.1 Interpretation of the Estimate $\hat{K}$ 81

4.3.3 Channel Capacity and Information Rates 82

4.3.4 Input Distributions and Numbers of Mass Points 88

4.4 Mutual Information Behavior for Different ρ 91

4.5 Conclusion 93

5 **Coding for Optical Channels: Non-Uniform Distributions** **95**

5.1 Introduction 96

5.2 Generating Non-uniform Distribution 98

5.3 Coding Scheme for Optical Channel 99

5.4 The Mapper and the Equivalent Channel 102

5.5 Quantized-Level Distributions 104

5.5.1 Average Power Constraint 105

5.5.1.1 Mutual Information of Quantized-levels distributions 106

5.5.1.2 Non-uniform Signaling Algorithm 109

5.5.2 Peak and Average Power Constraints 112

5.5.2.1 Channel Capacity and Mutual Information 115

5.5.2.2 Number of Mass Points 118

5.5.2.3 Algorithm Performance 119

5.6 Conclusion 124

6 **Capacity and Outage for Fading FSO Channels** **125**

6.1 Introduction 126

6.2 Outage Capacity 127

6.3 FSO Link Design Criteria 129

6.4 Weather and System Parameters 131

6.5 Uniform Signaling and Outage Capacity 134

6.5.1 Probability of Outage 134

6.5.2 Probability of Outage and Achievable Rates 137

6.6 Non-Uniform Signaling and Outage Capacity 141

6.6.1 Average Power Constraint 141

6.6.2 Peak and Average Power Constraints 146

6.7 Conclusion 151

7 **Conclusions and Future Directions** **153**

7.1 Conclusion 153

7.2 Future Directions 155

Appendices **161**

A $h_p(r)$ **Approximation** **161**

B Upper Bound on γ_m **163**

C Erfc(x**) Lower Bound** **167**

D Limit of $\phi(\alpha, n)$ **171**

E Limit of the Supremum **175**

F Uniqueness of the root t_0 **177**

List of Tables

2.1 Atmospheric attenuation for different weather conditions 42

2.2 Normalized mean square error (NMSE) between exact and approximate h_{p} expressions 46

4.1 Number of mass points in the input distribution that maximizes the mutual information when $\rho = 4$ 89

5.1 Optimum Distribution and Peak Amplitudes for $M = 2$ and $N = 4$. 108

5.2 Input distribution $2^N = 4$ quantization levels 119

5.3 Input distribution $2^N = 8$ quantization levels 119

6.1 Weather parameters 132

6.2 System Parameters 133

List of Figures

1.1 Free-space optical (FSO) system topology as a solution for the last-mile connectivity problem. 3

1.2 Wireless optical channel. 7

1.3 FSO channel fading impairments. 11

2.1 Gaussian-beam wave with effective beam radius w_o at the transmitter aperture ($z = 0$) and different radius of curvature, (a) convergent beam ($F_o > 0$), (b) collimated beam ($F_o = \infty$), and (c) divergent beam ($F_o < 0$). 29

2.2 Optical wave propagation through turbulence cells. 32

2.3 Relative deviation of scintillation index versus displacement from the beam centre for different turbulence strengths over a propagation distance $z = 1000$ m. 40

2.4 Detector and beam footprint with misalignment at the detector plane. 44

2.5 Exact and approximate values of $h_{\mathrm{p}}(d, z)$ for different values of w_z/a versus the normalized radial displacement d/a. 45

3.1 (a) 2-D representation of an n-simplex and its parallel body at distance ϱ, (b) 3-D illustrative diagram for sphere packing in the volume $\Phi(P, \varrho)$. 57

3.2 Average power constraint. Capacity bounds C_{L} and C_{U} and mutual information for continuous exponential [60], and discrete uniform PAM. For comparison, previously reported upper bounds $H\&K_{\mathrm{U}}$ [60, Eqn. (21)], M_{U1} [61, Eqn. (3.27)], M_{U2} [62, Eqn. (28)] and lower bound M_{L} [61, Eqn. (3.26)] are also presented. 64
3.3 The optimum β^* and the corresponding optimum mass point spacing, ℓ^*, for $P = 0.5, 1, 2$ and $h = 1$ versus SNR. 66
3.4 The proposed discrete distribution at different SNR for average optical power constraint P=1. 69
3.5 The optimum α^* for the capacity upper bound versus SNR. 70
4.1 Normalized spacing ℓ/σ versus ρ at transition SNRs between $\bar{K}+1 \rightarrow \bar{K}+2$ mass points in $\bar{q}_X^*(x;\bar{K})$. 80
4.2 Peak and average power constraints. Channel capacity and mutual information for the maxentropic input distributions (4.8) with different number of mass points versus SNR for $\rho = 2$. 83
4.3 Peak and average power constraints. Channel capacity and mutual information for the maxentropic input distributions (4.8) with different number of mass points versus SNR for $\rho = 4$. 84
4.4 Peak and average power constraints. Channel capacity and mutual information for the maxentropic input distributions (4.8) with different number of mass points versus SNR for $\rho = 6$. 85
4.5 Peak and average power constraints. Channel capacity and mutual information for the proposed input distribution with K and $\hat{K}$ and the uniform input distributions for $\rho = 4$. 87
4.6 The optimum, $f_X^*(x)$ (4.3), and the proposed input distributions, $\bar{q}_X^*(x,\bar{K})$ (4.6), for different SNRs at $\rho = 4$. 90

4.7 Peak and average power constraints. Mutual information versus SNR for different ρ using the input distribution $\bar{q}_X^*(x;\bar{K})$ in (4.6). 92

5.1 Illustrative diagram for optical channels including mapper 98

5.2 Schematic block diagram for multilevel coding (MLC) and mapping scheme for optical intensity channels with non-uniform channel input distribution. 101

5.3 Schematic block diagram for multi-stage decoders (MSD). 101

5.4 Mapping function over $\mathcal{X} = \{0,1\}$ to induce $p(0) = 7/8$ 103

5.5 Equivalent Z-Channel seen by W_1 when $N = 3$ and $p(0) = 7/8$ 103

5.6 Equivalent Channel between W_1 and Y 103

5.7 Equivalent channel for the mapper as seen by the individual bit W_i. . 104

5.8 Average power constraint. Upper, $H\&K_{\mathrm{U}}$ and C_{U} (3.18), and lower, C_{L} (3.7), bounds on the channel capacity and the mutual information using the quantized-level distributions for $N = 2, 3$ and 4 encoders, i.e., 4-, 8-, and 16-quantization levels respectively. 107

5.9 Average power constraint. The mutual information versus SNR for each sub-channel in the MLC system using $N = 3$ encoders to generate input distribution $\{q_0, q_1\} = \{7/8, 1/8\}$. The rates are given by $R_1 = \mathbb{I}(W_1;Y)$, $R_2 = \mathbb{I}(W_2;Y|W_1)$ and $R_3 = \mathbb{I}(W_3;Y|W_1,W_2)$. 110

5.10 Average power constraint. BER and FER for MLC system using LDPC codes with rate $R_1 = R_2 = 0.05$ and $R_3 = 0.12$. The Shannon limit for both the uniform 2-PAM and the non-uniform distributions with $N = 3$ is shown. 111

5.11 Peak and average power constraints. Channel capacity and mutual information for the M-ary uniform and the quantized input distribution with 4- and 8-quantization levels for $\rho = 4$. 116

5.12 Peak and average power constraints. Mutual information using, the maxentropic input distribution $\bar{q}_X^*(x;K)$ (4.6), the 8-quantized level distribution in $\breve{\mathcal{Q}}^3$, and the 8-quantized level distribution in $\tilde{\mathcal{Q}}^3$ for $\rho = 4$. 117

5.13 Peak and average power constraints. Number of mass points versus SNR at 4- and 8- quantization levels. The number of mass points using the maxentropic input distribution $\bar{q}_X^*(x,K)$ with real valued amplitudes is also shown $\rho = 4$. 120

5.14 Peak and average power constraints. Sub-channels rate for the MLC system using two mass points with probabilities $\left[\frac{3}{4},\frac{1}{4}\right]$ at $\rho = 4$. . . . 122

5.15 Peak and average power constraints. The optimum and the proposed input distribution for different SNRs with $\rho = 4$. 123

6.1 P_{out} versus P for clear weather and $R_0 = 0.5$ bits/ch. use. 135

6.2 Beamwidth versus P for clear weather and $R_0 = 0.5$ bits/ch. use. . . 135

6.3 P_{out} versus P for light fog and $R_0 = 0.5$ bits/ch. use. 136

6.4 Beamwidth versus P for light fog and $R_0 = 0.5$ bits/ch. use. 136

6.5 Probability of outage versus achievable rate for nominal ($w_o = 2$ cm) and optimum beamwidths for light fog using uniform OOK. A variety of error control codes with rate k/n are applied to this channel where k bits are sent per codeword of length n symbols and the performance presented at BER=10^{-6}. Hardware implemented Turbo[1] codes with $R_0 = \{1/4, 1/3\}$ and $k = 8920$ [126]. LDPC[2] and Turbo[2] with rate 1/2 and $n = 10^4$ [127]. Hardware implementation for LDPC[3] with $R_0 = 1/2$ and $k = 4096$ [132]. LDPC[4] [129] and LDPC[5] of code rate 0.75 [130]. High rate Reed-Solomon codes RS[6] with $R_0 = 0.874$ and 0.937 [128]. LDPC[7] with $k = 1024$ [131]. 139

6.6 Optimum beamwidth, w_o^{opt}, versus rate, R_0, for light fog weather condition where w_o varies from 1 to 3 cm. 140

6.7 Average power constraint. Probability of outage P_{out} versus rate R_0 in bits/channel use for light fog weather condition. The non-uniform distribution with $M = 2$ mass points and $2^N = 4$ and 32 quantization levels are presented in addition to uniform 2-PAM. Optimum beamwidth is considered in the analysis. 143

6.8 Average power constraint. Probability of outage P_{out} versus rate R_0 in bits/channel use for clear weather condition. The non-uniform distribution with $M = 2$ mass points and $2^N = 4$ and 32 quantization levels are presented in addition to uniform 2-PAM. Optimum beamwidth is considered in the analysis. 144

6.9 Average power constraint. Beamwidth versus P_{out} for light fog weather. 145

6.10 Average power constraint. Beamwidth versus P_{out} for clear weather. 145

6.11 Peak and average power constraints with $\rho = 4$. Probability of outage versus rate, R_0, for uniform 2-PAM distribution, non-uniform $\bar{q}^*(x; \bar{K})$ (4.6), quantized distribution $\tilde{q}^*(x; \tilde{K})$ (5.5), and the capacity bounds for light fog weather condition. 149

6.12 Peak and average power constraints with $\rho = 4$. Beamwidth versus P_{out} for light fog weather condition. 150

C.1 A plot for $g(x)$ versus x. For a given $s > \sqrt{e/2\pi}$ two roots x_1 and x_2 exist. 169

Chapter 1

Introduction

Telecommunications has witnessed a tremendous expansion in network size and a rapid increase in data rate in the last few years. The increasing demand to deliver high data rate services to users leads the revolution to exploit reliable and cost-effective technologies that can be deployed to deliver various types of services. Wireless optical communication has been introduced as a promising technology that can be of great benefit in telecommunications development. Wireless optical communication is a line-of-sight technology which establishes a communication link by transmitting a laser beam through the atmosphere. This technology is employed in many applications operating over a few millimeters up to several hundred kilometers. These applications include, on board inter-chip connection [1], indoor wireless communications [2], terrestrial links [3,4], ground-to-air (unmanned-aerial-vehicle UAV) [5,6], satellite-to-ground [7] and inter-satellite communications links [8–10] for both commercial and military applications [11,12].

A popular commercial application of optical wireless links is free-space optical (FSO) communication in which a point-to-point near ground communication link through the atmosphere is established. Current commercial FSO systems offer data rates in the range of 100 Mega bits/second (Mbps) to 1.5 Giga-bits/second (Gbps) delivering data, voice and video at distances up to 5 kilometers e.g., "SONAbeam™ 1250-M" by fSONA [13] and "TereScope® 5000" by MRV [14]. Experimental measurements show that FSO links can operate at higher rates of order 40 Gbps over distances up to 5 km [15]. Theoretical investigations demonstrated the ability of FSO link to operate at 160 Gbps [16].

This high data rate feature has introduced FSO links as a promising solution for the last-mile problem. Figure 1.1 illustrates a schematic diagram for the last-mile connection between central building and network nodes. This problem arises at the network terminals where it is required to connect buildings, companies, and business offices to the fiber network through a high speed carrier. Connecting the high data rate (Gbps) traffic routed by the fiber network to the end user is still the bottleneck problem where wired or RF connections limit the data rates delivered by the fiber network. The importance to find a solution for this problem lies in the fact that current fiber networks cannot reach all companies and business offices in major cities and it is very expensive to extend this network to all buildings. As an example, only 5% of the major companies in the United States are connected to fiber and 75% are only one mile away from the fiber network [17].

Conventionally, cable modems ($5-15$ Mbps) and digital subscriber line (DSL) (5 Mbps) are deployed to deliver data to the end users. As an alternative solution, radio frequency (RF) communication links can be utilized to increase the rate delivered to the end users. A class of the RF communications is the WiMAX (worldwide interpretability for microwave access) [18] technology. WiMAX utilizes the 2.4 GHz unlicensed frequency band and can theoretically operate at 70 Mbps over a distance of 35 miles [19]. This data rate can be upgraded to 100 Mbps over shorter distances. WiMAX technology is widely utilized for internet access in a point-to-multipoint topology. Although WiMAX provides higher data rates compared to DSL and cable modems, it still does not fulfill the Gbps users requirements.

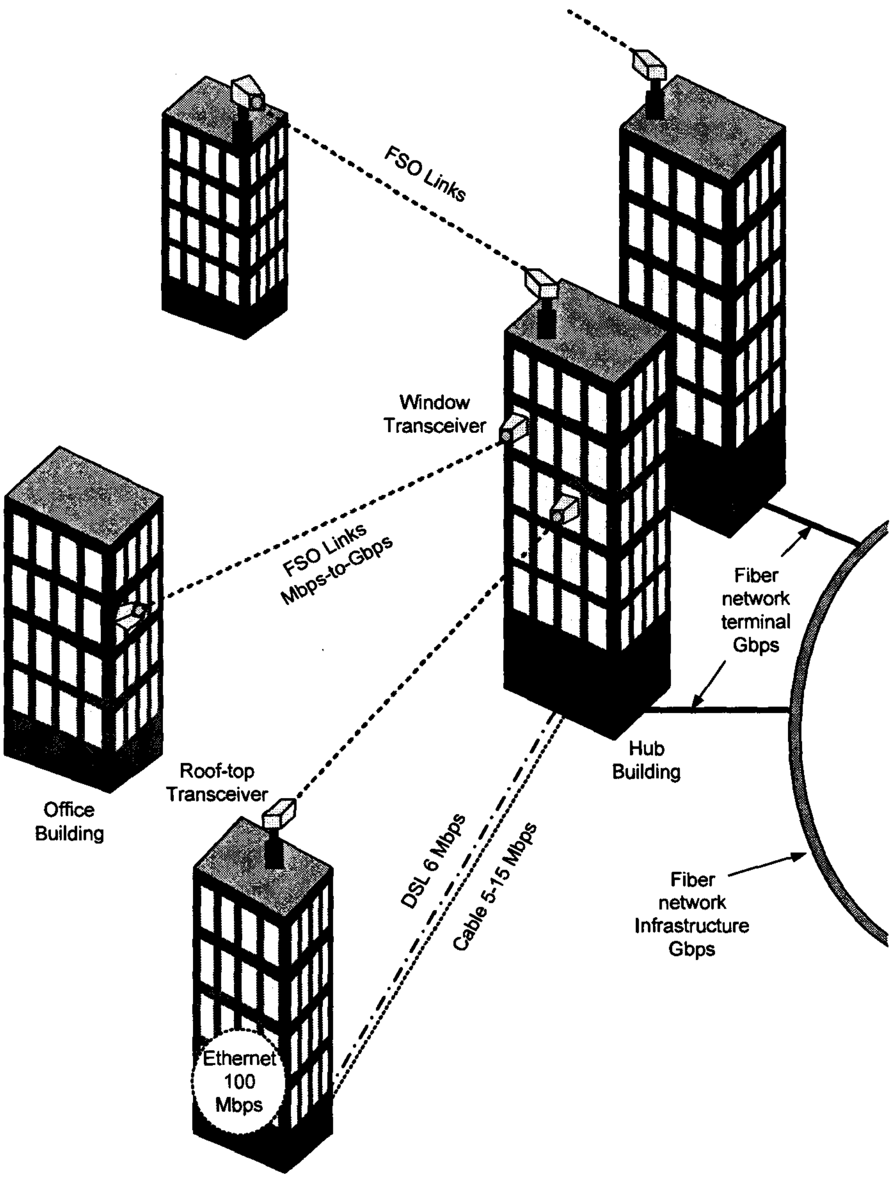

Figure 1.1: Free-space optical (FSO) system topology as a solution for the last-mile connectivity problem.

The latest innovation in RF point-to-point communication is to utilize higher frequency bands in the range 60-86 GHz. Operating at 60 GHz has gained much attention due to the license-free operation allowed by FCC (Federal Communications Commission). In addition, with the large bandwidth allocated by FCC in this band, a 1 Gbps rate can be achieved. Currently, commercial systems like AireBeam™ $60-1250$ by LightPointe™ can operate at 1.25 Gbps over 800 m [20]. Due to the high atmospheric attenuation and the possibility of interference in this license-free band, FCC has approved the 71-76 GHz and 81-86 GHz bands as licensed band for wireless communications [21]. A commercially available product the G1.25-WiFiber®, developed by GigaBeam corporation [22], can operate at 1.25 Gbps over 1 mile. Although these systems are capable of delivering Gbps data rates, the cost and the high attenuation in rain are the main challenges for these systems.

An alternative solution is to utilize a fiber. Although laying a fiber to connect the end user terminals to the fiber network infrastructure is the best solution from rate and reliability perspectives, it is impractical in high density cities. As an example, fiber deployment, including digging and rights-of-way license, in urban areas could cost $\$300,000 - \$700,000$ while a short FSO link of 155 Mbps might cost only $\$15,000 - \$18,000$ [23]. Compared to fiber, FSO links have much lower cost with fiber-like connectivity [15]. They also have the features of ease deployment, rapid setup, digging-free installation, and redeployment flexibility.

Compared to RF communication technologies operating at rates on the order of 10-100 Mbps, FSO links can accommodate much higher data rates, i.e., 40 Gbps [15], with the benefit that no spectrum licensing is required in the infrared band. In addition, an FSO link operating at 155 Mbps costs approximately half the price of RF link at the same rate [24]. Compared to RF communications in the $60-86$ GHz band, FSO links have smaller attenuation in rain. In addition, with the recent advances in FSO communications, a Gigabit wireless link under $10,000 has been introduced by LightPointe™ [25] which is much less expensive than the G1.25-WiFiber® product with average unit price of $44,000. In addition to low cost, FSO links possess the feature of high security communication and immunity to interference due to the narrow beam employed between transceivers [26–28].

FSO links can be utilized for short distance local area networks (LAN) extension, e.g., between company/bank branches [24]. Similar applications include, LAN to LAN building connectivity, intra-campus connections, metro network extension, Gigabit Ethernet access and network backhaul connection [23]. In addition, FSO systems can provide an efficient solution to establish communication links in high density population cities and difficult terrain (crossing highway, airports, etc.) where the insertion of fiber links is too expensive or impractical. Recently, FSO technology has gained growing interest in military applications in US and Europe due to its high security, since it is difficult to intercept the optical signal without corruption. Also it is used for survivability on the battlefield, due to the mobility of FSO links mounted on aircrafts [12]. These advantages introduce FSO communication as a promising candidate for short distance high data rate communication links.

Each high data rate link discussed, i.e., fiber, RF, and FSO, offers a "*zone of advantage*" when compared to the others. Since the advantages of FSO communication links over RF and fiber links are discussed above in detail, it is important to emphasize the limitations and challenges in these links. One of the concerns in FSO link design is the accurate alignment between transmitter and receiver. Another issue is the weather-dependent performance where heavy fog can lead to a link outage. One of the major issues in FSO systems is the limited transmitted power utilized. This limitation arises since eye safety regulations are considered worldwide. Having limited power budget, optimized design is required to achieve the high gains.

One of the main challenges in FSO communication is to combat the fading due to the atmosphere and misalignment to increase the link rate, reliability and distance. As a fundamental step to achieve this, an accurate channel model is required. Another challenge in FSO communications is to find the maximum reliable data rates, i.e., channel capacity, and the corresponding optimum signaling schemes. This point arises since FSO channels are fundamentally different from the well studied RF channels. Thus, algorithms used to implement RF systems may not be suitable for FSO systems. These challenges in FSO system design motivate the need for a comprehensive and novel study for these communication systems.

This thesis considers the analysis and design of FSO systems and develops new results in four major areas: 1) channel modeling, 2) channel capacity and optimal signal design, 3) algorithms to implement this signaling in practice, and 4) performance evaluations to verify the theoretical study.

1.1 Wireless Optical Systems

A wireless optical communication link consists of a transmitter and a receiver as shown in Fig. 1.2. At the transmitter the input data is processed in electrical domain and then converted to optical domain through a laser source. The transmitter is made, in general, of a number of laser sources emitting confined light beam to the receiver. The transmitter is equipped with optics, e.g., telescope, lenses and mirrors, to shape the outgoing beam at transmitter. At the receiver telescope, lenses and mirrors are used to focus the incoming beam on a photodetector which converts the optical power to an output current where the received data are detected.

Laser sources deployed in FSO transmitters typically operate at two popular wavelengths in the nanometer (10^{-9} m) range; 850 nm and 1550 nm [17]. The choice between these two bands depends on many factors, e.g. price, transmitted power and component availability. Due to worldwide eye safety regulation, a maximum optical power density is allowed in each band. Since the 1550 nm band, according to the

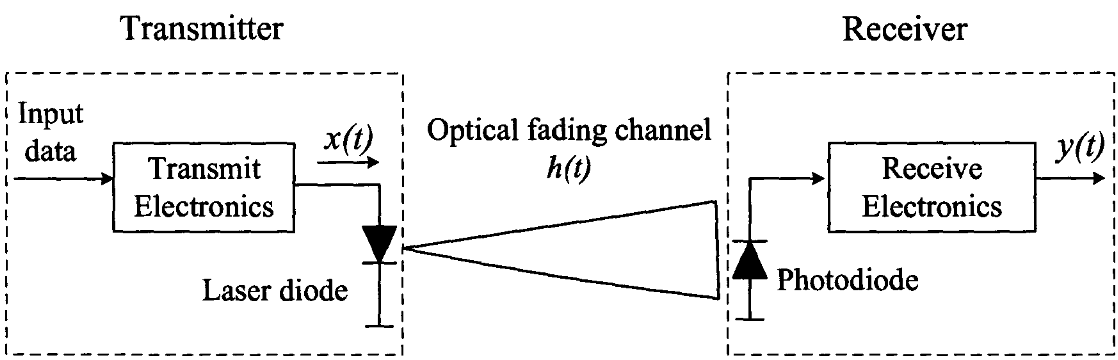

Figure 1.2: Wireless optical channel.

IEC (International Electrotechnical Commission) standards [29], can accommodate higher power, 100 mW/cm^2, compared to the 850 nm band, 1 mW/cm^2, they are widely used in commercial FSO systems operating over long distances [30]. However, the 850 nm band is considered for short distance links due to the availability of inexpensive components. In addition to high price, the lower detector sensitivity at 1550 nm is another drawback, however, the higher allowable optical power in this band can compensate for the low sensitivity problem.

Before light is launched to the atmosphere, it passes through lenses and mirrors which cause optical power loss. A similar process at the receiver occurs as well. These losses are termed transmitter (receiver) optics efficiency η_T (η_R) respectively. The total system optics efficiency is given by $\eta = \eta_T\eta_R$. These losses can be reduced using anti-reflection coatings on both sides.

A block diagram for a wireless optical communication system is shown in Fig. 1.2. The transmitter modulates data onto the instantaneous intensity of optical wave, i.e., *intensity modulation.* The modulation process is performed using a laser diode or a light emitting diode (LED). The collected optical power at the receiver is converted to a current through a photodiode, i.e., *direct detection.* This system is conventionally termed as *intensity modulation direct detection* (IM/DD) FSO system. The output photocurrent signal is proportional to the incident optical power by the scaling factor R_v which represents the detector responsivity. A mathematical model for an FSO communication system that is well justified through measurements is given by [31]

$$y(t) = \eta\ R_v\ h(t)x(t) + n(t). \tag{1.1}$$

where $x(t)$ is the transmitted optical intensity signal, $y(t)$ is the output electrical current, the channel gain $h(t)$ represents the random fluctuations in the propagation medium, η is the optics efficiency and $n(t)$ is the noise. This flat-fading model is justified since the time scale on which $h(t)$ varies is many orders of magnitude slower than $x(t)$. Without loss of generality, the electro-optical conversion ratio of the laser diode is set to unity since it only scales the signal-to-noise ratio.

In FSO systems, the additive noise arises due to high intensity shot noise generated in the photodiode as a result of the signal intensity and the ambient illumination. The statistical model of the noise approaches a Gaussian distribution under the assumption that the received intensity is high [32,33]. Therefore, the noise in FSO systems is conventionally modeled as signal-independent additive white Gaussian noise with variance σ^2 [27].

The channel $h(t)$ is time varying and random due to atmospheric turbulence and time varying misalignment (jitter). These two effects are discussed in detail in Section 2.3 and Section 2.6 respectively. Also in Chapter 2 a new statistical model for the optical channel considering both atmospheric and misalignment fading is developed.

1.2 System Model and Definitions

Consider the mathematical model given in (1.1). One of the most popular and widely used modulation schemes in FSO communications is the M-ary pulse amplitude modulation (M-PAM) where on-off keying (OOK), i.e., $M = 2$, is considered as a special case. The transmitted signal $x(t)$ is represented by the basis function [34],

$$\phi(t) = \begin{cases} \frac{1}{\sqrt{T}} & 0 \leq t \leq T, \\ 0 & \text{otherwise}, \end{cases}$$

as follows,

$$x(t) = \sum_{m=-\infty}^{\infty} \frac{2P}{M-1} \sqrt{T}\, a_m\, \phi(t - kT),$$

where $a_m \in \{0, 1, \ldots, M-1\}$ with equiprobable symbols, P is the average optical power, and T is the symbol duration. At the receiver, the received optical signal is converted to a noisy photocurrent $y(t)$ where the transmitted data is estimated using a matched filter. A matched filter at the receiver with an impulse response $\phi(-t)$ is utilized followed by a sampler that samples the output signal at multiples of the symbol duration T. In this case, timing synchronization is required which becomes a more complicated process at higher data rates. Equivalently, a receiver that integrates and dumps the photocurrent in each symbol period can also be utilized.

A simple discrete representation for the system is given as [31]

$$Y = \eta R_v H X + Z. \tag{1.2}$$

The channel gain H models the random fluctuations of the propagation channel. FSO optical channel is a time-varying flat-fading channel where the fading has a time varying multiplicative effect, i.e., gain, on the transmitted intensity. The time scale at which the gain factor remains approximately constant is denoted as the *coherence time*. Fading channels can be further classified based on the relative scale of the coherence time and the transmitted codeword length. When the coherence time is much smaller than the codeword length so that many fading states occur within the transmission, the channel is termed fast-fading channel. On the other hand, when the coherence time is on the order or greater than the codeword length the channel is termed slow-fading channel [35]. Since typical FSO fading processes coherence time varies approximately in the range $10^{-3} - 10^{-1}$ sec [31], and typical symbol duration T is on the order of 10^{-9} sec, FSO channels are modeled as slow-fading channels. In this case a channel state $H = h$ is chosen from a random ensemble according to the distribution $f_H(h)$ and fixed over many transmitted symbols, i.e., block-fading model. In this case, channel state information at the receiver can be estimated by transmitting a training sequence, i.e., pilot symbols, which, due to the long coherence time, does not severely degrade the link rate [36]. If channel state information is required at the transmitter, it can be sent through a feedback link.

In this model H represents the optical intensity fluctuations which arises due to three factors: path loss, h_ℓ, geometric spread and pointing errors, H_{p}, and atmospheric turbulence, H_{a}, and can be formulated as

$$H = h_\ell \, H_{\mathrm{p}} \, H_{\mathrm{a}}. \tag{1.3}$$

Both H_{a} and H_{p} are random. The attenuation factor h_ℓ is a weather dependent and since the weather changes in minutes to hours it is considered fixed over a long time. These factors are discussed in detail in Sections 2.2, 2.6 and 2.5 respectively.

1.3 Channel Fading and Attenuation

In order to extract the gains offered by FSO links, it is essential to exploit and properly account for the characteristic features of the underlying communication channel. Figure 1.3 presents a schematic diagram showing the main impairments in the FSO channels namely: scattering and absorption, atmospheric turbulence, and misalignment. These impairments attenuate and fade the optical signal at the receiver.

Absorption occurs when a photon of radiation is absorbed by an atmosphere molecule resulting in energy loss and hence reduction in received power. Scattering is the redirection of electromagnetic energy when the radiation interacts with a particle

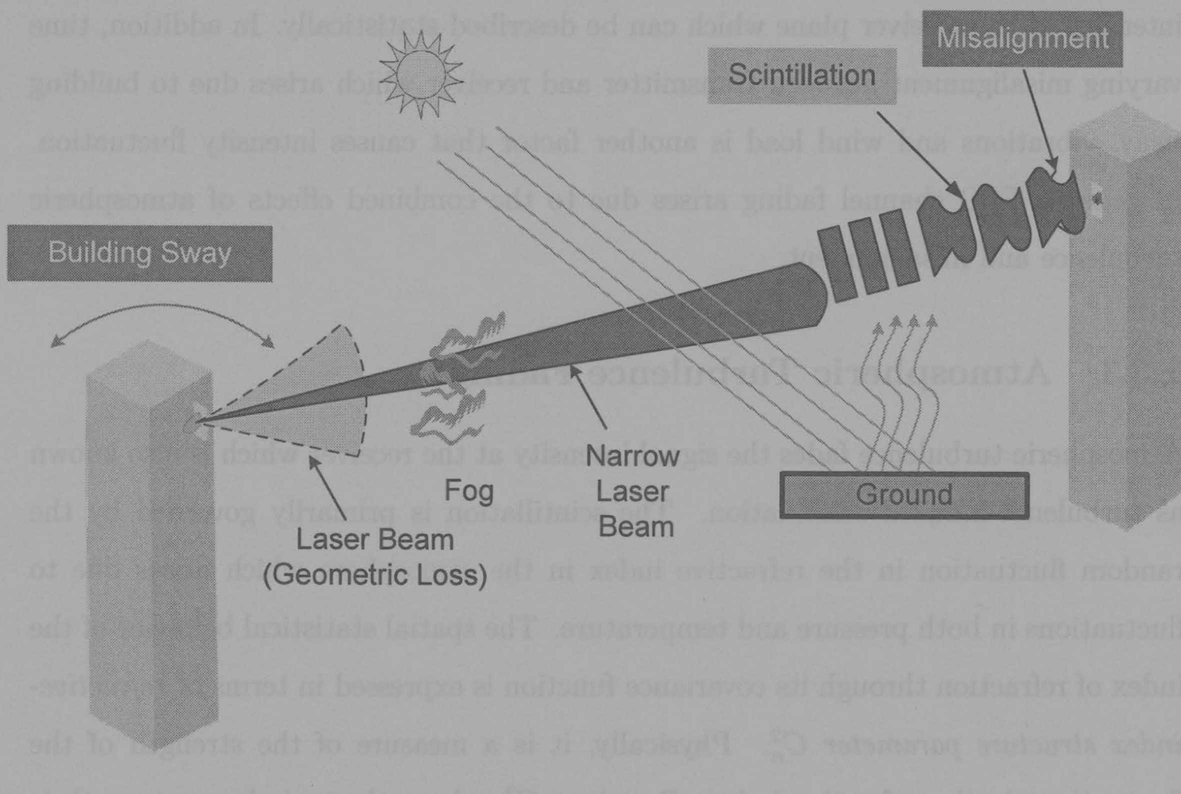

Figure 1.3: FSO channel fading impairments.

in the atmosphere, i.e., the optical wave at this particle location is retransmitted but in a possibly different direction with respect to the line-of-sight axis. [37]. Both absorption and scattering are wavelength dependent and often grouped to define the atmospheric attenuation, h_ℓ, which is discussed in Section 2.5.

However, attenuation is not the only impact caused by atmosphere but also fading which causes intensity fluctuation at the receiver. When the optical wave propagates through the atmosphere it travels via successive air pockets with different temperatures and pressures causing scintillation, i.e., different index of refraction (Section 2.2). Dynamic wind load along with the existence of temperature gradients causes random fluctuations in the atmosphere's refractive index known as *optical turbulence* [28, 37, 38]. This phenomenon results in a random distortion for the optical intensity at the receiver plane which can be described statistically. In addition, time varying misalignment between transmitter and receiver which arises due to building sway, vibrations and wind load is another factor that causes intensity fluctuation. In general, FSO channel fading arises due to the combined effects of atmospheric turbulence and misalignment.

1.3.1 Atmospheric Turbulence Fading

Atmospheric turbulence fades the signal intensity at the receiver which is also known as turbulence-induced scintillation. The scintillation is primarily governed by the random fluctuation in the refractive index in the atmosphere which arises due to fluctuations in both pressure and temperature. The spatial statistical behavior of the index of refraction through its covariance function is expressed in terms of *refractive-index structure parameter* C_n^2. Physically, it is a measure of the strength of the fluctuations in the refractive index. Based on C_n^2 values, the turbulence strength is classified from weak to very strong regimes. The refractive index structure parameter can be computed at a point using the mean-square temperature difference of two fine wire thermometers and the pressure measurements at this point. Furthermore, path average values of C_n^2 can be obtained by optical measurements using scintillometer [39].

Many attempts have been conducted to propose efficient statistical models to describe the intensity fluctuation, h_a, over different fading regimes [3,4,40–45]. However, most of these models were not capable to characterize the fading under all atmospheric turbulence conditions, i.e., some of these models are only suitable to describe the intensity fading under specific turbulence conditions. This fact motivates designers to develop so called "universal" statistical channel models.

In the weak turbulence regime, a log-normal distribution is utilized to describe the channel fading [41]. When the turbulence strength increases to strong turbulence conditions the K-distribution [41] and the log-normally modulated exponential pdf (LNME) [46] are utilized to model the intensity fluctuation. However, they cannot characterize the weak turbulence regime. For the very strong turbulence regime, the negative exponential distribution is utilized [40, 41]. Unlike the previous distributions, the I-K distribution is utilized for both weak and strong turbulence strengths [42, 44]. A recently proposed density function that has a simple closed form is the Gamma-Gamma distribution which describes the intensity fluctuation under different turbulence strengths [47]. This density function has been extensively utilized in the literature to evaluate the FSO system performance since it provides a close agreement with measurement. In this thesis both log-normal and Gamma-Gamma distributions are considered in the analysis. A detailed review for these density functions is given in Section 2.3.

1.3.2 Misalignment Fading (Jitter)

In practical systems, time varying misalignment between a transmitter and a receiver causes pointing errors which limit the performance of FSO links. In inter-satellite communication, this misalignment exists due to relative motions of the end points of the link. For terrestrial links where FSO systems are mounted on high rise buildings to achieve line-of-sight communication, dynamic wind loads, thermal expansion, and internal vibrations cause misalignment. Conventionally, two methods are utilized to mitigate misalignment fading. For expensive systems, a tracking mechanism is employed to precisely align the beam between the transmitter and the receiver through a feedback channel, however, the complexity is high. Another solution is to utilize a wide beam with an increase in the power budget, however, this method is suitable only for low rate short range links.

The impact of misalignment fading (pointing errors/jitter) has been widely investigated for inter-satellite space-based FSO links [9, 10, 48–50] which operate over ranges of many thousands of kilometers. In these links, the assumption of negligible detector aperture size with respect to the beamwidth at the receiver is made due to the large distances. The effect of pointing error and atmospheric turbulence has also been considered in terrestrial links of shorter range. Modeling the combined impact of turbulence and jitter on bit-error rate (BER) has been considered in [51]. Optimizing system performance over transmitter power and beam divergence angle are investigated for terrestrial FSO links [52, 53]. Also statistical models for probability density functions considering atmospheric turbulence and misalignment effects were given in [54]. A similar model is utilized to compute the error probability for target tracking was presented in [55].

In the previous work negligible detector aperture size with respect to the beamwidth (footprint) at the receiver is considered in the analysis. This assumption is valid for inter-satellite communications where the distance is on order of thousands kilometers. However, the situation is different for FSO links operating over shorter ranges, e.g. 1-5 kilometers. As an example, typical optical beam footprint at the receiver for an FSO link operating over 1 km is in the range 1-3 m while the detector aperture radius is approximately 2-10 cm. In fact a statistical model considering the combined effects of atmospheric turbulence and misalignment fading including beamwidth, aperture size and jitter parameter is not available. In this thesis a novel model is developed and discussed in Chapter 2. This model assists in a better understanding and design for FSO systems.

1.4 Channel Capacity

The capacity of a communication channel is the maximum reliable date rate that can be achieved between a transmitter and a receiver. Mathematically, it is the maximum mutual information between channel input and output where the maximization is carried out over all possible input distributions satisfying input signal constraints [56]. Since intensity modulation is considered, a number of signal constraints, different from the RF channels, are applied. These constraints shape the set of permissible input distributions over which the mutual information is maximized. These constraints are discussed in the following section.

1.4.1 Input Signal Constraints

Signaling design for wireless communication is governed by the constraints imposed on the transmitted signals. In wireless optical communication, infrared light with a small wavelength is utilized and hence coherent transmission/detection is difficult. A simple alternative that a majority of wireless optical systems utilize is (IM/DD) system. Due to its simplicity, IM/DD is widely utilized in FSO systems. Signaling design for intensity modulation channels is different from well-known radio-frequency (RF) channels where in the later the mean square of the signal, i.e., electrical power, is constrained. Unlike RF channels, in wireless optical intensity channel the mean of the intensity $x(t)$ is constrained. Physically, due to worldwide eye safety regulations (IEC $60825-1$ [29]), an average optical power (average amplitude) constraint is considered and given by,

$$\lim_{T\to\infty}\frac{1}{T}\int_0^T x(t)dt \le P,$$

where P is the average power limit. Statistically this constraint is expressed as

$$\mathbb{E}\{x(t)\} \le P,$$

where $\mathbb{E}\{\cdot\}$ is the expectation operator. Furthermore, a peak power (peak amplitude) constraint is also applied due to safety and physical source limits and expressed as [29]

$$\forall t, \quad x(t) \le A,$$

where A is the amplitude limit. Finally, since intensity modulation is considered, the transmitted signal must be non-negative, i.e.,

$$\forall t, \quad x(t) \geq 0.$$

Notice that, due to the non-negativity constraint signaling schemes with negative amplitudes such as those developed for RF channel, are not applicable to intensity modulated FSO channels. Thus, wireless optical intensity systems have fundamental differences compared to RF channels and hence signaling schemes designed for RF channels may not be suitable for wireless optical channels. As an example, although a uniform input distribution with two mass points achieves rates close to the channel capacity for Gaussian noise RF channels at low signal-to-noise ratios (SNRs) [57,58], the corresponding rates when this input distribution is employed over optical intensity channels with average optical power constraint are far from the channel capacity at low SNRs [59]. This observation is also true for uniform input distributions with more than two mass points. In order to achieve higher data rate, i.e., minimize the gap to capacity, a proper signaling design is required that accounts for the mentioned constraints explicitly.

As a result, many challenges and open questions regarding signaling design for FSO channels are still under investigation. Currently, well known on-off keying (OOK) and pulse-position modulation (PPM) schemes are widely utilized in commercial systems. Although not necessarily optimum, these schemes are simple and satisfy amplitude constraints.

1.4.2 Channel Capacity: Average Power Constraint

An analytic expression for the capacity of the wireless optical intensity channels under non-negativity and average power constraints is an open problem. However, numerical solutions can provide the asymptotic behavior for the channel capacity. A well known approach to describe the capacity is to develop lower and upper bounds on the channel capacity. The lower bound illustrates the achievable rates, while the difference between the upper and the lower bounds indicates an uncertainty region where it is not known whether the points in this region are achievable or not. The tighter the lower and upper bounds, i.e., the smaller the uncertainty region, the closer the developed rates to the channel capacity.

Recently lower and upper bounds on the channel capacity have been developed in order to characterize the achievable rates. Although more attention has been focused on the lower bound and the corresponding input distribution to realize signaling for these channels, the upper bound provides insights on the tightness of the achieved rates. Since the channel capacity is defined as the maximum mutual information between channel input and output under the input constraints, any input distribution satisfying these constraints results in a lower bound on the channel capacity. Based on this fact, Hranilovic and Kschischang developed a lower bound on the channel capacity considering the continuous exponential distribution [60] since it is the entropy maximizing input distribution. The maxentropic input distribution is considered based on the intuition that the mutual information would be close to the capacity at high SNR. However, the bound is tight only at high SNRs. In an alternative approach, Moser and Lapidoth derived an analytic lower bound using the entropy power inequality (EPI) with exponential input distribution [61, 62]. Although an analytic expression is given, the bound achieves lower rates compared to the maxentropic bound [60], in addition, no input distribution was given to realize these rates.

In order to complete the analysis, an upper bound on the channel capacity is required. An upper bound on the channel capacity can be developed by applying the classical sphere-packing argument presented by Shannon [63]. Sphere packing takes place in signal space in which the non-negativity and average optical power constraints are represented geometrically [64]. These constraints are represented geometrically by a regular n-simplex. You and Kahn applied the sphere-packing concept to derive an upper bound for the optical channel capacity with multiple-subcarrier modulation [65]. Results for Gaussian noise optical intensity channels were presented in [60] where the total volume is outer bounded by a generalized n-simplex. As a result, the derived bound is tight at high signal-to-noise ratio (SNR) and loose at low SNR. A duality-based upper bound for the capacity of optical intensity channels was also presented in [62, 66]. Bounds are derived by converting the mutual information maximization problem over input source distributions to a dual minimax problem.

Combining the bounds discussed above, a significant gap between the lower and the upper bounds, i.e., a large uncertainty region, is noticed. The problem of finding tight bounds and input distributions that achieve the lower bound for optical intensity channels is a challenge and still an open problem.

1.4.3 Channel Capacity: Peak and Average Power Constraints

In this section a more general case is considered where a peak amplitude constraint in addition to the non-negativity and average power constraints is included into the analysis. A capacity lower bound was presented in [61], however, again the bound is not tight and no guidelines were provided on how signaling can be established over the channel. In 1971, the pioneering work of Smith [67] established a new direction toward finding the optimum distribution for channels with bounded-amplitude input signal constraints. Unlike RF Gaussian noise channels with input power constraint where the capacity-achieving input distribution is Gaussian [57], Smith [67] showed that for channels with input power and bounded-input (peak amplitude) constraints the capacity-achieving distribution is discrete with finite number of probability mass points.

Using a similar approach, Shamai [68] showed that a discrete input distribution is a capacity-achieving distribution for Poisson optical channels with bounded-input and power constraints. Later, Shamai and Bar-David [69] obtained the same results for quadrature additive Gaussian channels while Abou-Faycal *et al.* [70] proved these results for Rayleigh fading channels. More attention was directed to these results in the last decades where the discrete input distribution is shown to be a capacity-achieving distribution for many channels [70–73]. Subject to bounded-input and average cost constraints, Chan *et al.* [74] showed that the channel capacity is achievable and derived necessary and sufficient condition for an input distribution to be a capacity-achieving distribution. This procedure was utilized to study signal-dependent optical channels where the capacity-achieving distribution is proven to be discrete with finite number of mass points.

Based on the results obtained by Smith [67] and Chan *et al* [74], the capacity-achieving input distribution for FSO channels under amplitude constraints is discrete. This distribution can be computed numerically by solving a complex non-linear optimization problem. In this problem the mutual information is maximized over the input distribution such that all constraints are met. The mass point amplitudes, locations and number are free parameters in the optimization problem. Efficient numerical optimization techniques can be applied to solve this problem and provide numerical solutions for the input distribution and the channel capacity at different SNRs and peak-to-average power ratios [74]. As can be expected the number of mass points increases with SNR. Although solving this problem at low SNR, i.e., small number of mass point, is simple and fast, at moderate and high SNR when the number of mass points increases the solution becomes complex.

Also upper and lower bounds on the capacity of optical channels were developed in [61, 62]. However, no explicit source distributions were provided that can achieve the lower bound rates, and hence no clear insights for communication system design can be drawn.

As discussed, an analytic expression for a capacity-achieving input distribution for FSO channels is not available. Even simple expressions for input distributions with mutual information that is close to the channel capacity is not presented in the literature. Clearly the need to develop such expressions becomes of major interest since this step will enable designers to approach the promising rates offered by FSO channels.

1.5 Signaling Design and Implementation

One of the most popular modulation schemes utilized in optical communications is pulse amplitude modulation (PAM) schemes. In particular, its binary-level version, on-off keying (OOK) is extensively utilized in optical communications. Also pulse position modulation (PPM) has gained much attention due to its power efficiency. Recently multiple subcarrier modulation techniques have been considered for optical channels [75]. In this technique data are loaded onto different frequency bins. Since this technique does not guarantee non-negative signal amplitudes in the time domain, a DC bias is added such that the transmitted signal satisfies the non-negativity constraint [76, 77]. However, in all previous approaches the analysis is performed using uniform input distributions (signaling). Even for coded modulation where the pairwise error probability is analyzed in [78, 79] equiprobable input bits are assumed. Under different fading statistics the channel capacity is analyzed considering uniform OOK signaling [80]. The bit-error rate for error control coding over FSO links to mitigate the turbulence effect has been studied [81,82] where uniform input distribution was considered.

The previous approaches are in contrast to the capacity results which suggest the use of *non-uniform* input distributions. Although coding for channels with uniform input distribution (equally likely input stream) is simple where binary linear codes can be applied directly, coding for channels with non-uniform input distribution is more complex and different strategies are proposed. Coding for channels with non-uniform input distributions was first presented by Gallager [83]. Gallager used a deterministic mapper at the output of a binary encoder to induce a non-uniform distribution of output symbols, however, decoding algorithm was not given. Later a message-passing algorithm was suggested as a decoding algorithm in [84] to complete Gallager system. In [85] simulation results showed that this method did not generally perform well. Another approach for inducing a non-uniform distribution is presented in [85] where LDPC codes are designed over GF(q) with $q > 2$. Although a substantial performance improvement was reported, the higher complexity in both code design and decoding process limits the use of such techniques. A method to realize a capacity-approaching system with a non-uniform source distribution is to employ multi-level coding (MLC) followed by a deterministic mapper [86–88] where the mapping is not necessarily a one-to-one function.

1.6 Thesis Contributions

This thesis presents novel contributions to FSO channel modeling, capacity, signaling design, and coding algorithms.

A new model for misalignment fading is developed taking into account the beamwidth and the detector aperture radius explicitly. The developed model generalizes the existing fading model where a point receiver is considered as a special case. A statistical channel model for FSO channels combing atmospheric turbulence and misalignment fading is derived and utilized to study FSO systems [89–91]. The model introduces the beamwidth as an additional degree of freedom in system design. Using this feature, a significant performance improvement is achieved using beamwidth optimization compared to a fixed beamwidth in current commercial systems. As an example, in light fog weather condition, beamwidth optimization with uniform OOK signaling achieves 80% gain in rate compared to fixed beamwidth when the link is designed to meet a reliability of 90%.

A tight lower bound on the optical channel capacity under non-negativity and average optical power constraints is derived. An analytic expression for the input distribution that realizes the lower bound is obtained through source entropy maximization. Although not necessarily a capacity-achieving distribution, it provides a tight lower bound on the optical channel capacity over a wide range of signal-to-noise ratios [59, 92]. Compared to previously reported lower bounds [60–62], significant gains in rate are achieved. Furthermore, an analytic upper bound expression is derived using a sphere packing argument. Unlike previous work, the derived upper bound is tighter than the bound in [60] at low signal-to-noise ratio and tighter than [61] at high SNRs. The developed lower and upper bounds asymptotically describe the optical capacity at low and high signal-to-noise ratios [59].

In the general case when non-negativity, average optical power and *peak* optical power constraints are considered, an analytic expression for a discrete non-uniform input distribution is developed. Over a range of SNRs the mutual information using the proposed non-uniform distribution is shown to be significantly close to the channel capacity for different peak-to-average power ratios. In addition, it is much simpler to find the input distribution compared to the capacity-achieving input distribution which requires solving a complex optimization problem. A remarkable gap is noticed compared to uniform distributions [93, 94].

In order to complete the design, an algorithm to realize the non-uniform input distributions proposed for the optical intensity channels is developed. We consider the combination of a multi-level coding (MLC) with a deterministic mapper at the transmitter to induce the proposed non-uniform signaling [88]. Practical low density parity check (LDPC) codes are used for the sub-channels encoders in the MLC structure and the performance of the system is evaluated numerically [95]. Non-uniform distribution with practical finite length LDPC is shown to outperform uniform distribution with capacity-achieving codes.

Finally, with the slow fading nature of FSO channels, the outage capacity for FSO channels is analyzed using the developed statistical channel model. The performance is optimized over both beamwidth and input distribution selection. Significant gain in both rates and reliability is achieved. This analysis provides a formal method to jointly design a code rate, a beamwidth, and signaling scheme for FSO channels.

1.7 Thesis Structure

This thesis focuses on free-space optical intensity channels and develops novel techniques for communication system design.

In Chapter 2, a statistical model for the optical intensity fluctuation at the receiver due to the combined effects of atmospheric turbulence and time varying misalignment (jitter) fading is derived. Beamwidth and detector aperture size are considered explicitly. For atmospheric turbulence, log-normal and Gamma-Gamma density functions are considered in the model. In the case of log-normal distributions, a closed-form expression can be derived for the probability of outage. For Gamma-Gamma density function, numerical integration is utilized. Compared to commercial fixed beamwidth systems, the proposed model allows the designer to optimize system performance over beamwidth based on the channel condition. This model has been utilized by different FSO research groups to study FSO system performance [96–99].

In Chapter 3, upper and lower bounds on the capacity of wireless optical intensity channels under non-negativity and average optical power constraints are derived considering pulse amplitude modulation (PAM). A lower bound is derived based on source entropy maximization for discrete distributions. Utilizing signal space geometry and a sphere packing argument, an upper bound is developed. The tightness of the derived lower and upper bounds at low SNR asymptotically describes the channel capacity in this range. Also the tightness of the lower bound to the channel capacity concludes that non-uniform distributions are essential for FSO communication.

In Chapter 4, the design and analysis of capacity-approaching input signaling under non-negativity, peak amplitude and average optical power constraints is developed. Following the same procedure, a family of input distributions is derived based on source entropy maximization. Again non-uniform distributions have proved their superiority over uniform distributions in FSO channels. For comparison, a capacity-achieving input distribution is presented by numerically solving a complex optimization problem. Comparisons for computational complexity and achievable information rates are presented. It is shown that significant complexity reduction in developing the maxentropic distribution is achieved compared to the capacity-achieving distribution. Furthermore, the achievable rates using non-uniform distributions closely follow the channel capacity over a range of SNRs.

Having determined that non-uniform distribution is capacity-achieving, coding and decoding algorithm to realize this distribution is required. In Chapter 5, Algorithm to realize the proposed non-uniform input distribution is presented. Multi-level coding (MLC) followed by a deterministic mapper at the transmitter with a multi-stage decoding (MSD) at the receiver are utilized. Having N sub-channel encoders in the MLC system, a distribution with mass point probability on the form of $m/2^N$, where m is integer, can be realized. When N increases, more distributions can be realized, however, the encoding/decoding complexity increases as well. In order to balance between these issues, the mass points probabilities developed previously are quantized to form a modified input distribution. The performance of the modified distribution is compared to the channel capacity at different SNRs. In addition to the substantial reduction in system complexity, the resulting mutual information is very close to the channel capacity. Having theoretically verified its potential, numerical performance evaluation for the modified distribution using finite length low density parity check (LDPC) codes is presented. It is shown that the non-uniform distribution with finite length LDPC outperforms uniform distribution with capacity-achieving codes.

In Chapter 6, the outage capacity of slow-fading FSO channels under atmospheric turbulence and misalignment fading is analyzed. The outage capacity is optimized over the selection of beamwidth and input distribution. It is shown that more than double the rate can be achieved compared to uniform distributions at a given reliability. In addition, in the case when a communication link is in outage when uniform distribution is utilized, a reliable communication can be established using the developed non-uniform distributions.

Finally. Chapter 7 presents concluding remarks and future directions.

Chapter 2

Statistical Channel Model: Atmosphere and Misalignment

Optical signal propagation through the atmosphere is affected by atmospheric turbulence (scintillation) and misalignment errors which fade the signal at the receiver and deteriorate the link performance. In order to achieve reliable communication over FSO channels, an accurate model for the underlying communication channel is essential as a fundamental step for optimum system design. Seen as a random effect, atmospheric turbulence and misalignment fading can be described by a statistical model. Although atmospheric turbulence statistics have been well modeled, a general model that takes into account the effect of misalignment is not available. Models considering the case of a point receiver have been developed. However, the model does not reflect the real behavior of the FSO channels since aperture size is not considered. In this chapter, a statistical model for the optical intensity fluctuation at the receiver due to the combined effects of atmospheric turbulence and misalignment (jitter) is derived. Unlike earlier work, the developed model considers the effect of beamwidth, detector size and jitter variance explicitly.

2.1 Gaussian-Beam Wave

Wave propagation analysis is conventionally classified into three major categories: plane wave, spherical wave, and Gaussian-beam wave. Since FSO systems operate over distances on the order of hundred meters to few kilometers, it is convenient to consider a Gaussian-beam wave model to study the optical wave propagation in these systems. Consider a Gaussian-beam wave emitting from an aperture in the plane $z = 0$ where the amplitude distribution in this plane is Gaussian. The beam is defined through two parameters, an effective beam radius w_o (meter) representing the beamwidth when the amplitude falls to $1/e$ of its peak, and a phase front radius of curvature F_0 (meter). The wave field $U_0(r, z)$ at $z = 0$ is given by [37, p.88],

$$U_0(r,0) = u_0 \exp\left(-\frac{r^2}{w_o^2} - \frac{ikr^2}{2F_o}\right) = u_0 \exp\left(-\frac{1}{2}\alpha_o k r^2\right),$$

where u_0 is the field amplitude, $r = \sqrt{x^2+y^2}$ is the radial distance from the beam centre in the plane, $k = 2\pi/\lambda$ is the optical wave number, λ is the wavelength, $i = \sqrt{-1}$ and

$$\alpha_o = \frac{2}{kw_o^2} + i\frac{1}{F_o}.$$

Based on the value of F_o, the Gaussian beam is classified to convergent, collimated or divergent beam as shown in Fig. 2.6. The wave field at a point $\boldsymbol{R} = (x, y, z)$, for a free-space medium with fixed refractive index $n = 1$, is obtained by solving the wave equation

$$\nabla^2 \boldsymbol{E} + k^2 \boldsymbol{E} = \boldsymbol{0}$$

where $\boldsymbol{E}$ is the field of the electromagnetic wave and $\nabla^2 = \partial^2/\partial x^2 + \partial^2/\partial y^2 + \partial^2/\partial z^2$ is the Laplacian operator. The above equation can be decomposed into three scalar equations representing the components of $\boldsymbol{E}$. Let U denotes one of the scalar components of $\boldsymbol{E}$ then,

$$\nabla^2 U + k^2 U = 0$$

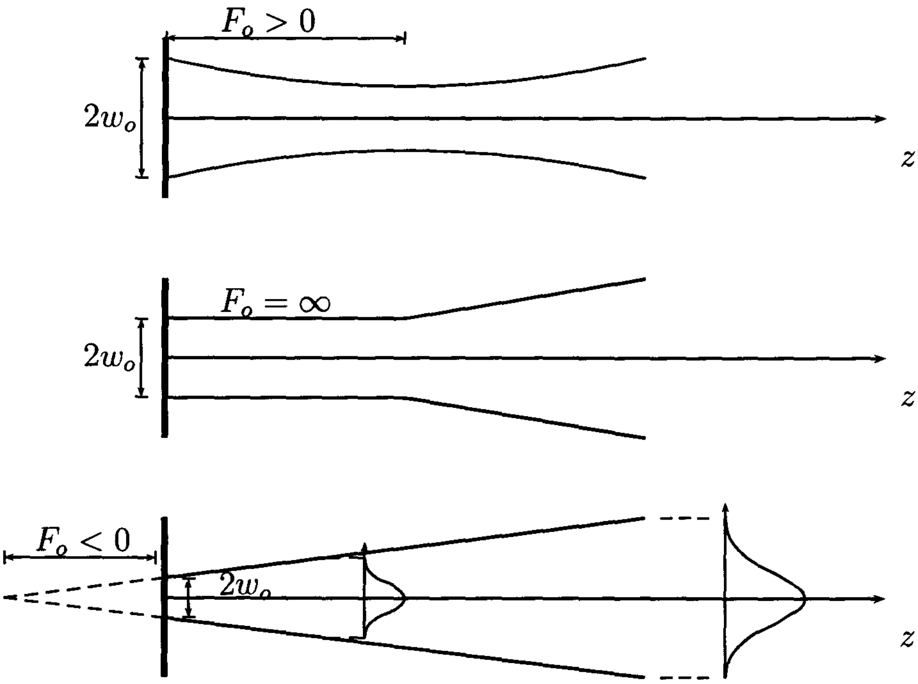

Figure 2.1: Gaussian-beam wave with effective beam radius w_o at the transmitter aperture ($z = 0$) and different radius of curvature, (a) convergent beam ($F_o > 0$), (b) collimated beam ($F_o = \infty$), and (c) divergent beam ($F_o < 0$).

Solving the wave equation, the wave field at a point $\boldsymbol{R}$ is given by [37, p.91]

$$U_0(r,z) = \frac{1}{p(z)} \exp\left(ikz - \frac{k\alpha_o}{2p(z)} r^2\right)$$

where

$$p(z) = 1 + i\alpha_o z = \underbrace{1 - \frac{z}{F_o}}_{\Theta_o} + i \underbrace{\frac{2z}{kw_o^2}}_{\Lambda_o}.$$

hence the Gaussian beam propagation can be described by the parameters

$$\Theta_o = 1 - \frac{z}{F_o}, \quad \text{and} \quad \Lambda_o = \frac{2z}{kw_o^2}$$

The *irradiance* or *intensity* of the optical wave is defined as the square magnitude of the field $U_0(r,z)$ in watt per meter square units and is given as,

$$I(r,z) = |U_0(r,z)|^2. \qquad [\mathrm{W/m^2}]$$

When the refractive index is a function of the location, i.e., $n(\boldsymbol{R})$, the field $U_0(r,z)$ is no longer valid. In this case a general expression for the field denoted $U(r,z)$ is developed in terms of $U_0(r,z)$. In the following section the development is outlined.

2.2 Atmosphere and Irradiance Fluctuations

The local temperature of the atmosphere is dynamically changing resulting in temporal and spatial temperature gradients. In the presence of dynamic wind, this temperature gradient causes a randomly varying spatial distribution for the refractive index. Optical wave propagation near the earth surface travels through this random medium resulting in random fluctuation in the received optical wave. This phenomenon is known as *optical turbulence.* Historically, Kolmogorov presented the classical theory of turbulence. Based on this theory, the turbulent air is represented by a set of eddies of scale size ranging from large scale size L_o (*outer scale*) to small scale size l_o (*inner* *scale*). These parameters can be estimated from channel measurements [100, 101]. A simple illustrative diagram for the atmosphere and the effect of random turbulence cells is shown in Fig. 2.2.

Electromagnetic wave propagation in a random medium is governed by a stochastic wave equation given by ,

$$\nabla^2 \boldsymbol{E} + k^2 n^2(\boldsymbol{R})\boldsymbol{E} = \mathbf{0}$$

where $n(\boldsymbol{R})$ is the refractive index. The wave equation can be further simplified in terms of the field components U as follows,

$$\nabla^2 U + k^2 n^2(\boldsymbol{R}) U = 0 \tag{2.1}$$

The refractive index fluctuation due to wind speed and temperature gradient can be expressed as,

$$n(\boldsymbol{R}) = 1 + n_1(\boldsymbol{R}),$$

where $n_1(\boldsymbol{R})$ is the random deviation with mean $\langle n_1(\boldsymbol{R})\rangle = 0$ and covariance function,

$$B_n(\boldsymbol{R}_1, \boldsymbol{R}_2) = \langle n_1(\boldsymbol{R}_1) n_1(\boldsymbol{R}_2)\rangle,$$

and $\langle\cdot\rangle$ denotes the ensemble mean. For statistically homogeneous and isotropic medium, the covariance function is a function of $R = |\boldsymbol{R}_2 - \boldsymbol{R}_1|$ as

$$B_n(\boldsymbol{R}_1, \boldsymbol{R}_2) = B_n(R),$$

and exhibits the asymptotic behavior,

$$2\Big(B_n(0) - B_n(R)\Big) = \begin{cases} C_n^2 l_o^{-4/3} R^2, & 0 \le R \le l_o; \\ C_n^2 R^{2/3}, & l_o \le R \le L_o. \end{cases}$$

where C_n^2 is the refractive-index structure parameter ($\mathrm{m}^{-2/3}$). Physically, C_n^2 is a measure of the fluctuations in the refractive index. It can be computed at a point

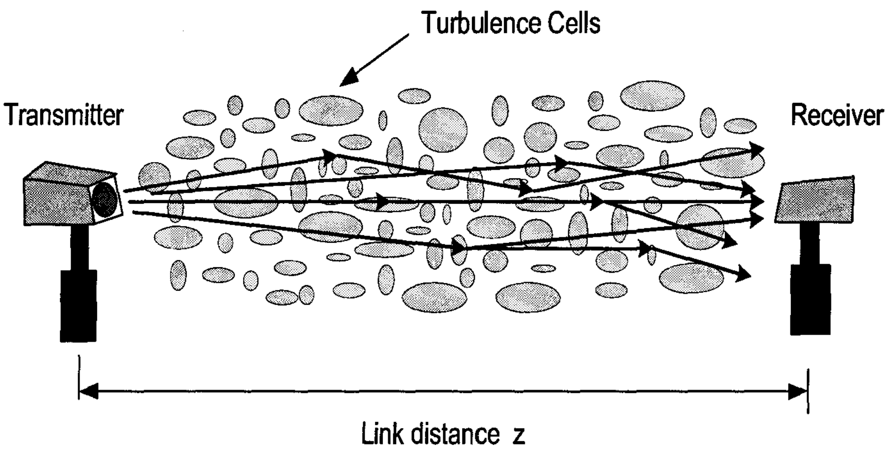

Figure 2.2: Optical wave propagation through turbulence cells.

using the mean-square temperature difference of two fine wire thermometers and the pressure measurements at this point.

When an optical wave propagates through the atmosphere both its amplitude and phase are distorted and experience random fluctuations. Several approaches are proposed to solve the stochastic wave equation relying on different assumptions and approximations [37, p. 137]. These approximations are considered in order to simplify the analysis and develop statistical quantities that describe the optical wave propagation. Theories utilized to solve the wave equation are classified into either weak or strong fluctuation theories. The Rytov variance given by,

$$\sigma_{\mathrm{R}}^2 = 1.23\, C_n^2\, k^{7/6}\, z^{11/6},$$

where z is the propagation distance, is conventionally used to distinguish between weak and strong irradiance fluctuations [28, 31]. Physically, Rytov variance represents the irradiance fluctuations for an unbounded plane wave [37]. Three cases are considered, weak turbulence ($\sigma_{\mathrm{R}}^2 \ll 1$), moderate turbulence ($\sigma_{\mathrm{R}}^2 \backsim 1$), and strong turbulence ($\sigma_{\mathrm{R}}^2 > 1$).

An important parameter associated with the optical wave propagation is the *correlation width*, ρ_c. Correlation width is defined as the width of the irradiance covariance function at $1/e^2$ of its peak value. Note that ρ_c depends on both the weather and the link distance. A receiver aperture size smaller than the correlation width acts like a point receiver while aperture size larger than ρ_c can average the irradiance fluctuations, i.e., scintillation. This effect is known as *aperture averaging* effect.

An important measure that describes the irradiance fluctuation is the *scintillation index* defined as,

$$\sigma_I^2 = \frac{\langle I^2 \rangle}{\langle I \rangle^2} - 1.$$

In wireless optical communications the system performance is measured via different quantities, e.g., bit error rate, link reliability, etc. These measures are computed using the probability density function (pdf) of the irradiance. In the following section a detailed discussion is given for modeling the density function of irradiance under weak and strong turbulence conditions.

2.3 Irradiance Statistical Models Overview

Atmospheric turbulence causes fluctuations in the received optical intensity due to variations in the refractive index along the propagation path [28, 37, 38]. Many statistical models have been proposed to describe the optical intensity fluctuations [40–47, 102–105]. A basic guideline to choose a good model among this family is the capability of the model to validate the practical measurements. Since the model is weather dependent, it is important that the model parameters can be obtained directly from channel measurements. Mathematically, a simple analytic expression is of major importance to simplify system analysis. In addition, a universal model able to characterize different turbulence strengths is one of the main concerns.

In the weak turbulence regime, a log-normal distribution is conventionally utilized to describe the channel fading [41]. In addition to its simple and tractable mathematical form, the distribution is characterized by one parameter that can be obtained directly from channel measurement. Also it closely validates the practical measurements [45,47]. When the turbulence strength increases it is noticed that the log-normal distribution under estimates the behavior of the distribution tail compared to the measured data [41,43,104]. Since the system performance, e.g. probability of error, is evaluated based on the tails, then log-normal distribution is no longer suitable for strong turbulence regimes.

Under strong turbulence conditions the K-distribution [41] and the log-normally modulated exponential pdf (LNME) [46] are utilized to model the intensity fluctuation. However, they can not characterize the weak turbulence regime. An extension for the K-distribution is the I-K distribution that can characterize the intensity fluctuations for both weak and strong turbulence strengths [42,44]. Although the Beckmann pdf gives good agreement with measurement for weak and strong regimes, it is expressed in an integral form and it is not clear how to deduce its parameters from atmospheric measurements. When the turbulence strength increases and approaches the very strong turbulence regime, the negative exponential distribution is utilized to characterize the intensity fluctuations [41].

In a recent approach, a Gamma-Gamma distribution has been proposed. It has the advantage of describing the turbulence strength from weak to very strong turbulence regimes. The Gamma-Gamma density function provides close agreement with the measurements under different turbulence strengths [47]. In addition, the parameters involved in the distribution can be measured directly from the channel. In this work both the log-normal and the Gamma-Gamma density functions are considered in the analysis. The log-normal is considered since a closed-form expression for error probability can be derived.

2.3.1 Log-normal density function

As discussed in Section 2.2, several approaches are proposed to solve the stochastic wave equation relying on different assumptions and approximations [37]. The wave equation is analyzed through perturbation theories one of which is the Rytov approximation. The Rytov approximation is utilized to analyze the optical wave propagation in weak irradiance fluctuations regime where the field is expressed as a multiplication of perturbation terms. In this method the wave field $U(r,z)$ is expressed in terms of unperturbed field $U_0(r,z)$ through the form [37, p. 143],

$$U(r,z) = U_0(r,z)e^{\psi(r,z)}$$

where $\psi(r,z) = \psi_1(r,z) + \psi_2(r,z) + \ldots$ is a complex phase perturbation with ψ_1 and ψ_2 representing first- and second-order perturbations respectively. In order to simplify the analysis, the first-order perturbation is considered where the perturbation is expressed as $\psi_1(r,z) = \chi(r,z) + i\vartheta(r,z)$ where $\chi(0,z)$ denotes the *log amplitude* which is assumed to have a Gaussian distribution and $\vartheta(r,z)$ is the log phase. The irradiance of the optical wave is given by

$$I_{\mathrm{a}}(0,z) = |U_0(0,z)|^2 e^{\psi_1(0,z)+\psi_1^*(0,z)} = |U_0(0,z)|^2 e^{2\chi(0,z)}$$

For simplicity, let I_{a} denote the irradiance at the beam center, i.e., $r = 0$ and at distance z. The above expression is conventionally written as,

$$I_{\mathrm{a}} = |U_0|^2 e^{2\chi}$$

From the above relation, since the logarithm of the irradiance has a Gaussian (Normal) distribution, then I_a has a log-normal distribution. Let h_{a} denote the normalized channel gain given as,

$$h_{\mathrm{a}} = I_{\mathrm{a}}/\langle I_{\mathrm{a}}\rangle.$$

Then h_a has a normalized log-normal distribution, i.e., $\langle h_a \rangle = 1$, given by,

$$f_{h_a}(h_a) = \frac{1}{2h_a\sqrt{2\pi\sigma_\chi^2}} \exp\left(-\frac{(\ln h_a + 2\sigma_\chi^2)^2}{8\sigma_\chi^2}\right). \tag{2.2}$$

where the log-amplitude of the optical intensity has a Gaussian pdf with variance σ_χ^2 given by [28],

$$\sigma_\chi^2 = 0.30545\, k^{7/6}\, C_n^2\, z^{11/6} \approx \frac{\sigma_R^2}{4}.$$

The scintillation index is given by,

$$\sigma_{I_a}^2 = \frac{\langle I_a^2 \rangle}{\langle I_a \rangle^2} - 1 = \frac{\langle h_a^2 \rangle}{\langle h_a \rangle^2} - 1.$$

The scintillation index for the log-normal distribution is given by,

$$\sigma_{I_a}^2 = \exp\left(4\sigma_\chi^2\right) - 1 \tag{2.3}$$

Although the log-normal distribution can efficiently describe the intensity fluctuations and validate the measurements [28,31,41] in very weak turbulence regime ($\sigma_R^2 \leq 0.3$), the distribution cannot characterize strong turbulence [41,43] where the simulated data does not match the practical measurements.

2.3.2 Gamma-Gamma density function

A recent approach to describe the irradiance fluctuation is to utilize the extended Rytov approximation method. The perturbation is assumed to be a multiplication of small scale and large scale fluctuation as [37, p. 325],

$$U(r,z) = U_0(r,z) \exp\left(\psi_L(r,z)\right) \exp\left(\psi_S(r,z)\right),$$

where ψ_L and ψ_S are statistically independent phase perturbations. The irradiance, I_a at $r = 0$ is modeled as $I_a = \Upsilon_L \Upsilon_S$, where Υ_L and Υ_S are the large and small scale irradiance fluctuation. The probability density functions for Υ_L and Υ_S are chosen as a Gamma density function [37, Sec 9.10]. The Gamma density function was chosen based on the observation that it gives an excellent approximation for many propagation problem involving intensity [37].

Based on this model the channel gain, $h_a = I_a / \langle I_a \rangle$, has a probability density function that is conventionally termed Gamma-Gamma density function as denoted by Andrews *et al* [37]. The Gamma-Gamma density function is given by [40, 41].

$$f_{h_a}(h_a) = \frac{2(\alpha\beta)^{(\alpha+\beta)/2}}{\Gamma(\alpha)\Gamma(\beta)}(h_a)^{\frac{(\alpha+\beta)}{2}-1} K_{\alpha-\beta}(2\sqrt{\alpha\beta h_a}), \tag{2.4}$$

where $K_{\alpha-\beta}(.)$ is the modified Bessel function of the second kind, $1/\alpha$ and $1/\beta$ are the variances of the large and small scale fluctuations [41] given by

$$\begin{aligned} \alpha &= \frac{1}{\sigma^2_{\Upsilon_L}} = \frac{1}{\exp(\sigma^2_{\ln \Upsilon_L}) - 1} \\ \beta &= \frac{1}{\sigma^2_{\Upsilon_S}} = \frac{1}{\exp(\sigma^2_{\ln \Upsilon_S}) - 1} \end{aligned} \tag{2.5}$$

Expression for α and β for plane, spherical and Gaussian-beam wave are given explicitly in [37]. In all cases α and β are expressed in terms of Rytov variance, i.e., C_n^2, which can be measured directly from the atmosphere. Expressions for α and β considering Gaussian-beam wave propagation are given explicitly in Section 2.4.

It has been shown that the Gamma-Gamma pdf provides close agreement with measurements under a variety of turbulence conditions, i.e., weak to strong turbulence regimes [40, 41]. As a result, the Gamma-Gamma density function will be utilized to analyze the FSO system performance. However, for the very weak turbulence regime the log-normal density function will be utilized since simple closed form expression for the performance measures can be developed. In the following section a brief description for the Gaussian-beam propagation model and parameters are given.

2.4 Gaussian-Beam Wave Parameters

Consider a Gaussian beam propagating in free space with a transmitter aperture located at plane $z = 0$. When the receiving aperture is smaller than the irradiance correlation width the receiver behaves as a point receiver. However, for larger aperture size, the receiver will average out the fluctuations of the received signal over aperture area hence decreasing scintillation [47, 102, 103]. Let

$$\Theta_1 = \frac{\Theta_o}{\Theta_o^2 + \Lambda_o^2}, \quad \text{and} \quad \Lambda_1 = \frac{\Lambda_o}{\Theta_o^2 + \Lambda_o^2}.$$

Taking into account the aperture average effects at the receiver and the limiting case where $l_o = 0$ and $L_o = \infty$, the large and small scale variances are given as [37, p. 420],

$$\sigma^2_{\ln\Upsilon L}(D_G) = \frac{0.49\left(\frac{\Omega_G-\Lambda_1}{\Omega_G-\Lambda_1}\right)^2\sigma_B^2}{(1+T+0.56(1+\Theta_1)\sigma_B^{12/5})^{7/6}}, \tag{2.6}$$

$$\sigma^2_{\ln\Upsilon S}(D_G) = \frac{(0.51\sigma_B^2)/(1+0.69\sigma_B^{12/5})^{5/6}}{1+(1.2(\sigma_R/\sigma_B)^{12/5}+0.83\sigma_R^{12/5})/(\Omega_G+\Lambda)}, \tag{2.7}$$

where $\Omega_G = \frac{16z}{kD_G^2}$, D_G is the receiver diameter, and

$$T = \frac{0.4(2-\bar{\Theta}_1)(\sigma_B/\sigma_R)^{12/7}}{(\Omega_G+\Lambda_1)\left(\frac{1}{30}\right)(10-15\bar{\Theta}_1+6\bar{\Theta}_1^2)^{6/7}}.$$

The parameter σ_B^2 is given by,

$$\sigma_B^2 \cong 3.86\sigma_R^2\left[(0.4(1+2\Theta_1)^2+4\Lambda_1^2)^{5/12}\times\cos\left(\frac{5}{6}\tan^{-1}\left(\frac{1+2\Theta_1}{2\Lambda_1}\right)\right)-\frac{11}{16}\Lambda_1^{5/6}\right].$$

The scintillation index is given by

$$\sigma^2_{I_a}(D_G) = \exp\left(\sigma^2_{\ln\Upsilon L}(D_G)+\sigma^2_{\ln\Upsilon S}(D_G)\right)-1. \tag{2.8}$$

When a point receiver is considered, the same expressions are utilized with the limiting behavior that $D_G \to 0$. When practical values for $l_o > 0$ and $L_o < \infty$ are considered, equation (2.8) under estimates the scintillation index at large Rytov variance [37].

2.4.1 Gaussian Beam Off-axis Statistics

Note that the scintillation index expression is derived based on perfect alignment between transmitter and receiver. In Section 2.6 time varying misalignment will be considered in the analysis to develop a general statistical model for the irradiance fluctuations. Therefore, it is important to introduce the behavior of the scintillation index *at a point* in the transverse plane as a function of radial distance r from the beam centre which is given by [37, p.353]

$$\sigma_{I_a}^2(r,z) = \left[\exp\left(\sigma_{\ln\Upsilon_L}^2(0) + \sigma_{\ln\Upsilon_S}^2(0)\right) - 1\right] + 4.42\sigma_R^2\Lambda_e^{5/6}\left(\frac{r^2}{w_z}\right) \tag{2.9}$$

where $\Lambda_e = 2z/kw_z^2$ is the effective Gaussian beam wave parameter considering the atmospheric effect. The Gaussian beam waist w_z at the receiver given by [37, p. 238 Eq. 45],

$$w_z \approxeq w_o\sqrt{\Theta_o^2 + \Lambda_o^2}\sqrt{1 + 1.63\sigma_R^{12/5}\Lambda_1},$$

where this relation can be utilized for all atmospheric turbulence conditions [37, Ch. 7, Eq. 45]. More attention should be considered when the time varying misalignment is taken into account since for a given beam deviation the scintillation index at the receiver changes. However, for a divergent beam the variations in the scintillation index with r is small. In Fig. 2.3 the relative deviation $\Delta\sigma_{I_a}^2(r,z)$ in the scintillation index defined as

$$\Delta\sigma_{I_a}^2(r,z) = \frac{\sigma_{I_a}^2(r,z) - \sigma_{I_a}^2(0,z)}{\sigma_{I_a}^2(0,z)} \times 100 \quad [\%] \tag{2.10}$$

is plotted versus the radial distance r from the beam centre for different values of C_n^2 varying from 5×10^{-14} to 50×10^{-14} with $z = 1000$ m, $\lambda = 1550$ nm, $w_o = 4$ cm and $F_0 = -20$ m which are typical values for a Gaussian beam propagation in free space. In this example the beam waist at the receiver is $w_z \approx 2$ m, i.e., a divergence angle of 2 mrad at the transmitter. Assume that the maximum misalignment angle is 0.5 mrad, i.e., approximately $r = 50$ cm deviation at the receiver then the maximum

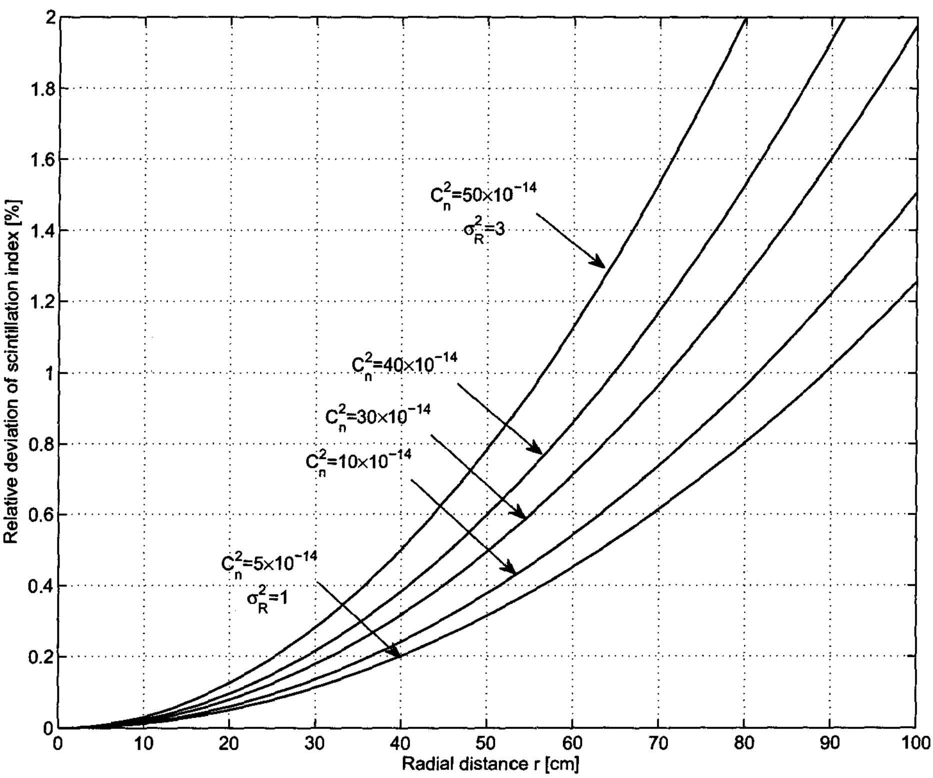

Figure 2.3: Relative deviation of scintillation index versus displacement from the beam centre for different turbulence strengths over a propagation distance $z = 1000$ m.

relative deviation in the scintillation index is 0.8% as shown from Fig. 2.3. That is, the scintillation index can be considered fixed at the receiver and equal to its value at the beam centre. In the following analysis this assumption is considered as a key element through the derivations.

2.5 Atmospheric Attenuation

Optical power attenuation while the wave propagates through the atmosphere is caused due to two phenomena: absorption and scattering. Absorption is the event when the electromagnetic energy is absorbed by atmosphere particles resulting in power attenuation. Scattering is the redirection of electromagnetic energy when the radiation interacts with a particle in the atmosphere, i.e., the optical wave at this particle location is retransmitted but into different direction with respect to the line of sight axis. [37]. Absorption and scattering are weather and wavelength dependent. Since the time scale at which the weather condition changes (minutes to hours) is much larger than the time scale for the fading process i.e., coherence time $T_c \backsim 10$ msec, then h_ℓ is considered fixed over many fading states. The atmospheric attenuation is well studied and rigorous mathematical models are used to describe its behavior.

The attenuation of laser power through atmosphere is described by the exponential Beers-Lambert Law as [17],

$$h_\ell(z) = \frac{P(z)}{P(0)} = \exp(-\nu\ z)$$

where $h_\ell(z)$ is the loss over a propagation path of length z, $P(z)$ is the laser power at distance z and ν is the attenuation coefficient [4]. The attenuation factor h_ℓ is considered a fixed scaling factor during multiple fading states. It depends on the size and distribution of the atmosphere particles and the wavelength utilized. It

Table 2.1: Atmospheric attenuation for different weather conditions

Weather condition	visibility [km]	Attenuation [dB/km]
Clear	23	0.2
	10	0.4
Haze	4	2
	2	4
	1	9
Fog	0.5	21
	0.2	60
	0.05	272

can be expressed in terms of the visibility, which can be measured directly from the atmosphere [3, 17]. Many empirical formulas are given in the literature for the attenuation coefficient based on measurements. However, a simple and well verified formula is given by [17],

$$\nu = \frac{3.91}{V}\left(\frac{\lambda}{550\times 10^{-9}}\right)^{-q},$$

where V is the visibility in kilometer, λ is the wavelength, and q is the size distribution of the particles related to the visibility by,

$$q = \begin{cases} 1.6 & V > 50 \text{ km}, \\ 1.3 & 6 \text{ km} < V < 50 \text{ km}, \\ 0.585\ V^{1/3} & V < 6 \text{ km}. \end{cases}$$

Table 2.1 illustrates how the attenuation in dB/km varies for different weather conditions with different visibilities. Notice that, the clear weather condition has the lowest attenuation value. The main challenge in FSO communication is how to combat the fog weather condition since, as can be seen from Table 2.1, it has the highest attenuation. This high attenuation channel limits the FSO link to few meters and leads to link outage for longer distance links. However, the irradiance fluctuation, due to atmospheric turbulence, is higher in clear weather compared to fog. In summary, there is a strong inverse correlation between the turbulence strength and attenuation. For example, strong turbulence is highly unlikely to occur during a fog event [106].

2.6 Misalignment Fading

In line-of-sight FSO communication links, pointing accuracy is an important issue in determining link performance and reliability. However, wind loads and thermal expansions result in random building sways which in turn cause pointing errors and signal fading at the receiver [51]. As discussed in Section 1.3.2, a negligible detector aperture size with respect to the beamwidth (footprint) at the receiver is considered in literature. Unlike previous work, in this section a new statistical model for pointing error loss due to misalignment is developed. The model considers detector aperture size, beamwidth, and jitter variance explicitly.

Consider a spatial Gaussian beam profile where the normalized spatial distribution of the transmitted intensity at distance z from the transmitter is given by [107],

$$I_{beam}(\boldsymbol{r}, z) = \frac{2}{\pi w_z^2} \exp\left(-\frac{2\|\boldsymbol{r}\|^2}{w_z^2}\right), \tag{2.11}$$

where $\boldsymbol{r}$ is the radial vector from the beam center. The attenuation due to geometric spread with pointing error $\boldsymbol{d}$ is expressed as,

$$h_{\mathrm{p}}(\boldsymbol{d}, z) = \int_{\mathcal{A}} I_{beam}(\boldsymbol{r} - \boldsymbol{d}; z)\, d\boldsymbol{r},$$

where $h_{\mathrm{p}}(\cdot)$ represents the fraction of the power collected by the detector and $\mathcal{A}$ is the area of a detector with aperture radius a. The detector and the beam footprint in the transverse plane are shown in Fig. 2.4.

Due to the symmetry of the beam shape and the detector area, the resultant $h_{\mathrm{p}}(\boldsymbol{d}, z)$ depends only on the radial distance $d = \|\boldsymbol{d}\|$. Therefore, without loss of

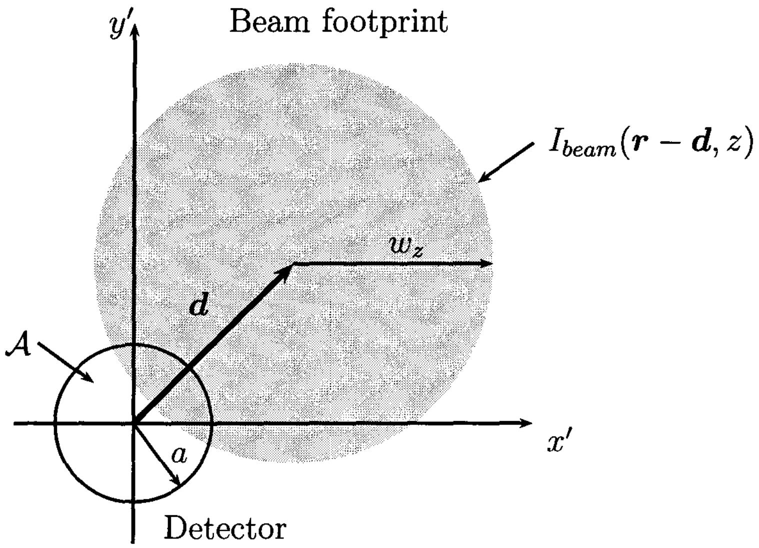

Figure 2.4: Detector and beam footprint with misalignment at the detector plane.

generality, we can assume that the radial distance is located along the x'-axis. The fraction of the collected power at a receiver of radius a in the transverse plane of the incident wave can be expressed as,

$$h_{\mathrm{p}}(d, z) = \int_{-a}^{a} \int_{-\zeta}^{\zeta} \frac{2}{\pi w_z^2} \exp\left(-2\frac{(x'-d)^2 + y'^2}{w_z^2}\right) dy'dx', \tag{2.12}$$

where $\zeta = \sqrt{a^2 - x'^2}$. As shown in Appendix A, this integration can be approximated as the Gaussian form,

$$h_{\mathrm{p}}(d, z) \approx \tilde{h}_{\mathrm{p}}(d; z) = A_0 \exp\left(-\frac{2d^2}{w_{z_{eq}}^2}\right), \tag{2.13}$$

where

$$v = (\sqrt{\pi}a)/(\sqrt{2}w_z), \quad A_0 = [\mathrm{erf}(v)]^2, \quad \text{and} \quad w_{z_{eq}}^2 = w_z^2 \frac{\sqrt{\pi}\,\mathrm{erf}(v)}{2\,v\exp(-v^2)}.$$

Notice that A_0 is the fraction of the collected power at $d = 0$ and $w_{z_{eq}}$ is the equivalent beamwidth. The exact (2.12) and the approximate (2.13) expressions for $h_{\mathrm{p}}(d)$ are

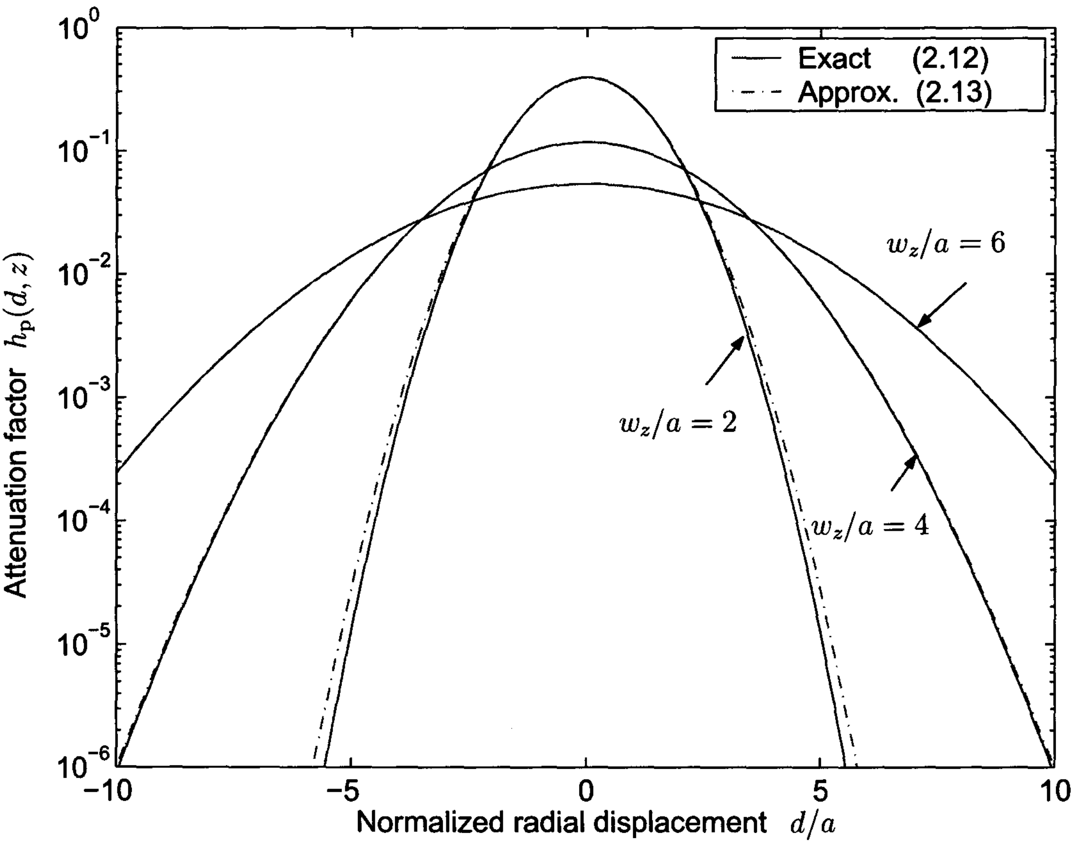

Figure 2.5: Exact and approximate values of $h_p(d, z)$ for different values of w_z/a versus the normalized radial displacement d/a.

plotted in Fig. 2.5 for different values of w_z/a. The normalized mean square error (NMSE) between the exact (2.12) and the approximate expressions (2.13) for h_p are given in Table 2.2 for different values of w_z/a as a measure for the approximation accuracy. The NMSE is defined as

$$\text{NMSE} = \frac{\sum (h_p - \tilde{h}_p)^2}{\sum h_p^2}$$

where h_p and $\tilde{h}_p$ are the exact and the approximate expressions. It can be deduced that the proposed approximation is close to the exact expression when $w_z/a \geq 2$.

Table 2.2: Normalized mean square error (NMSE) between exact and approximate h_p expressions

w_z/a	2	4	6
NMSE	10^{-4}	4×10^{-6}	6×10^{-7}

In order to relate this work to previous work, consider the case when $w_z \gg a$. This is the situation when a point detector is considered. The limiting expression for $h_\text{p}(d, z)$ as $a/w_z \to 0$, i.e., $v \to 0$ and $\text{erf}(v) \to 2v/\sqrt{\pi}$, is given as,

$$\lim_{a/w_z \to 0} h_\text{p}(d, z) = \underbrace{\pi a^2}_{\text{Detector Area}} \cdot \underbrace{I_{beam}(\boldsymbol{d}; z)}_{\text{Irradiance Sample at } \boldsymbol{d}}.$$

That is the attenuation $h_\text{p}(d, z)$ at a displacement d is simply the intensity of a Gaussian beam sampled at radial distance d multiplied by the detector area as commonly used when a point receiver is considered in previous work.

Consider independent identical Gaussian distribution for the elevation and the horizontal displacement (sway), as was done in previous work [51]. The radial displacement d at the receiver is modeled by a Rayleigh distribution

$$f_d(d) = \frac{d}{\sigma_s^2} \exp\left(-\frac{d^2}{2\sigma_s^2}\right) \qquad r > 0, \tag{2.14}$$

where σ_s^2 is the jitter variance at the receiver. Combining (??) and (2.14) the probability distribution of h_p can be expressed as,

$$f_{h_\text{p}}(h_\text{p}) = \frac{\gamma^2}{A_0^{\gamma^2}}\, h_\text{p}^{\gamma^2 - 1}, \qquad 0 \leq h_\text{p} \leq A_0 \tag{2.15}$$

where $\gamma = w_{z_{eq}}/2\sigma_s$ is the ratio between the equivalent beam radius at the receiver and the pointing error displacement standard deviation at the receiver. Note that it is possible to consider other distributions for the jitter and the proposed expression for h_p is a general frame work for misalignment channel modeling.

2.7 Channel Statistical model

A weather condition is parameterized by the vector $\phi = \{C_n^2, \nu, z\}$. The probability distribution of the channel $H = h_\ell H_\mathrm{a} H_\mathrm{p}$ can be expressed as,

$$f_H(h; w_o, \phi) = \int f_{H|H_\mathrm{a}}(h|h_\mathrm{a})\, f_{H_\mathrm{a}}(h_\mathrm{a})\, dh_\mathrm{a}, \tag{2.16}$$

where $f_H(h; w_o, \phi)$ is a family of pdfs parameterized by the Gaussian beam waist at the transmitter w_o and $f_{H|H_\mathrm{a}}(h|h_\mathrm{a})$ is the conditional probability given a turbulence state $H_\mathrm{a} = h_\mathrm{a}$. Note that h_ℓ acts as a scaling factor. The resulting conditional distribution can be expressed as,

$$\begin{aligned} f_{H|H_\mathrm{a}}(h|h_\mathrm{a}) &= \frac{1}{h_\mathrm{a} h_\ell} f_{H_\mathrm{p}}\left(\frac{h}{h_\mathrm{a} h_\ell}\right) \\ &= \frac{\gamma^2}{A_0^{\gamma^2} h_\mathrm{a} h_\ell}\left(\frac{h}{h_\mathrm{a} h_\ell}\right)^{\gamma^2 - 1} \qquad 0 \le h \le A_0 h_\mathrm{a} h_\ell. \end{aligned} \tag{2.17}$$

Substituting (2.17) into (2.16) gives,

$$f_H(h; w_o, \phi) = \frac{\gamma^2}{(A_0\, h_\ell)^{\gamma^2}}\, h^{\gamma^2 - 1} \int_{h/A_0 h_\ell}^{\infty} h_\mathrm{a}^{-\gamma^2} f_{h_\mathrm{a}}(h_\mathrm{a})\, dh_\mathrm{a}. \tag{2.18}$$

The channel state distribution $f_H(h; w_o, \phi)$ can now be computed by substituting different statistical models for atmospheric turbulence, $f_{H_\mathrm{a}}(h_\mathrm{a})$ into (2.18).

For weak turbulence ($\sigma_R^2 < 0.3$), $f_{H_\mathrm{a}}(h_\mathrm{a})$ has a log-normal distribution (2.2). Substituting into (2.18) gives,

$$f_H(h; w_o, \phi) = \frac{\gamma^2}{(A_0 h_\ell)^{\gamma^2}}\, h^{\gamma^2 - 1} \int_{h/A_0 h_\ell}^{\infty} h_\mathrm{a}^{-\gamma^2} \frac{1}{2 h_\mathrm{a} \sqrt{2\pi\sigma_\chi^2}} \exp\left(-\frac{(\ln h_\mathrm{a} + 2\sigma_\chi^2)^2}{8\sigma_\chi^2}\right) dh_\mathrm{a}.$$

This expression can be further simplified. Let $\mu = 2\sigma_\chi^2(1 + 2\gamma^2)$ then,

$$f_H(h; w_o, \phi) = \frac{\gamma^2}{2(A_0 h_\ell)^{\gamma^2}}\, h^{\gamma^2 - 1} \mathrm{erfc}\left(\frac{\ln(\frac{h}{A_0 h_\ell}) + \mu}{\sqrt{8}\sigma_\chi}\right) e^{\left(2\sigma_\chi^2 \gamma^2 (1 + \gamma^2)\right)}.$$

In strong turbulence regime $f_{H_a}(h_a)$ has a Gamma-Gamma distribution. Substituting (2.4) into (2.18) results in,

$$f_H(h; w_o, \phi) = \frac{2\gamma^2(\alpha\beta)^{(\alpha+\beta)/2}}{(A_0 h_\ell)^{\gamma^2}\Gamma(\alpha)\Gamma(\beta)} h^{\gamma^2-1} \int_{h/A_0 h_\ell}^{\infty} h_a^{(\alpha+\beta)/2-1-\gamma^2} \mathrm{K}_{\alpha-\beta}(2\sqrt{\alpha\beta\, h_a})\, dh_a. \tag{2.19}$$

This integration can be expanded into a complex expression of hypergeometric functions, however, in this thesis, numerical integration is utilized to compute the integral. For completeness, an expression for (2.19) is given in [96] in terms of Meijers G-function which can be written in terms of the more familiar generalized hypergeometric functions.

2.8 Conclusion

Accurate channel modeling for a wireless communication system is one of the key elements in system design. In this chapter a statistical model for the FSO channel considering the combined effect of atmospheric turbulence and time varying misalignment is developed. The model considers the beamwidth, detector size and misalignment parameters. This model enables the system designer to use more degrees of freedom to optimally design FSO systems. In Chapter 6 the developed model will be utilized to study the outage capacity of FSO channels where significant gain in rate and an order of magnitude reduction in the probability of outage are shown with beamwidth optimization.

Chapter 3

Capacity Bounds Under an Average Optical Power Constraint

Coding for optical channels can significantly mitigate the effect of atmospheric turbulence and misalignment fading [36, 74]. In order to design channel coding and signaling, the channel capacity must be computed. The channel capacity is the maximum reliable data rate that can be transmitted over a communication channel. The maximization is performed over the input distribution under input signal constraints. When the capacity expression is mathematically intractable and complex, which is the case for the optical channel under investigation, an alternative method is to tightly bound the channel capacity.

In this chapter, bounds on the capacity of wireless optical intensity pulse amplitude modulation (PAM) channels under non-negativity and average optical power constraints are developed. Based on the developed bounds, non-uniform signaling achieves higher rates compared to uniform schemes. The developed bounds are tighter than previous reported bounds over a wide range of SNRs.

3.1 Introduction

As discussed in Section 1.4.2, the capacity of optical intensity channels with non-negativity and average power constraints is an open problem where lower and upper bounds are developed to asymptotically describe the behavior of the channel capacity [60,62,64,66,108]. However, in previous work, a significant gap between the lower and the upper bounds is noticed especially at low and moderate SNRs. Furthermore, the highest reported rates in low and moderate SNR ranges were achieved using both one-sided exponential and 2-PAM signaling. However, other signaling schemes were not investigated although it was shown that discrete distributions are capacity-achieving distributions for many channels [67–72, 74].

In this chapter, tight upper and lower bounds on the capacity of pulse amplitude modulated (PAM) wireless optical intensity channels are derived. Using the fact that a discrete distribution is capacity-achieving for Gaussian channels with bounded input [67], we consider a family of discrete input distributions with equally spaced mass points. Within this family the maxentropic input distribution under average power constraint is chosen. Although not necessarily capacity-achieving, these distributions are shown to provide a tight lower bound on the capacity of wireless optical intensity channels over a wide range of SNRs. In addition, an analytic upper bound on the channel capacity is derived using a sphere packing argument. Under non-negativity and average optical power constraints, the admissible transmitted signal region is a regular n-simplex. Unlike previous work [60], the Minkowski sum [109] of convex bodies is utilized to obtain the exact volume of the outer parallel body at a fixed distance from a regular n-simplex. The derived upper bound is tighter than previous bounds [60] at low SNRs. The tightness of the derived bounds at low SNR provides a useful benchmark for communication system design.

3.2 Channel Capacity Lower Bound

Recall the discrete representation of the optical channels in (1.2) given by

$$Y = HX + Z, \tag{3.1}$$

where, without loss of generality, both η and R_v are set to unity since they are scaling factors. The non-negativity and average optical power constraints are expressed as

$$X \geq 0, \quad \text{and} \quad \mathbb{E}\{X\} \leq P,$$

where P is the average power limit. The optical SNR at a given channel realization $H = h$ is [60]

$$\text{SNR}(h) = \frac{Ph}{\sigma}.$$

Since the FSO channels are slow-fading channels, it is assumed that the receiver has a perfect channel state information (CSI).

The capacity of the wireless optical intensity channel is the maximum mutual information, $\mathbb{I}(X;Y)$, between channel input and output over all possible input distributions, $f_X(x)$, satisfying the non-negativity and average optical power constraints. Consider the Gaussian channel model given in (3.1). The mutual information, in bits/channel use, between channel input and output for a given a channel realization $H = h$ is defined as

$$\mathbb{I}(X;Y|H=h) = \int\int f_{Y|H,X}(y|h,x) f_X(x) \cdot \log_2 \frac{f_{Y|H,X}(y|h,x)}{f_{Y|H}(y|h)} \, dx \, dy, \tag{3.2}$$

where

$$f_{Y|H,X}(y|h,x) = \mathcal{N}(h\,x, \sigma^2),$$
$$f_{Y|H}(y|h) = \int_x f_X(x) f_{Y|H,X}(y|h,x) \, dx,$$

and $\mathcal{N}(\nu, \zeta^2)$ denotes a Gaussian distribution with mean ν and variance ζ^2. Let $\mathcal{F}$ denote the family of all input distributions satisfying the non-negativity and average optical power constraints. The instantaneous channel capacity, $\mathcal{C}(h)$, for a given channel state h, is the maximum mutual information over the set $\mathcal{F}$ and is given by

$$\mathcal{C}(h) = \max_{f_X(x) \in \mathcal{F}} \mathbb{I}(X;Y|H=h), \tag{3.3}$$

where

$$\mathcal{F} = \left\{ f_X(x) : f_X(x<0) = 0, \mathbb{E}\{X\} \leq P, \int f_X(x)\, dx = 1 \right\}.$$

It was shown in [67,74] that the capacity-achieving distribution for conditional Gaussian channels under average electrical power and bounded-input constraints is discrete with a finite number of mass points. Although no peak amplitude is considered in this chapter, discrete distributions are considered based on the intuition that they would perform well over the optical channels. Furthermore, there are efficient algorithms to implement discrete distributions as will be shown in Chapter 5. Consider confining the input distribution to the set of *discrete* distributions $\mathcal{Q}$ defined as

$$\mathcal{Q} = \left\{ q(x) : a_k > 0, x_k \geq 0, \sum_{k=0}^{\infty} a_k\, x_k \leq P,\ q(x) = \sum_{k=0}^{\infty} a_k\, \delta(x - x_k) \right\},$$

where $\delta(\cdot)$ is the Dirac delta functional, a_k and x_k are the amplitude and position of the k^{th} mass point. Optimizing the mutual information over $\mathcal{Q}$ results in a nonlinear optimization problem where no analytical form for the mutual information maximizing input distribution $q(x)$ can be obtained. Consider instead the set $\mathcal{Q}_\ell \subset \mathcal{Q}$ such that the discrete mass points are equally spaced at a given distance $\ell > 0$, i.e.,

$$\mathcal{Q}_\ell = \left\{ q_\ell(x) \in \mathcal{Q} : a_k \geq 0,\ q_\ell(x) = \sum_{k=0}^{\infty} a_k \delta(x - k\ell) \right\}.$$

Although the capacity achieving distribution need not be in $\mathcal{Q}_\ell$, the proposed form simplifies the analysis of the channel capacity. Note that all $q_\ell(x) \in \mathcal{Q}_\ell$ satisfy the non-negativity and the average optical power constraints. Also any $q_\ell(x) \in \mathcal{Q}_\ell$ can provide a lower bound on the channel capacity. In the analysis, the maxentropic input distribution in $\mathcal{Q}_\ell$ is considered since the mutual information of this input distribution is close to the channel capacity at high SNR. The discrete entropy of X with input distribution $q_\ell(x) \in \mathcal{Q}_\ell$ is defined as

$$\mathbb{H}(X) = \sum_{k=0}^{\infty} a_k \log_2 \frac{1}{a_k}.$$

The problem is formulated as follows,

$$q_\ell(x) \triangleq \arg \max_{q_\ell(x)\in\mathcal{Q}_\ell} \mathbb{H}(X),$$
$$\text{s.t} \quad a_k \geq 0, \quad \sum_{k=0}^{\infty} a_k = 1, \quad \sum_{k=0}^{\infty} k\ell a_k \leq P. \tag{3.4}$$

Define $\mathcal{J}$ as the Lagrangian associated with the optimization problem as

$$\mathcal{J} = \sum_{k=0}^{\infty} a_k \log_2 \frac{1}{a_k} - \lambda_1 \left(\sum_{k=0}^{\infty} a_k - 1 \right) - \lambda_2 \left(\sum_{k=0}^{\infty} k\ell a_k - P \right).$$

Applying the method of Lagrange multipliers, setting $\partial\mathcal{J}/\partial a_k = 0$, and using the constraints in (3.4) , it is straightforward to show that the maxentropic distribution is given by,

$$q_\ell(x) = \sum_{k=0}^{\infty} \underbrace{\frac{\ell}{\ell+P} \left(\frac{P}{\ell+P} \right)^k}_{a_k^*} \delta(x - k\ell), \tag{3.5}$$

where $\{a_k^*\}$ is the collection of weights for mass points. Notice that although $q_\ell(x)$ is a family of distributions parameterized in ℓ, the mean, i.e., average optical power, is P independent of ℓ. For a given P and σ, a capacity lower bound can be found by maximizing the mutual information (3.2) over the input distribution $f_X(x) \in \mathcal{Q}_\ell$ or more precisely the mass point spacing ℓ. The corresponding input distribution is given by,

$$q_\ell^*(x) = \arg \max_{f_X(x)\in\mathcal{Q}_\ell} \mathbb{I}(X; Y|H = h). \tag{3.6}$$

In order to simplify the analysis and give insight into the problem, consider the scaled output $G = Y/h\ell$ where the output noise remains Gaussian with zero mean but with variance β^2 where,

$$\beta = \sigma/h\ell.$$

Since the mutual information is invariant to scaling then

$$\mathbb{I}_{q_\ell}(X;Y|H=h) = \mathbb{I}_{q_\ell}(X;G|H=h) = -\int f_G(g)\log_2 f_G(g)dg - \frac{1}{2}\log_2(2\pi e\beta^2),$$

where

$$f_G(g) = \sum_{k=0}^{\infty} \frac{1}{1+\beta\frac{Ph}{\sigma}} \left(\frac{\beta\frac{Ph}{\sigma}}{1+\beta\frac{Ph}{\sigma}}\right)^k \frac{1}{\sqrt{2\pi\beta^2}} e^{-(g-k)^2/2\beta^2}.$$

Notice that for a given Ph/σ the reformulated mutual information is parameterized by β. This formulation transforms the original scenario to an equivalent Gaussian noise channel with noise variance β^2 and input distribution,

$$\bar{q}_\beta(x) = \sum_{k=0}^{\infty} \left[\frac{1}{1+\beta\frac{Ph}{\sigma}} \left(\frac{\beta\frac{Ph}{\sigma}}{1+\beta\frac{Ph}{\sigma}}\right)^k\right] \delta(x-k).$$

As noticed the noise and the input distribution are parameterized by β. Considering any arbitrary value for β, the resulting mutual information is presented as a lower bound on the channel capacity. For a given SNR, the best lower bound on the channel capacity C_{L} is obtained by maximizing the mutual information over the input distribution, or equivalently the best choice of β as follows,

$$C_{\mathrm{L}}(\mathrm{SNR}) = \max_{\beta}\ \mathbb{I}(X;Y|H=h), \tag{3.7}$$

where the optimum value of β at a given SNR is expressed as,

$$\beta^*(\mathrm{SNR}) = \arg\max_{\beta}\quad \mathbb{I}(X;Y|H=h). \tag{3.8}$$

For a given Ph/σ, this maximization can be solved numerically using an exhaustive search or directed search method in an interval. Notice, however, that for any selection of β, the resulting $\mathbb{I}(X;Y|H=h)$ remains a valid lower bound. In Sec. 3.4.2 a simple closed form approximation to β^* as a function of SNR is presented. Although no analytical form is provided, C_{L} can be computed efficiently through numerical integration.

3.3 Channel Capacity Upper Bound

In this section an upper bound on the channel capacity is derived using a sphere packing argument [63]. Consider the non-negativity and average optical power constraints, the set of transmissible codewords is presented geometrically by a regular n-simplex in the n-dimensional signal space [64]. For conditionally Gaussian channels, the signal space of the received codewords is defined by the parallel body to this regular n-simplex at fixed distance. The maximum achievable rate can be upper bounded by the maximum asymptotic number of non-overlapping spheres that can be packed in the outer volume (sphere packing argument). Based on a sphere packing argument, an analytical upper bound on the channel capacity in the presence of Gaussian noise is derived. Unlike [60] where the volume is bounded by an n-simplex, the Minkowski sum [109] of convex bodies is utilized to obtain the volume of the outer parallel body at fixed distance from the regular n-simplex. The derived upper bound is tight at low SNR and asymptotically describes the channel capacity behavior.

3.3.1 Set of Received Codewords and Volumes

Consider transmitting a sequence of n independent PAM symbols to form the codeword $\boldsymbol{x} = (x_1, x_2, \ldots, x_n)$. The admissible set of transmitted codewords satisfying non-negativity and average amplitude constraints, forms the regular n-simplex $\Psi(P)$ defined by [64]

$$\Psi(P) = \left\{ \boldsymbol{x} \in \mathbb{R}^n : \forall i \; x_i \geq 0, \; \frac{1}{n}\sum_{i=1}^{n} x_i \leq P \right\}.$$

According to the Gaussian noise model presented, conditioned on $\boldsymbol{x}$ and the channel state h the received vector $\boldsymbol{y}$ has a Gaussian distribution with mean $h\boldsymbol{x}$ as follows,

$$\boldsymbol{y} = h\boldsymbol{x} + \boldsymbol{z}$$

where $\boldsymbol{z} = (z_1, z_2, \ldots, z_n)$ has i.i.d. Gaussian components. Since in this chapter the capacity bounds are derived for a given channel realization h, i.e., h only scales the SNR, then, and for the balance of the analysis, h is set to unity and its effect will be considered in the final expression of the capacity upper bound. Asymptotically, with identically distributed independent noise components in each dimension then

$$\lim_{n\to\infty} \frac{1}{n} \|\boldsymbol{z}\|^2 \to \sigma^2$$

In signal space representation, for n large enough, the received vector $\boldsymbol{y}$ can be viewed as a cloud of radius ϱ centered at point $\boldsymbol{x}$ in the n-dimensional space where

$$\varrho = \sqrt{n\sigma^2}$$

Define $\mathcal{B}_n$ as the n-dimensional unit ball given by,

$$\mathcal{B}_n = \left\{ \mathrm{b} \in \mathbb{R}^n : \|\boldsymbol{b}\|^2 = 1 \right\}.$$

Also define the set $\Phi(P, \varrho)$ as the collection of vectors $\boldsymbol{y}$, formally,

$$\Phi(P, \varrho) = \left\{ \boldsymbol{y} \in \mathbb{R}^n : \boldsymbol{y} = \boldsymbol{x} + \boldsymbol{b},\ \boldsymbol{x} \in \Psi(P),\ \mathrm{b} \in \varrho\mathcal{B}_n \right\}.$$

The region defined by $\Phi(P, \varrho)$, when n large, is termed the outer parallel body to $\Psi(P)$ at distance ϱ and is the result of the Minkowski sum of $\Psi(P)$ and $\varrho\mathcal{B}_n$. Figure 3.1(a) presents a two-dimensional example of $\Psi(P)$ and $\Phi(P, \varrho)$. An upper bound for the wireless optical intensity channel capacity can be obtained by applying a sphere-packing argument to find the maximum number of non-overlapping spheres that can be packed in $\Phi(P, \varrho)$ as $n \to \infty$ as illustrated in Fig. 3.1(b) when $n = 3$. Let $V(\cdot)$ denote the volume of a closed set. The volume of a sphere with radius ϱ is given by,

$$V\big(\varrho\mathcal{B}_n\big) = \kappa_n \varrho^n = \frac{\pi^{n/2}}{\Gamma(\frac{n}{2}+1)} \varrho^n$$

where $\kappa_n = V\big(\mathcal{B}_n\big)$ and $\Gamma(\cdot)$ is the Gamma function . The channel capacity can thus be bounded as,

$$C \le \lim_{n\to\infty} \frac{1}{n} \log_2 \frac{V\big(\Phi(P, \varrho)\big)}{V\big(\varrho\mathcal{B}_n\big)} \qquad \text{bits/channel use.}$$

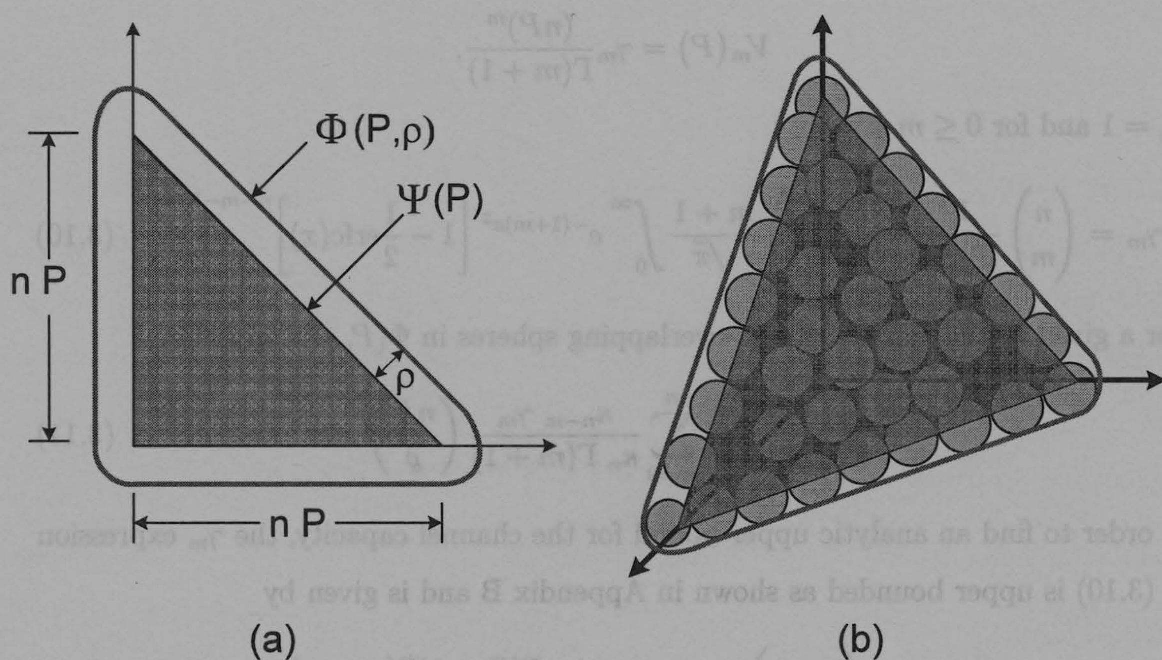

Figure 3.1: (a) 2-D representation of an n-simplex and its parallel body at distance ϱ, (b) 3-D illustrative diagram for sphere packing in the volume $\Phi(P, \varrho)$.

3.3.2 Volume Approximation

The volume $V(\Phi(P,\varrho))$ can be expressed in terms of the intrinsic volumes $V_m(P)$ of an n-simplex as [109],

$$V(\Phi(P,\varrho)) = \sum_{m=0}^{n} V_m(P) V(\varrho\mathcal{B}_{n-m}), \tag{3.9}$$

where

$$V_m(P) = \gamma_m \frac{(nP)^m}{\Gamma(m+1)},$$

$\gamma_n = 1$ and for $0 \le m < n$

$$\gamma_m = \binom{n}{m}\frac{1}{2^{n-m}} + \binom{n}{m+1}\frac{m+1}{\sqrt{\pi}}\int_0^{\infty} e^{-(1+m)x^2}\left[1-\frac{1}{2}\mathrm{erfc}(x)\right]^{n-m-1} dx. \tag{3.10}$$

For a given n, the number of non-overlapping spheres in $\Phi(P,\varrho)$ is given by

$$\frac{V(\Phi(P,\varrho))}{V(\varrho\mathcal{B}_n)} = \sum_{m=0}^{n} \frac{\kappa_{n-m}\,\gamma_m}{\kappa_n\,\Gamma(m+1)}\left(\frac{nP}{\varrho}\right)^m. \tag{3.11}$$

In order to find an analytic upper bound for the channel capacity, the γ_m expression in (3.10) is upper bounded as shown in Appendix B and is given by

$$\begin{aligned}\gamma_m &< \binom{n+1}{m+1}(m+1)(\sqrt{e})^m \frac{\Gamma(\frac{m}{2}+1)\Gamma(n-m)}{\Gamma(n-\frac{m}{2}+1)} \\ &= \lambda_m.\end{aligned}$$

Substituting into (3.11) results in

$$\frac{V(\Phi(P,\varrho))}{V(\varrho\mathcal{B}_n)} < \sum_{m=0}^{n} \frac{\kappa_{n-m}\,\lambda_m}{\kappa_n\,\Gamma(m+1)}\left(\frac{nP}{\varrho}\right)^m.$$

In order to simplify the notation let $\mathbb{Z}_n^+ = \{0,1,\ldots,n\}$ and define $\psi(m,n)$ as

$$\psi(m,n) = \frac{\kappa_{n-m}\,\lambda_m}{\kappa_n\,\Gamma(m+1)}\left(\frac{nP}{\varrho}\right)^m.$$

Then the capacity can be upper bounded as follows,

$$
\begin{aligned}
C &\leq \lim_{n\to\infty} \frac{1}{n} \log_2 \frac{V(\Phi(P,\varrho))}{V(\varrho\mathcal{B}_n)}, \\
&< \lim_{n\to\infty} \frac{1}{n} \log_2 \left[\sum_{m=0}^{n} \psi(m,n)\right], \\
&\leq \lim_{n\to\infty} \frac{1}{n} \log_2 \left[n \sup_{m\in\mathbb{Z}_n^+} \psi(m,n)\right], \\
&= \lim_{n\to\infty} \frac{1}{n} \log_2 \left[\sup_{m\in\mathbb{Z}_n^+} \psi(m,n)\right], \\
&= \lim_{n\to\infty} \sup_{m\in\mathbb{Z}_n^+} \frac{1}{n} \log_2 \left[\psi(m,n)\right], \qquad (3.12)
\end{aligned}
$$

where the last inequality is due to the monotonic increase of the $\log(\cdot)$ function. Define $\mathbb{Q}_n$ as the set of rational numbers of the form

$$
\mathbb{Q}_n = \left\{\alpha : \alpha = \frac{m}{n},\ m = 0,\ldots,n\right\}, \qquad (3.13)
$$

and let

$$
\psi(\alpha n, n) = \frac{\kappa_{(1-\alpha)n}\,\lambda_{\alpha n}}{\kappa_n\,\Gamma(\alpha n+1)} \left(\frac{nP}{\varrho}\right)^{\alpha n}, \ \alpha \in \mathbb{Q}_n
$$

$$
\phi(\alpha, n) = \frac{1}{n} \log_2 \left[\frac{\kappa_{(1-\alpha)n}\,\lambda_{\alpha n}}{\kappa_n\,\Gamma(\alpha n+1)} \left(\frac{nP}{\varrho}\right)^{\alpha n}\right], \ \alpha \in [0,1].
$$

Substituting into (3.12) gives,

$$
\begin{aligned}
C &< \lim_{n\to\infty} \sup_{m\in\mathbb{Z}_n^+} \frac{1}{n} \log_2 \left[\psi(m,n)\right], \\
&= \lim_{n\to\infty} \sup_{\alpha\in\mathbb{Q}_n} \frac{1}{n} \log_2 \left[\psi(\alpha n,n)\right], \\
&\leq \lim_{n\to\infty} \sup_{\alpha\in[0,1]} \left[\phi(\alpha,n)\right],
\end{aligned}
$$

where the last inequality arises due to the relaxation $\alpha \in [0,1]$ since $\mathbb{Q}_n \subset [0,1]$.

Lemma 3.1 *The limit of $\phi(\alpha,n)$ as $n \to \infty$ exists for all $\alpha \in [0,1]$ i.e.,*

$$\lim_{n\to\infty} \phi(\alpha,n) = \log_2\left[\left(\sqrt{\frac{e^2}{4\pi}}\right)^{\alpha}\left(\frac{P}{\sigma}\right)^{\alpha}\frac{1}{\Theta(\alpha)}\right],$$

where

$$\Theta(\alpha) = \alpha^{\frac{3\alpha}{2}}\ (1-\alpha)^{\frac{(1-\alpha)}{2}}\ \left(1-\frac{\alpha}{2}\right)^{(1-\frac{\alpha}{2})}.$$

Proof. See Appendix D. ■

Proposition 3.1 *Given that the limit of $\phi(\alpha,n)$ as $n \to \infty$ exists for all $\alpha \in [0,1]$,*

$$\lim_{n\to\infty}\left[\sup_{\alpha}\ \phi(\alpha,n)\right] = \sup_{\alpha}\left[\lim_{n\to\infty}\ \phi(\alpha,n)\right].$$

Proof. See Appendix E. ■

The channel capacity upper bound can be written as,

$$\begin{aligned} C &< \lim_{n\to\infty}\ \sup_{\alpha\in[0,1]}\ \phi(\alpha,n), \\ &= \sup_{\alpha\in[0,1]}\ \lim_{n\to\infty}\ \phi(\alpha,n), \\ &= \sup_{\alpha\in[0,1]}\ \log_2\left[\left(\sqrt{\frac{e^2}{4\pi}}\right)^{\alpha}\left(\frac{P}{\sigma}\right)^{\alpha}\frac{1}{\Theta(\alpha)}\right]. \end{aligned} \tag{3.14}$$

The channel capacity upper bound at a given channel state h is given by,

$$C < \sup_{\alpha\in[0,1]}\ \log_2\left[\left(\sqrt{\frac{e^2}{4\pi}}\right)^{\alpha}\left(\frac{Ph}{\sigma}\right)^{\alpha}\frac{1}{\Theta(\alpha)}\right]. \tag{3.15}$$

In the following we show that there is a unique $\alpha^* \in [0,1]$ that maximizes the capacity upper bound given in (3.15) and explicitly present this value.

3.3.3 Uniqueness of α^*

Consider the objective function inside the supremum in (3.15) and define $J(\alpha)$ as,

$$J(\alpha) = \log_2 \left[\left(\sqrt{\frac{e^2}{4\pi}} \right)^\alpha \left(\frac{Ph}{\sigma} \right)^\alpha \frac{1}{\Theta(\alpha)} \right]. \tag{3.16}$$

It is straightforward to show that $J(\alpha)$ is a concave function in α in the interval $[0, 1]$, i.e., $\partial^2 J/\partial\alpha^2 < 0$ when $\alpha \in [0, 1]$. In order to find α^* that maximizes $J(\alpha)$, consider $\partial J/\partial\alpha = 0$ which results in

$$\alpha^3 - b\alpha^2 + 3b\alpha - 2b = 0,$$

where

$$b = \frac{1}{2} \exp \left(\log_2 \frac{e^2}{4\pi} \left(\frac{Ph}{\sigma} \right)^2 - 1 \right) \geq 0. \tag{3.17}$$

Proposition 3.2 *Let $\Lambda(\alpha) = \alpha^3 - b\alpha^2 + 3b\alpha - 2b$ then for all $b > 0$, there exists a unique root for $\Lambda(\alpha)$, denoted α^* in the interval $[0, 1]$.*

Proof. Since $\Lambda(\alpha)$ is continuous and $\Lambda(0) = -2b \leq 0$ and $\Lambda(1) = 1$, then from the intermediate value theorem there exists at least one root for $\Lambda(\alpha)$ in $[0, 1]$. The extrema α_+ and α_- of $\Lambda(\alpha)$ obtained via solving $\partial\Lambda(\alpha)/\partial\alpha = 0$ are given as,

$$\alpha_\pm = \frac{1}{3} \left(b \pm \sqrt{b^2 - 9b} \right)$$

Three possibilities exist for the extrema in $\mathbb{R}$ which depend on b: (i) $b < 9$, no real extrema, (ii) $b = 9$, one extremum and (iii) $b > 9$, two distinct extrema. To prove the existence of a unique root for $\Lambda(\alpha)$ in $[0, 1]$, it is sufficient to prove that $\alpha_\pm > 1$ for all values of $b \geq 9$. When $b = 9$ one extremum exist at $\alpha = 3$. For $b > 9$, consider the following lemma.

Lemma 3.2 *If $b > 9$ then $\alpha_\pm > 1$.*

Proof. Consider $b > 9$ then it is clear that $\alpha_+ > 3$. On the other hand, note that α_- is decreasing with b where

$$\frac{\partial \alpha_-}{\partial b} = \frac{1}{3}\left(1 - \frac{1}{\sqrt{1-9/b}}\right) < 0,$$

is negative when $b > 9$. Also the asymptotic value as $b \to \infty$ is greater than one, i.e.,

$$\lim_{b\to\infty} \alpha_- = \frac{3}{2} > 1,$$

As a result $\alpha_\pm > 1$ whenever $b > 9$. ■

Therefore, for all values of $b > 0$ there is a unique real root for $\Lambda(\alpha)$ in $[0,1]$ and is denoted as α^*. ■

Since $J(\alpha)$ is a concave function when $\alpha \in [0,1]$, the upper bound for the optical channel capacity in (3.15) can be written as,

$$C_{\mathrm{U}} = \log_2\left[\left(\sqrt{\frac{e^2}{4\pi}}\right)^{\alpha^*}\left(\frac{Ph}{\sigma}\right)^{\alpha^*}\frac{1}{\Theta(\alpha^*)}\right]. \tag{3.18}$$

The unique root $\alpha^* \in [0,1]$ can be obtained analytically by solving the cubic equation $\Lambda(\alpha) = 0$. Consider the procedure presented in [110] and let

$$\Lambda_o = \Lambda(b/3), \quad \delta^2 = (b^2 - 9b)/9, \quad h = 2\delta^3, \quad \mu = \sqrt{\Lambda_o^2 - h^2}.$$

For a given SNR, i.e., (3.17), α^* can be computed according to the following cases [110]:

(i) $\Lambda_o^2 > h^2$

$$\alpha^* = \frac{b}{3} + \frac{1}{\sqrt[3]{2}}\left[(-\Lambda_o + \mu)^{\frac{1}{3}} + (-\Lambda_o - \mu)^{\frac{1}{3}}\right] \tag{3.19}$$

(ii) $\Lambda_o^2 = h^2$

$$\alpha^* = \min\left\{\frac{b}{3} + \left(\frac{\Lambda_o}{2}\right)^{1/3}, \frac{b}{3} - 2\left(\frac{\Lambda_o}{2}\right)^{1/3}\right\} \tag{3.20}$$

(iii) $\Lambda_o^2 < h^2$

$$\alpha^* = \min_{i=0,1,2}\left\{\frac{b}{3} + 2\delta\cos\left[\frac{2\pi i}{3} + \frac{1}{3}\cos^{-1}\left(\frac{-\Lambda_o}{h}\right)\right]\right\}. \tag{3.21}$$

Thus for a given SNR the channel capacity (3.18) has a closed form expression.

3.4 Results

3.4.1 Capacity Bounds: Discussion and Comparisons

The lower bound, C_{L} (3.7), and upper bound, C_{U} (3.18), are plotted versus SNR in Fig. 3.2. The upper bound is found directly from (3.18) while the lower bound is computed numerically. The optimum β^* (3.8) used to obtain C_{L} is shown in Fig. 3.3. The maximization is carried out by discretizing the range $\beta \in (0,1]$ with an increment of $\Delta\beta = 5 \times 10^{-4}$. For each entry in the discrete set, the mutual information is computed numerically and an exhaustive search is executed to find β^* which maximizes $\mathbb{I}(X;Y|H=h)$. Notice that every choice of β^* results in a valid lower bound. The numerical integration is computed using the MATLAB® function `'QUAD'` [111, version 7.6] with a tolerance of 10^{-6}. For the balance of the thesis, the same setting is used for all numerical integrations.

In addition, the mutual information for uniform M-ary PAM and continuous exponential distributions C_{E} [60] previously proposed as lower bounds are also plotted. Also a recently proposed lower bound, M_{L}, derived by applying the entropy power inequality (EPI) to the continuous exponential distribution is also presented [61, Eqn. (3.26)]. Notice that C_{L} is significantly tighter than the previous lower bounds C_{E} and M_{L} at both high and low SNR. The novelty of the developed lower bound is that the input distributions that realize the information rates presented by the lower bound are given explicitly in a simple closed form expression (3.5). Unlike C_{E} [60] where a single distribution is considered, the tightness of the developed lower bound C_{L} arises since a family of input distributions are considered. Although the lower bound M_{L} has a closed form, signaling schemes to achieve these rates are not known. The lower bound C_{L} has approximately double the mutual information (0.85 bits/channel use) compared to the continuous exponential C_{E} (0.42 bits/channel use) and the uniform 2-ary PAM (0.46 bits/channel use) at SNR=0 dB.

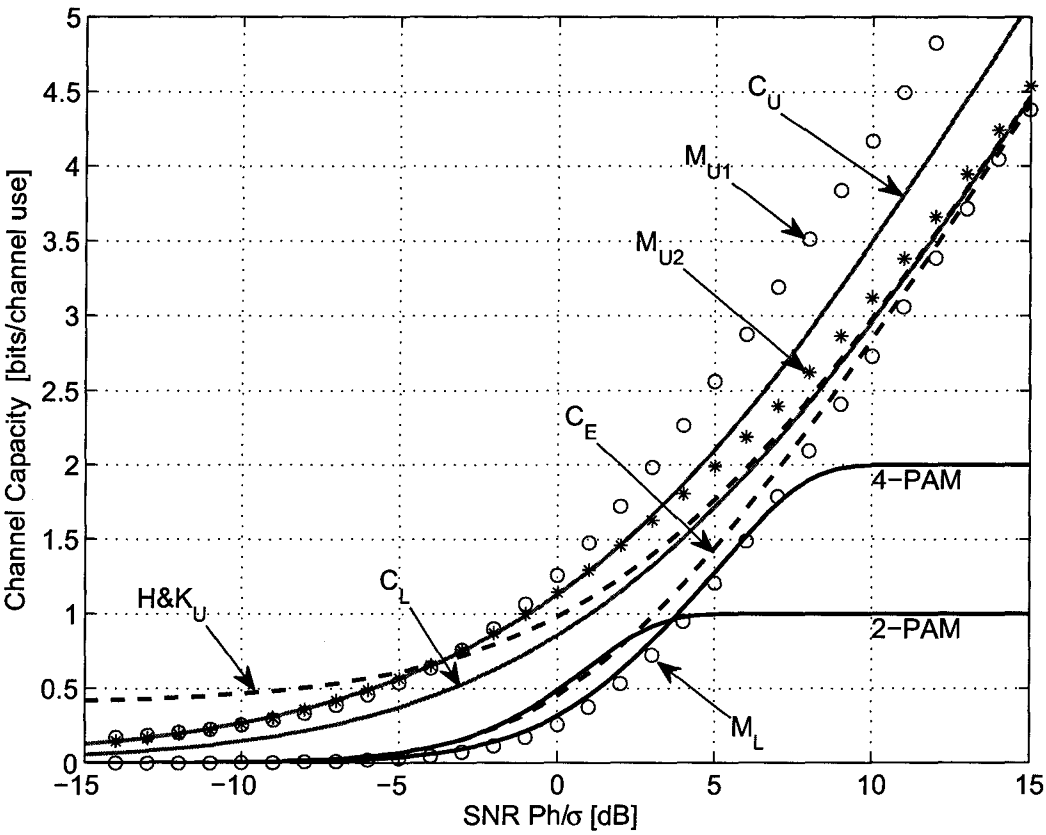

Figure 3.2: Average power constraint. Capacity bounds C_{L} and C_{U} and mutual information for continuous exponential [60], and discrete uniform PAM. For comparison, previously reported upper bounds $H\&K_{\mathrm{U}}$ [60, Eqn. (21)], M_{U1} [61, Eqn. (3.27)], M_{U2} [62, Eqn. (28)] and lower bound M_{L} [61, Eqn. (3.26)] are also presented.

The derived upper bound, $C_{\mathrm{U}} \rightarrow 0$ as $Ph/\sigma \rightarrow 0$ and asymptotically has a gap of $\log_2(\sqrt{e})$ in channel capacity at high SNRs compared to the tight upper bound $H\&K_{\mathrm{U}}$ [60, Eqn. (21)]. Notice that C_{U} provides a significantly better upper bound on the channel capacity compared to $H\&K_{\mathrm{U}}$ at low SNRs. In particular, when SNR < -3.46 dB C_{U} provides an insightful benchmark for different coding schemes comparisons since a majority of wireless optical intensity channels operate at low SNR regime. Although at low SNRs, both C_{U} and M_{U1} [61] have comparable performance, M_{U1} does not tend to zero as SNR $\rightarrow 0$. For completeness, the recent upper bound M_{U2} [62, Eqn. (28)] is presented in Fig. 3.2 as a modified version of M_{U1}. Although M_{U2} has a close performance to C_{U} at low SNR, i.e., SNR < 0 dB, the bound is computed through a complicated expression and there is no clear guideline on how the parameters involved in the expression were chosen. Hence, no clear insights about the bound behavior can be drawn. Contrary to M_{U2}, the proposed bound C_{U} has a simple closed form expression in this SNR range where α^* is uniquely defined by (3.19). At high SNR $H\&K_{\mathrm{U}}$ [60] is tighter to the lower bound C_{L} compared to M_{U2}. Furthermore, $H\&K_{\mathrm{U}}$ provides the tightest upper bound and the simplest closed form among all bounds when SNR > -3 dB. To summarize, the tightness of C_{U} at low SNR and its simple closed form expression are the key advantages when the bound is compared to all presented bounds.

3.4.2 Discussions on the Lower Bound

Fig. 3.3 shows that β^* varies from 0.25 to 0.45 over a wide range of SNRs (-20 to 20 dB). Note also any value for β results in a lower bound on the channel capacity and the maximization is used to find the tightest capacity lower bound.

The optimum mass point spacing $\ell^* = \sigma/h\beta^*$ is also presented in Fig. 3.3 for average optical powers $P = 0.5$, 1 and 2 and channel state $h = 1$. From Fig. 3.3 for a given P, ℓ^* can be approximated as a linear function of the SNR in the logarithmic

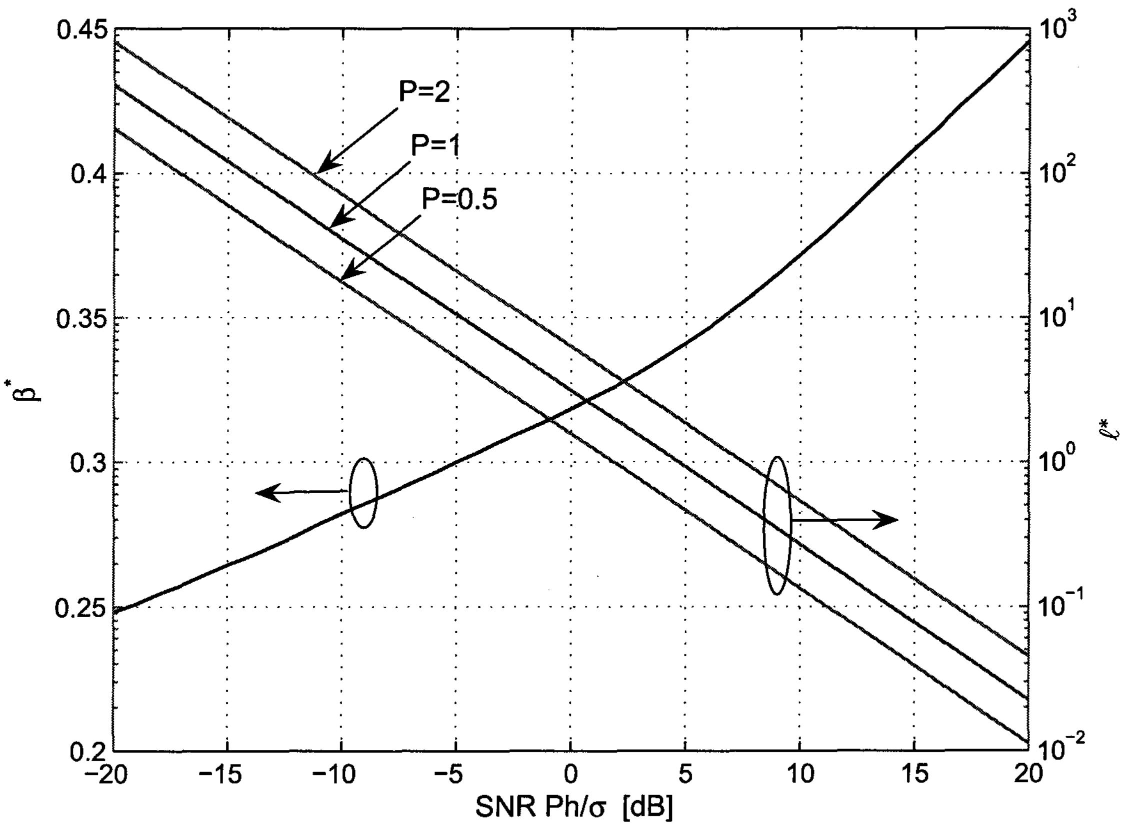

Figure 3.3: The optimum β^* and the corresponding optimum mass point spacing, ℓ^*, for $P = 0.5, 1, 2$ and $h = 1$ versus SNR.

domain. Define $\tilde{\ell}$ as the first order approximation for ℓ^* given as,

$$\log\left(\frac{\tilde{\ell}}{P}\right) = \log(c_1) + \log\left(\frac{Ph}{\sigma}\right)^{c_2} \tag{3.22}$$

where c_1 and c_2 are constants. This form is considered since for a given SNR, i.e., Ph/σ, the distribution, $q_\ell(x)$ in (3.5), that maximizes the mutual information depends on ℓ/P. The above form can be written as,

$$\tilde{\ell} = c_1 \left(\frac{Ph}{\sigma}\right)^{c_2} . P \tag{3.23}$$

These constants can be found through the linear least square regression [112] which results in $c_1 = 3.08$ and $c_2 = -1.06$ where the correlation coefficient between ℓ^* and $\tilde{\ell}$ using these values is

$$\text{Corr. Coeff.} = \frac{\langle \ell^* \tilde{\ell} \rangle - \langle \ell^* \rangle \langle \tilde{\ell} \rangle}{\sqrt{\langle \ell^{*2} \rangle - \langle \ell^* \rangle^2}\sqrt{\langle \tilde{\ell}^2 \rangle - \langle \tilde{\ell} \rangle^2}} = (1 - 1.5 \times 10^{-5}),$$

indicating an excellent fit. The resulting estimate for β^* is thus

$$\tilde{\beta} = \frac{1}{c_1}\left(\frac{Ph}{\sigma}\right)^{-c_2-1} \tag{3.24}$$

Using $\tilde{\beta}$, a new capacity lower bound is obtained and denoted $\tilde{C}_{\mathrm{L}}$. In simulation, the maximum difference between C_{L} and $\tilde{C}_{\mathrm{L}}$ is smaller than 2×10^{-4} bits/channel use for SNRs between -20 and 20 dB. Thus, (3.24) approximates the dependence of β^* on SNR and for practical purposes maximization over β to find C_{L} in (3.7) is not necessary.

Figure 3.4 plots the distribution $q^*_\ell(x)$ for different SNRs with $P = 1$. This scenario corresponds to optical wireless systems which typically operate at the maximum permissible optical power, which is limited by eye safety standards. At low SNR, this distribution consists of widely spaced mass points, i.e., ℓ^* is large, and few amplitudes contain nearly all of the probability mass. At higher SNRs, the spacing ℓ^* decreases, and a larger number of amplitudes carry significant probability mass. Quantitively, at low SNR the transmitter is turned off for a relatively long period of time to save the optical power and then is turned on to transmit high power for a short period of time that is capable to penetrate the high attenuation medium. Similar behavior is noticed for signal dependent noise [74, Fig. 2]. A common observation from [74] is the existence of mass point at amplitude zero. The fitting of ℓ^* to a linear model $\tilde{\ell}$ in (3.23) also provides the interesting intuition that ℓ^* is nearly inversely proportional to Ph/σ since $b \approx -1$. That is, for a given P and h, the spacing between mass points increases nearly linearly with σ.

3.4.3 Interpretations for the Upper Bound

Figure 3.5 shows the optimum $\alpha^* \in [0, 1]$ versus SNR. At low SNR, $\alpha \to 0$ implying $m \to 0$ through (3.13). The volume of the outer parallel body (3.9) is dominated by the first term in the summation, i.e., the volume of the ball $\varrho\mathcal{B}_n$. Intuitively this makes sense since at low SNR, ϱ is large and $\Phi(P, \varrho)$ approaches $\varrho\mathcal{B}_n$. At high SNR, $\alpha \to 1$ implying $m \to n$. Then $V(\Phi(P, \varrho))$ in (3.9) is dominated by the last term $m = n$ which is the volume of a regular n-simplex. Again, the corresponding intuition is that at high SNR ϱ is small and the volume of the Minkowski sum approaches that of the underlying simplex.

The figure also indicates which of the three cases (3.19)–(3.21) is employed to solve for α^* in C_{U}. At low and moderate SNR, (3.19) is selected while at higher SNRs (3.21) defines α^*. Note that when SNR increases beyond 0 dB the upper bound $H\&K_{\mathrm{U}}$ is the tightest bound among all presented upper bounds with the simplest form as well. Therefore, the proposed bound C_{U} can efficiently describe the channel capacity at low SNR where a closed form expression is presented with a simple unique equation for α^* in (3.19).

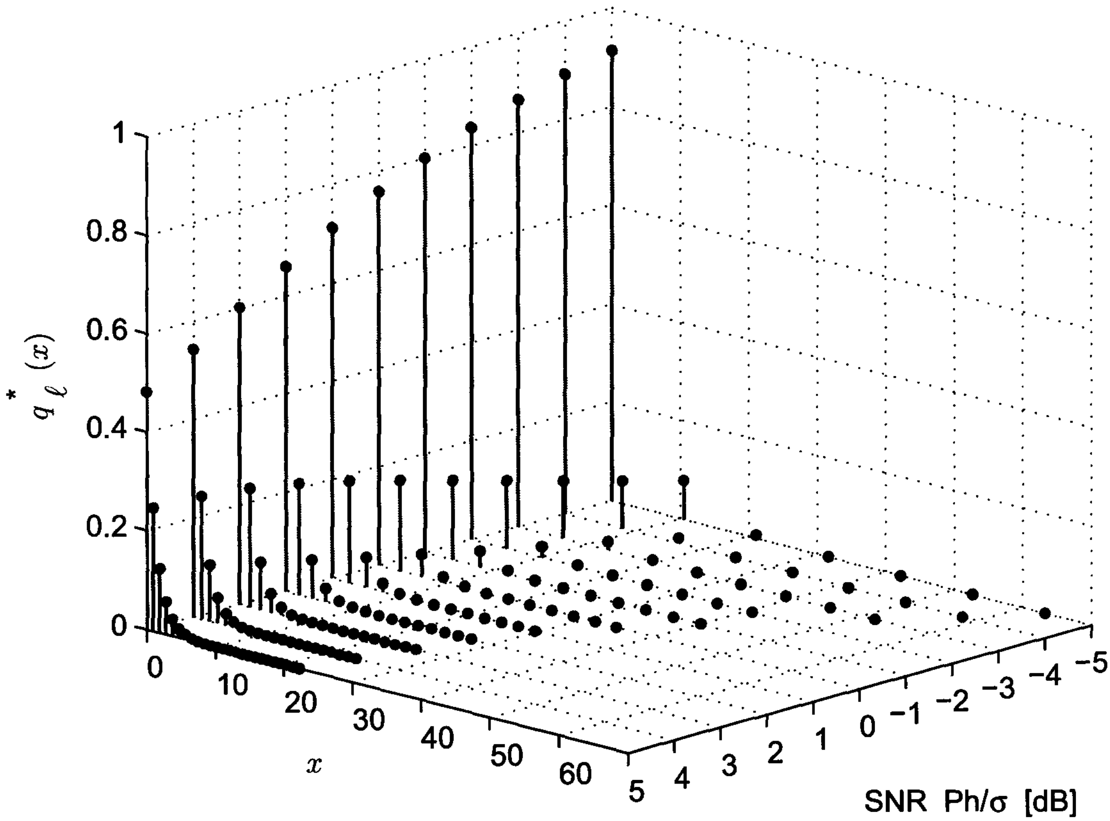

Figure 3.4: The proposed discrete distribution at different SNR for average optical power constraint P=1.

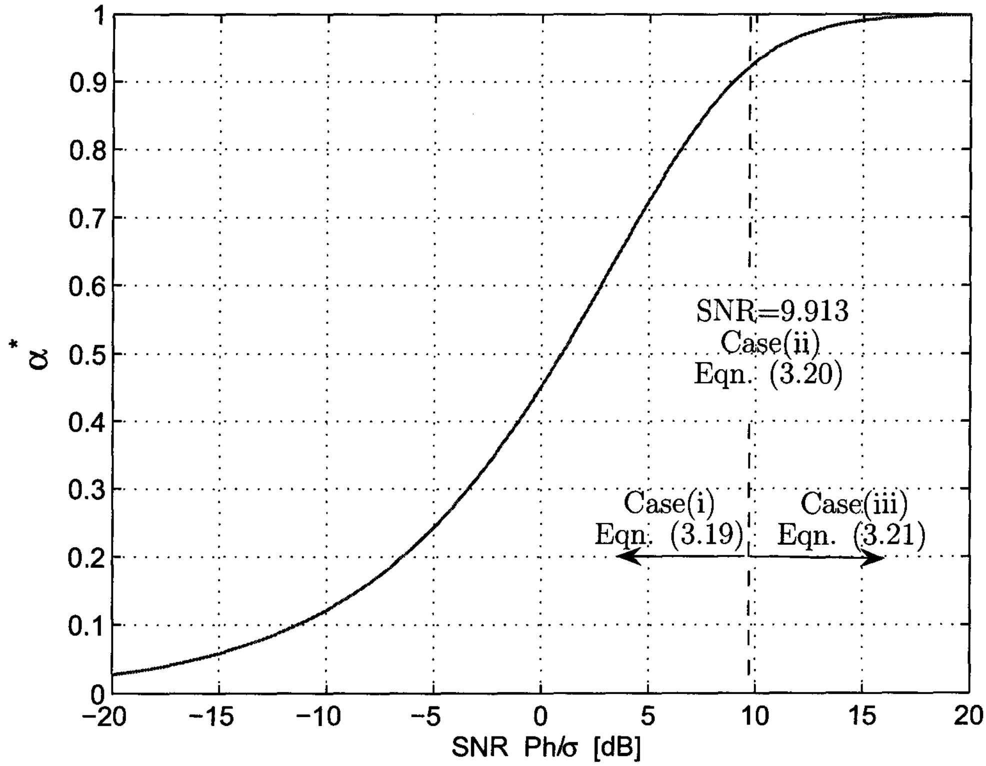

Figure 3.5: The optimum α^* for the capacity upper bound versus SNR.

3.5 Conclusion

In this chapter, lower and upper bounds on the instantaneous capacity at a given channel realization of PAM wireless optical intensity channels have been developed which are tight at low and high SNRs. Both non-negativity and average power (average amplitude) constraints are considered.

The lower bound is derived by considering a family of discrete distributions with equally spaced mass points that maximizes the input source entropy. Although no analytical closed-form expression for C_{L} is developed, the input distribution corresponding to this bound is given explicitly in a closed-form. In addition, an analytical upper bound on the channel capacity is derived based on a sphere packing argument. The bound is shown to be tighter than all previously proposed bounds at low SNR. The asymptotic behavior of the upper bound incurs a constant gap over the actual channel capacity at high SNRs. Moreover, discussions and interpretations for the parameters involved in the lower bound expression are presented and analyzed. In particular the parameter β and the spacing between the mass points for the proposed discrete distribution. First order approximations using a linear least square regression method is employed to provide an analytical expression for the optimum mass point spacing over a wide range of SNRs. The asymptotic behavior of the discrete distribution is also presented at different SNRs. Since most wireless optical links operate at relatively low SNRs, the tightness of the derived lower and upper bounds at low SNRs provides a useful benchmark for communication system design.

In practical systems, a peak amplitude constraint is considered to meet the physical dynamic range of a light source. In Chapter 4 channel capacity and input signaling design considering non-negativity, average power and peak amplitude constraints are analyzed. Following the same procedure, a family of input distributions are developed via source entropy maximization.

Chapter 4

Channel Capacity with Peak and Average Optical Power Constraints

Channel capacity bounds and signaling design for optical intensity channels considering non-negativity and average optical power constraints were developed in Chapter 3. In this chapter, a more general scenario where a peak optical power i.e., peak amplitude, constraint is added in addition to the previous mentioned constraints. This constraint is imposed to meet the physical dynamic range limits of light sources as well as amplifiers. This class of channels is very important and rarely studied in the literature. In previous work, lower and upper bounds on the channel capacity were developed [62], however, no input distributions were given and hence it is not clear how to achieve the lower bound rates. In this work, a closed form discrete capacity-approaching distribution is derived via entropy maximization. The computation of this distribution is substantially less complex than optimization approaches developed to find capacity-achieving distributions and can be easily computed for different SNRs. The information rates using the derived maxentropic distribution are shown through numerical simulations to be close to the channel capacity.

4.1 Introduction

As discussed in Section 1.4.3, although the discrete input distribution is a capacity-achieving distribution for many channels [70–73], analytical expressions are not available, and instead are found via complex optimization routines. However, numerical analysis is utilized to find the channel capacity for the sake of comparison. For optical intensity channels, lower and upper bounds on the channel capacity were developed in [61, 62]. Again, no explicit source distributions were provided, and hence no clear insights for communication system design can be drawn.

In this chapter, a family of non-uniform discrete source distributions with a finite number of equally spaced amplitude mass points whose mutual information is significantly close to the channel capacity is developed. The input distribution is derived via source entropy maximization criterion based on the intuition that it approaches the channel capacity at high SNRs. A closed form for the input distribution and the number of probability mass points are developed. As a result, and unlike the previous work mentioned above, signaling can be designed based on the developed distributions. For the sake of comparison and to measure how far the proposed distribution is from the channel capacity, the capacity-achieving distributions are computed numerically [67]. In this approach the capacity-achieving distribution varies for each SNR considered. It is shown via simulation that, the mutual information corresponding to the derived maxentropic input distributions is close to the channel capacity. Additional benefits of the developed distributions are that they provide capacity-approaching performance over a range of SNRs and require fewer amplitude mass points, making implementation simpler.

To summarize, the target of this work is to develop capacity-approaching distributions under peak amplitude constraint which can be utilized to efficiently design practical wireless optical systems.

4.2 Channel Capacity

Consider the channel model given in (3.1) as

$$Y = HX + Z. \tag{4.1}$$

The input X follows the constraints,

$$0 \leq X \leq A, \qquad \mathbb{E}\{X\} \leq P,$$

where A is the peak-amplitude limit. The signal-to-noise ratio for a given channel realization $H = h$ is given by,

$$\mathrm{SNR}(h) = \frac{P\,h}{\sigma},$$

and the optical peak-to-average power ratio (PAR) is defined as

$$\rho = \frac{A}{P}.$$

For eye-safety standards, $\rho < 17$ in typical commercial systems [113]. For channels with constrained input amplitude and power, it was first shown in [67] that the capacity-achieving input distributions are discrete with a finite number of mass points. Define the family of discrete input distributions

$$\mathcal{P} = \Bigg\{ p_X(x) : p_X(x) = \sum_{k=0}^{K} a_k\, \delta(x - x_k), x_k \in [0, A], \\ a_k \geq 0, \sum_{k=0}^{K} a_k = 1, K \in \mathbb{Z}^+, \sum_{k=0}^{K} x_k\, a_k \leq P \Bigg\},$$

where $\delta(\cdot)$ is the delta functional and $\mathbb{Z}^+$ is the set of positive integers. The number of mass points is $K + 1$, and a_k and x_k are the probability and location of the k^{th} mass point respectively. The channel capacity for a given channel state h is defined as,

$$\mathcal{C}(h) = \max_{f_X(x) \in \mathcal{P}} \mathbb{I}(X; Y | H = h), \tag{4.2}$$

where the mutual information, $\mathbb{I}(X;Y|H = h)$, is given by (3.2). The *capacity-achieving* input distribution is defined as

$$f_X^*(x) = \arg \max_{f_X(x)\in\mathcal{P}} \mathbb{I}(X;Y|H = h). \tag{4.3}$$

Finding an analytical closed form expression for the optimum distribution is difficult. However, for a given A, P, h, and σ^2, numerical optimization methods can be used to efficiently solve (4.2) to find $f_X^*(x)$ where the free parameters are a_k, x_k and K.

In [67, Proposition 1] it was shown that the mutual information is concave over the set of input distributions with bounded peak constraints. In addition, necessary and sufficient conditions on the optimal input distribution are given in [67, Corollary 1]. Furthermore, for a given peak amplitude, A, the number of mass points in $f_X^*(x)$ is monotonically non-decreasing with SNR and a mass point at $x_k = 0$ always exists [67]. Based on these facts, the capacity-achieving distribution is found by repeatedly solving the optimization problem in (4.2) for fixed $K = 1, 2, 3, 4, \ldots$ until a stopping criterion is met. Assume that the capacity-achieving distribution has $K^* + 1$ mass points. Solving the optimization problem with $K = K^* + m$, $m > 1$, results in the capacity-achieving distribution where the extra $m - 1$ mass points are assigned zero amplitudes. Note that the optimal input distribution must satisfy the conditions given in [67, Corollary 2]. Consequently, this fact is utilized as a stopping criterion for the optimization problem while incrementing K.

4.3 Capacity-Approaching Distributions

For every average optical power, peak amplitude and noise variance, the optimization problem (4.2) must be solved to extract $f_X^*(x)$. In addition to this drawback, the complexity of each run of the optimization problem increases as the number of mass points is increased. In this section, a simple family of capacity-approaching input distributions is developed based on source entropy maximization and termed *capacity-approaching* source distributions. These distributions have mutual information which closely approaches the channel capacity over a practical range of SNRs and are substantially simpler to generate than the capacity-achieving distribution. In addition, these capacity-approaching distributions are fixed over intervals of SNR making practical implementation easier.

4.3.1 Definition of Distributions

Consider the set of discrete input distributions $\mathcal{Q}_K \subset \mathcal{P}$ with $K+1$ *equally* spaced mass points,

$$\mathcal{Q}_K = \left\{ q_X(x) \in \mathcal{P} : \ell = \frac{A}{K},\ q_X(x) = \sum_{k=0}^{K} a_k \delta(x - k\ell) \right\} \tag{4.4}$$

where ℓ is defined as the mass point spacing. Define the maxentropic input distribution with $K+1$ mass points in $\mathcal{Q}_K$ as

$$\bar{q}_X(x; K) = \arg\max_{\mathcal{Q}_K} \mathbb{H}(X) \tag{4.5}$$

where

$$\mathbb{H}(X) = \sum_{k=0}^{K} a_k \log_2 \frac{1}{a_k}.$$

The input distribution that maximizes $\mathbb{H}(X)$ is considered based on the intuition that this distribution is capacity-approaching at high SNR. Define the collection of entropy maximizing discrete input distributions with different number of mass points as

$$\bar{\mathcal{Q}} = \left\{ \bar{q}_X(x) : \forall K \in \mathbb{Z}^+\ \bar{q}_X(x) = \bar{q}_X(x; K) \right\}$$

For a given A, P and σ^2, the capacity-approaching input distribution is the distribution in $\bar{\mathcal{Q}}$ which maximizes the mutual information, i.e.,

$$\bar{q}_X^*(x; \bar{K}(\rho, \mathrm{SNR})) = \arg \max_{f_X(x) \in \bar{\mathcal{Q}}} \mathbb{I}(X; Y | H = h), \tag{4.6}$$

where $\bar{K}(\rho, \mathrm{SNR}) + 1$ is defined as the number of mass points in the capacity-approaching distribution. Notice that while $\bar{q}_X(x; K) \in \bar{\mathcal{Q}}$ is independent of the channel parameters, i.e., noise variance, the distribution $\bar{q}^*_X(x; \bar{K}(\rho, \mathrm{SNR}))$ in (4.6) depends on the SNR value.

For each number of mass points $K + 1$, an expression for the maxentropic input distribution $\bar{q}_X(x; K)$ in (4.5) can be found by solving

$$\max_{a_k} \quad \mathbb{H}(X)$$
$$\text{s.t} \sum_{k=0}^{K} a_k = 1, \quad \sum_{k=0}^{K} k\ell a_k \leq P, \quad A = K\ell. \tag{4.7}$$

Define $\mathcal{J}$ as the Lagrangian associated with the optimization problem as

$$\mathcal{J} = \sum_{k=0}^{K} a_k \log_2 \frac{1}{a_k} - \lambda_1 \left(\sum_{k=0}^{K} a_k - 1 \right) - \lambda_2 \left(\sum_{k=0}^{K} k\ell a_k - P \right).$$

Proposition 4.1 *The discrete input distribution with equally spaced mass points that maximizes the entropy is given as,*

$$\bar{q}_X(x; K) = \sum_{k=0}^{K} \bar{a}_k \, \delta(x - k\ell) \tag{4.8}$$

where

$$\begin{aligned} \bar{a}_k &= \frac{1}{K+1}, & \rho \leq 2 \\ \bar{a}_k &= \frac{t_0^k}{1 + t_0 + t_0^2 + \ldots + t_0^K}, & \rho \geq 2 \end{aligned} \tag{4.9}$$

$t_0 \in [0, 1]$ *is the unique positive real root of*

$$S(t) = \sum_{k=0}^{K} \left(1 - \frac{k}{K} \rho \right) t^k. \tag{4.10}$$

Proof. Notice that when $\rho < 2$, i.e., $A < 2P$, a uniform distribution over the a_k satisfies both average and peak amplitude constraints. Since the uniform distribution is entropy maximizing among all discrete distributions, it must also be the result of the optimization problem. In this case there is slack in the average amplitude constraint, i.e., $\sum_{k=0}^{K} k\ell a_k < P$ and hence $\lambda_2 = 0$.

When $\rho \geq 2$ the above optimization problem is solved analytically considering all constraints. Solving the equations $\partial \mathcal{J}/\partial a_k = 0$ and substituting the constraints given in (4.7) it is straightforward to obtain (4.9). Notice that $\bar{a}_k > 0$ in (4.9) and for a given t_0 the polynomial $1 + t_0 + t_0^2 + \ldots + t_0^K$ has a fixed sign. Thus, $t_0 > 0$ since otherwise the sign of $\bar{a}_k$ would alternate. Lemma F.1 in the Appendix demonstrates that $S(t)$ has a unique positive root in $[0, 1]$. For a given K, equation (4.10) can be solved efficiently to obtain the real root t_0. As shown in Appendix F, $t_0 = 1$ when $\rho = 2$ and both expressions for the mass point amplitude a_k coincide. ■

A key point is that $\bar{q}_X(x) \in \bar{\mathcal{Q}}$ depends only on the amplitude constraints ρ while $\bar{q}_X^*$ in (4.6) depends on both ρ and SNR.

4.3.2 Estimate of $\bar{K}(\rho, \mathrm{SNR})$

An analytic expression for $\bar{K}(\rho, \mathrm{SNR})$, that maximizes the mutual information is difficult to obtain since it varies with SNR and ρ and since the mutual information expression depends on a nested relation between t_0 and K. Here we provide a simple approximation for $\bar{K}$ based on numerical analysis.

For a given ρ and SNR, $\bar{q}_X^*(x; \bar{K}(\rho, \mathrm{SNR}))$ has the highest mutual information over all source distributions in $\bar{\mathcal{Q}}$. Consider increasing SNR for a fixed ρ. There exists an $\mathrm{SNR_o} > \mathrm{SNR}$ at which the mutual information using $\bar{q}_X^*(x; \bar{K}(\rho, \mathrm{SNR_o}))$, is greater than or equal to that obtained using $\bar{q}_X^*(x; \bar{K}(\rho, \mathrm{SNR}))$. In this case, $\bar{K}(\rho, \mathrm{SNR_o}) = \bar{K}(\rho, \mathrm{SNR}) + 1$. We term $\mathrm{SNR_o}$ as a *transition SNR* where the number of mass points in the capacity-approaching distribution is incremented.

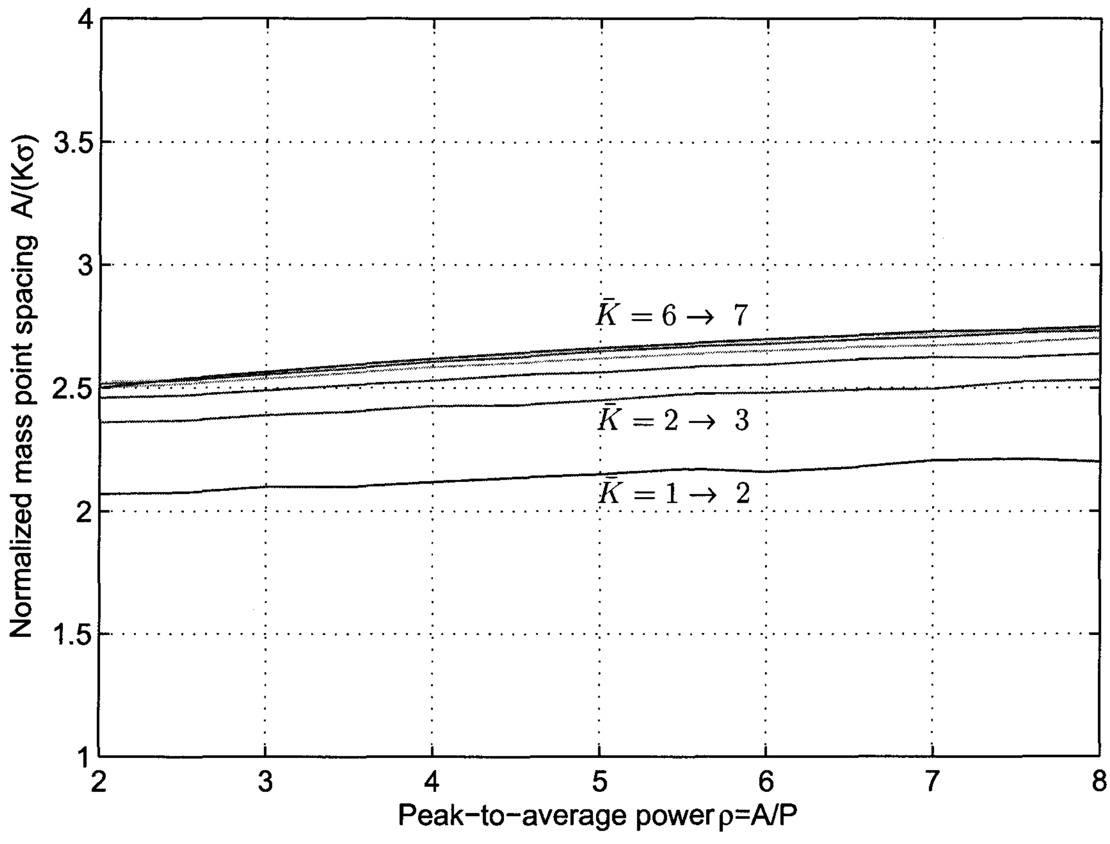

Figure 4.1: Normalized spacing ℓ/σ versus ρ at transition SNRs between $\bar{K}+1 \rightarrow \bar{K}+2$ mass points in $\bar{q}_X^*(x;\bar{K})$.

In order to remove the impact of scaling, define the normalized mass point spacing

$$\frac{\ell}{\sigma} = \frac{A}{\bar{K}\sigma} = \rho \cdot \mathrm{SNR} \cdot \frac{1}{\bar{K}(\rho, \mathrm{SNR})}.$$

The normalized mass point spacing is shown in Fig. 4.1 versus ρ at the transition SNRs as $\bar{K}$ increases from 1 to 7. From the figure, it is clear that ℓ/σ for a given transition between numbers of mass points changes slowly with ρ. A simple approximation adopted here is to set $\ell/\sigma = c$, for some constant c. This constant can be chosen from Fig. 4.1 depending on the SNR range of interest. For example, for high SNR cases where $\bar{K}$ is large, a reasonable value for $c \approx 2.7$, whereas, for low SNR cases $c \approx 2.2$. For the purposes of our numerical work we set $c = 2.5$ to yield the simple approximation for $\bar{K}$

$$\hat{K} = \left\lfloor \frac{A}{2.5\,\sigma} \right\rfloor. \tag{4.11}$$

Although many selections of $\hat{K}$ yield acceptable performance, the resulting mutual information using this approximation remains close to the channel capacity as shown in Section 4.3.3.

4.3.2.1 Interpretation of the Estimate $\hat{K}$

As discussed in Section 4.3.2, an estimate for K over a wide range of peak-to-average power ratio ρ is given by $\hat{K}$ in (4.11). This relation can be written as follow,

$$K \approx \frac{A}{c_3\,\sigma},$$

where c_3 is a constant in the range from 2.1 to 2.7 when ρ varies from 2 to 8 as shown in Fig. 4.1. This relation can be rearranged as,

$$\frac{A}{K\,\sigma} = \frac{\ell}{\sigma} \approx c_3,$$

i.e., the normalized mass point spacing to the noise standard deviation is approximately constant. This approximation for the case of peak and average optical power constraints coincides with the result obtained in Chapter 3 for $\tilde{\beta} = \sigma/h\ell$ in (3.24) in the case when only an average power constraint is considered where

$$\tilde{\beta} = \frac{\sigma}{\ell} = \frac{1}{c_1}\left(\frac{Ph}{\sigma}\right)^{-c_2-1} = \frac{1}{3.08}\left(\frac{Ph}{\sigma}\right)^{0.06}.$$

Notice that $\tilde{\beta}$ is approximately constant over a small range of SNR, i.e., the mass point spacing ℓ is approximately linearly proportional to the noise standard deviation σ. Clearly, this behavior can be induced for the two cases, 1) average power constraint and 2) average and peak power constraint.

4.3.3 Channel Capacity and Information Rates

The channel capacity is computed by numerically solving the optimization problem. The MATLAB® function `fmincon` [111, version 7.6] from the optimization toolbox is utilized. The tolerance between successive iterations in the objective function (mutual information) solution is set to 10^{-10}. The routine stops if the difference in mutual information in two successive iterations is less than the tolerance. The optimal input distribution obtained from the optimization problem also satisfies the conditions [67, Corollary 2]. Note that, with the concavity of the mutual information over $\mathcal{P}$, a global maximum is guaranteed.

The mutual information of the proposed maxentropic input distributions (4.8) versus SNR for $\rho = 2$ and $K = 1$, 2 and 3 are shown in Fig. 4.2. Recall that when $\rho = 2$ the maxentropic input distribution is uniform with $K + 1$ probability mass points (*Proposition 4.1*). Clearly, a small gap can be noticed between the mutual information and the channel capacity for different SNRs. In addition, based on the numerical results obtained from solving the optimization problem, the input distribution $f_X^*(x) = 0.5\,\delta(x) + 0.5\,\delta(x - A)$ is capacity-achieving input distribution at low SNRs which is also the maxentropic distribution obtained in (4.8).

Although the uniform distribution is a capacity-approaching distribution when

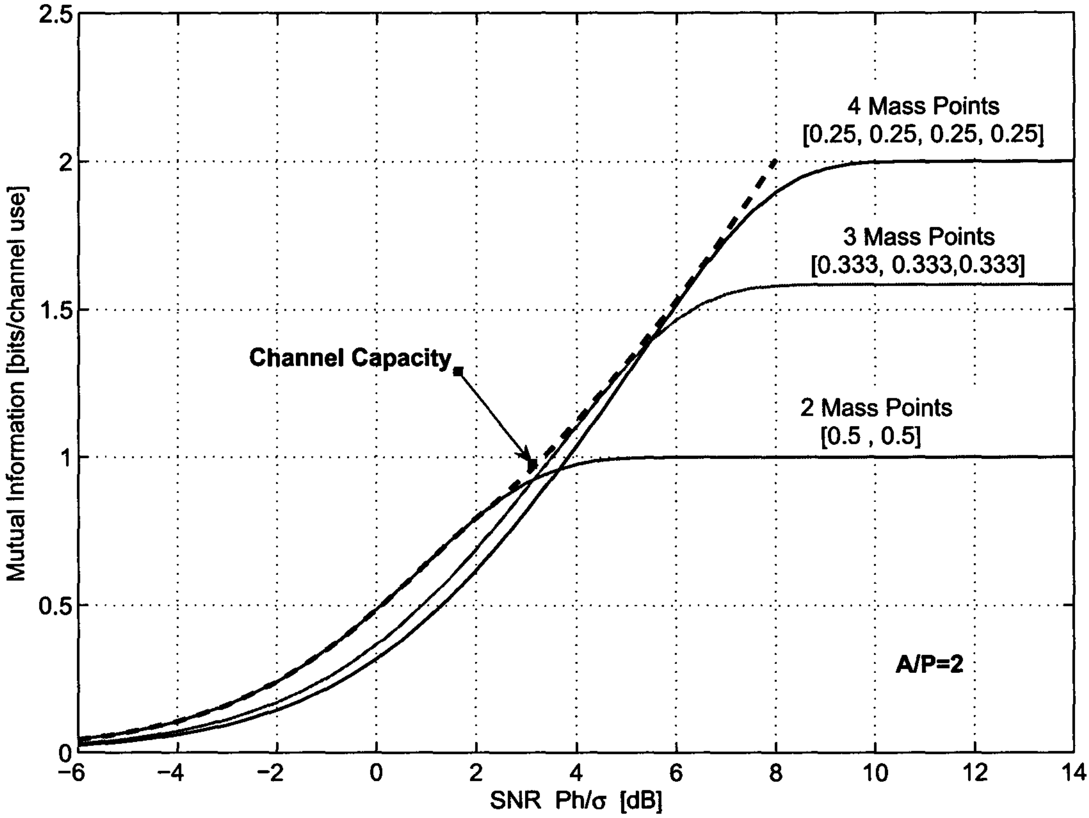

Figure 4.2: Peak and average power constraints. Channel capacity and mutual information for the maxentropic input distributions (4.8) with different number of mass points versus SNR for $\rho = 2$.

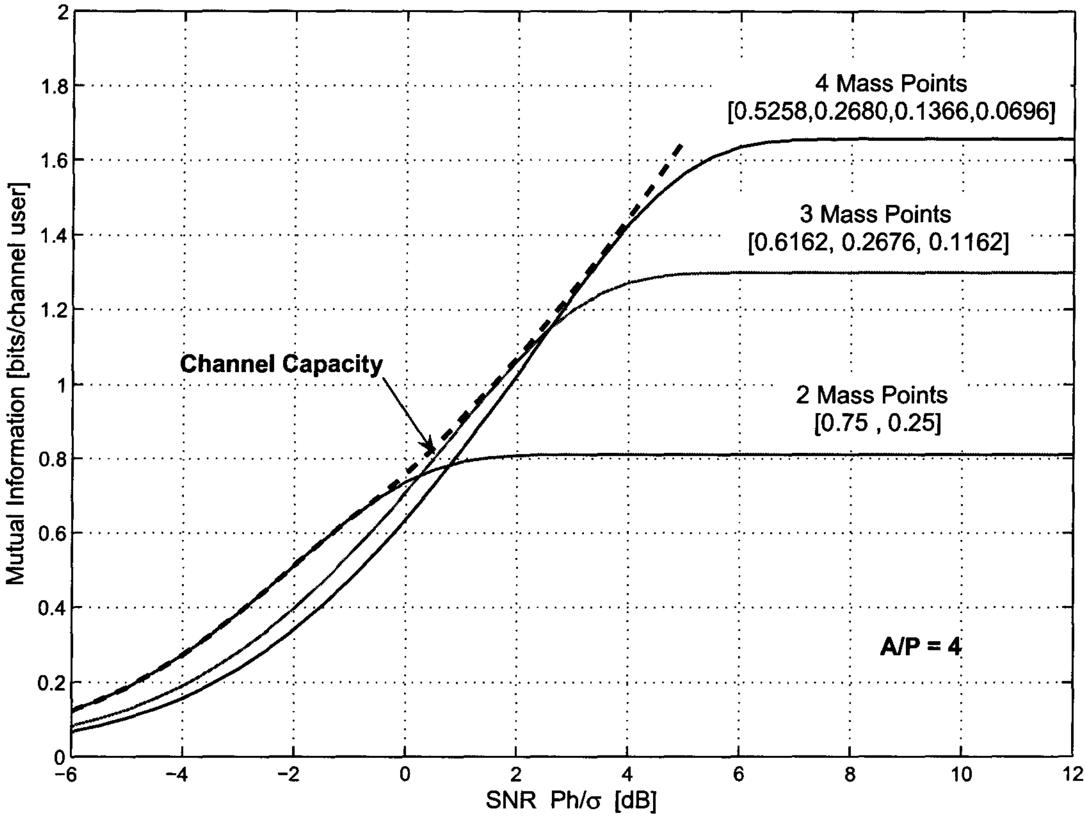

Figure 4.3: Peak and average power constraints. Channel capacity and mutual information for the maxentropic input distributions (4.8) with different number of mass points versus SNR for $\rho = 4$.

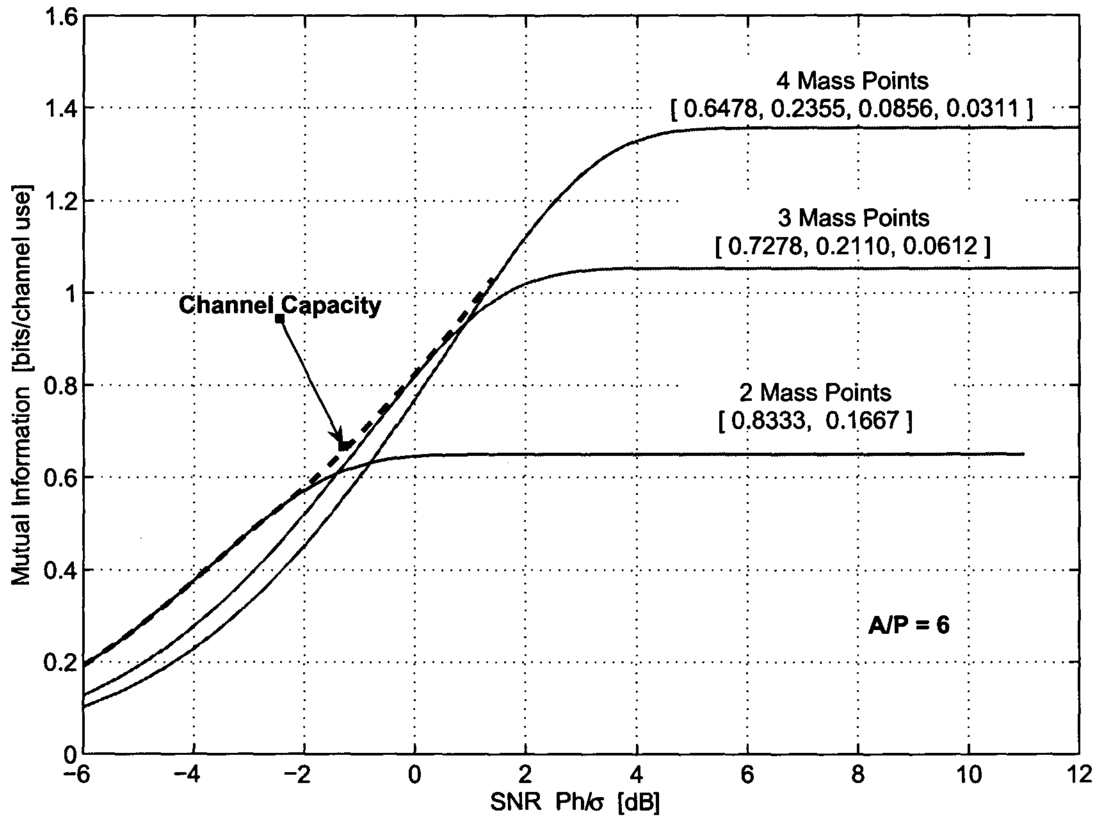

Figure 4.4: Peak and average power constraints. Channel capacity and mutual information for the maxentropic input distributions (4.8) with different number of mass points versus SNR for $\rho = 6$.

$\rho = 2$, the situation is quite different when $\rho > 2$. As shown in Fig. 4.3 when $\rho = 4$ the capacity-approaching distributions are non-uniform. The maxentropic input distributions approach the channel capacity over a wide range of SNRs. Furthermore, the input distribution is fixed over a range of SNRs. As an example, the maxentropic input distribution with three mass points is utilized when the SNR varies from 0.25 to 2.5 dB. Note that although the input distribution is fixed in this range, for each SNR, i.e., each rate, different encoders and decoders are utilized to achieve the corresponding rate. At low SNRs the maxentropic distribution is a capacity-approaching distribution with $\bar{q}_X^*(x, 1) = 0.75\,\delta(x) + 0.25\,\delta(x - A)$ where more weight is assigned to the mass point located at zero. Fig. 4.4 presents the mutual information and the channel capacity when $\rho = 6$. As shown, as ρ increases the maxentropic input distributions become more non-uniform with increasing mass point probability at zero amplitude.

From the previous discussion, at low SNRs, an input distribution with two mass points (i.e., $K = 1$) is sufficient to achieve/approach the channel capacity. The probability mass for these two-level outputs can be found from (4.8) and are given by

$$[p_0, p_1] = \left[\frac{\rho - 1}{\rho}, \frac{1}{\rho}\right].$$

Notice that as ρ increases the resulting capacity-approaching distributions become increasingly non-uniform with most weight on the zero-amplitude.

The capacity of the wireless optical intensity channel versus SNR (4.2) is shown in Fig. 4.5 for $\rho = 4$. In addition, the mutual information with input distribution $\bar{q}_X^*(x; \bar{K})$ in (4.6) is presented. Clearly, the proposed input distributions achieve nearly most of the rates offered by the optical channel with a substantial reduction in complexity. Figure 4.5 also plots the mutual information using the maxentropic source distribution (4.8) when the number of mass points is approximated by $\hat{K} + 1$ given in (4.11). Notice that the mutual information is also close to the capacity over the SNR

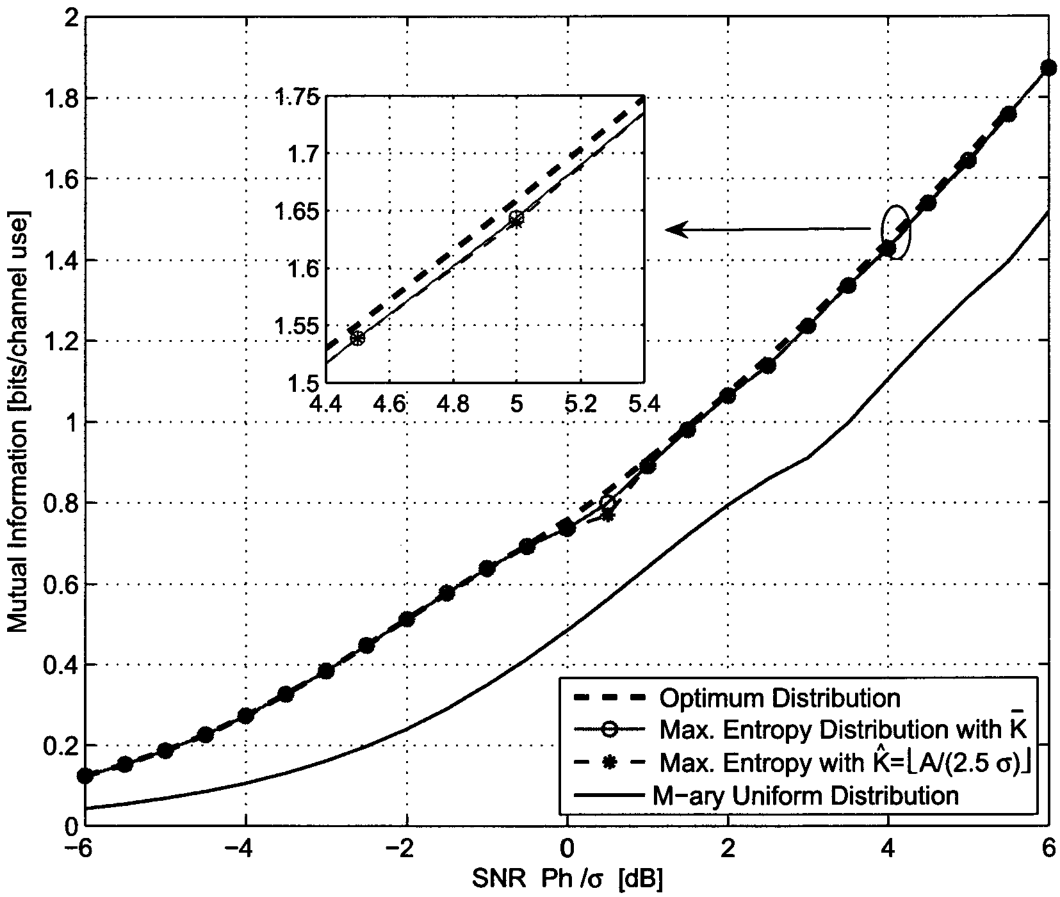

Figure 4.5: Peak and average power constraints. Channel capacity and mutual information for the proposed input distribution with K and $\hat{K}$ and the uniform input distributions for $\rho = 4$.

range considered, and only differs negligibly from the case where a search is performed to find a good $\bar{K}$ value. Thus, the approximation (4.11) does not incur a significant penalty in terms of rate. Notice that at SNR $= 0.5$ dB the mutual information using the maxentropic input distribution with $\hat{K}+1$ mass points is smaller than that with $\bar{K}+1$ mass points. This occurs since at this SNR the proposed $\hat{K}$ expression (4.11) under estimate the number of mass point. More precisely, when SNR $= 0.5$ the expression (4.11) results in $\hat{K}=1$, however, the maxentropic input distribution with three mass points achieves higher mutual information compared to the maxentropic input distribution with two mass points as shown in Fig. 4.3 when $\rho = 4$.

For comparison, the mutual information using uniform input distributions satisfying both the average and the peak power constraints is also presented. The uniform distributions utilized are selected from the set $\mathcal{U}$ defined for $\rho \geq 2$ as

$$\mathcal{U} = \left\{ q_X(x) : \forall K > 0,\ d = \frac{2P}{K}, q_X(x) = \sum_{k=0}^{K} \frac{1}{K+1}\,\delta(x - kd) \right\}. \tag{4.12}$$

Notice that these distributions have mass points with equal probability that are equally spaced. At each SNR, the distribution in $\mathcal{U}$ which maximizes the mutual information is selected and the information rate is plotted. As shown in Fig. 4.5, a remarkable gap between the mutual information of the uniform distribution and the non-uniform distribution is noticed. Therefore, the use of non-uniform signalling is essential for optical intensity channels, especially as ρ increases.

4.3.4 Input Distributions and Numbers of Mass Points

The number of mass points in the capacity-achieving source distribution (4.2), K^*+1, the capacity-approaching maxentropic distribution (4.6), $\bar{K}+1$, the maxentropic distribution with approximated K (4.11), $\hat{K}+1$, and the uniform distribution, $K_{\mathrm{u}}+1$, are presented in Table 4.1 for different SNR values.

Table 4.1: Number of mass points in the input distribution that maximizes the mutual information when $\rho = 4$

SNR [dB]		-1	0	1	2	3	4	5
Capacity-Achieving (4.2)	$K^* + 1$	2	3	3	4	4	5	7
Max. Entropy (4.6)	$\bar{K} + 1$	2	2	3	3	4	4	5
Max. Entropy approx (4.11)	$\hat{K} + 1$	2	2	3	3	4	5	6
Uniform	$K_{\text{u}} + 1$	2	2	2	2	2	3	3

Note that, although K^* is fixed over a range of SNR, the input distribution, i.e., mass points amplitudes and locations, varies for each SNR value. Unlike the capacity-achieving input distribution, for a given $\bar{K}$ the maxentropic distribution is fixed. Therefore, and as shown in Table 4.1, the maxentropic distribution that maximizes the mutual information is fixed over a range of SNRs. This advantage, in addition to the negligible gap between the mutual information and the channel capacity and the substantial complexity reduction in generating this distribution, renders the maxentropic input distribution more practical for realization over the capacity-achieving distribution obtained via optimization. Also notice that the uniform distribution has the minimum number of mass points as SNR increases simplifying its implementation, however, there is a severe rate degradation as shown in Fig. 4.5.

The capacity-achieving and the maxentropic input distributions are shown in Fig. 4.6 for SNRs=$[-3, 0, 3, 5]$ dB at $\rho = 4$. Notice that the mass point spacing is a free parameter in the capacity-achieving distributions while it is fixed in the maxentropic distributions. When SNR=-3 dB, an input distribution with two mass points can achieve the channel capacity and both the capacity-achieving and the maxentropic distributions coincide. As the SNR increases to 0 dB and although the

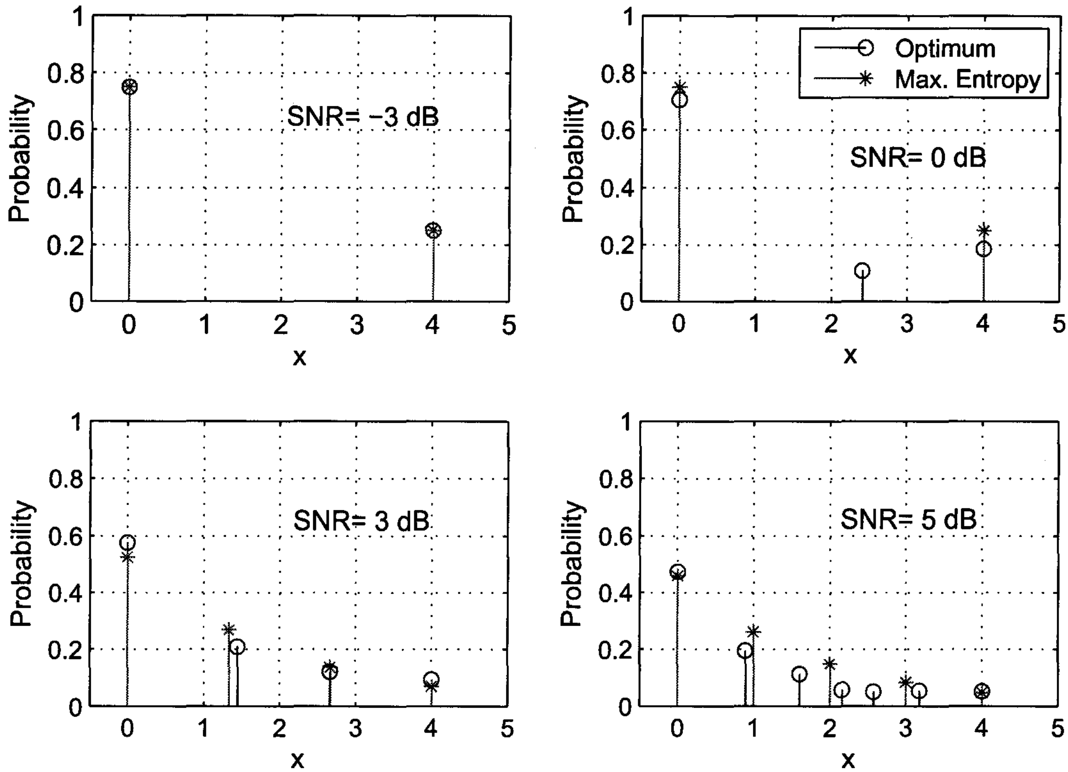

Figure 4.6: The optimum, $f_X^*(x)$ (4.3), and the proposed input distributions, $\bar{q}_X^*(x, \bar{K})$ (4.6), for different SNRs at $\rho = 4$.

number of mass points is different, the maxentropic distribution is still capable of approaching the channel capacity with a small gap. When SNR increases further to 5 dB, this observation becomes more clear where five and seven mass points are shown for the maxentropic and the capacity-achieving input distributions respectively. Surprisingly, the resulting information rates for both distributions are still very close as shown in Fig. 4.5.

4.4 Mutual Information Behavior for Different ρ

In this section the behavior of the mutual information versus SNR for different ρ, the peak-to-average optical power ratio, is investigated. Note that as ρ increases, higher mutual information can be achieved since more degrees of freedom are available.

Figure 4.7 presents the mutual information, in bits/channel use, versus SNR for $\rho = 2$, 4, and 8 using the input distribution $\bar{q}_X^*(x; \bar{K})$ in (4.6). Also the mutual information for the limiting case when $\rho \to \infty$ is shown representing the case when only an average optical power constraint is considered, i.e., the capacity lower bound C_{L} (3.7). Notice that, at high SNR the mutual information when $\rho \geq 4$ is close to C_{L}, i.e., the effect of the peak power constraint is weak. In addition, when $\rho = 2$, i.e., uniform input distribution (4.8), the resulting mutual information is greatly smaller than the rates achieved when $\rho \geq 4$ even at high SNRs.

However, at low SNR a larger gap is noticed as shown in Fig. 4.7 for different ρ, meaning that the peak power constraint has a strong impact on the achievable mutual information. Since, in general, at low SNR the input distribution, $\bar{q}_X^*(x, \bar{K})$, has a small number of mass points, then giving more degrees of freedom in choosing the spacing between the mass points, i.e., peak amplitude, can increase the mutual information achieved.

It should be noted that in Fig. 4.7 the breakpoint in the mutual information curve when $\rho = 2$ at approximately SNR = 3 dB is due to the transition from using the maxentropic input distribution with two mass points to the maxentropic input distribution with three mass points. This transition can be directly deduced from Fig. 4.2. The same observation can be seen when $\rho = 4$ and 8 at different SNR values, e.g. when $\rho = 4$ at SNR = 0 dB.

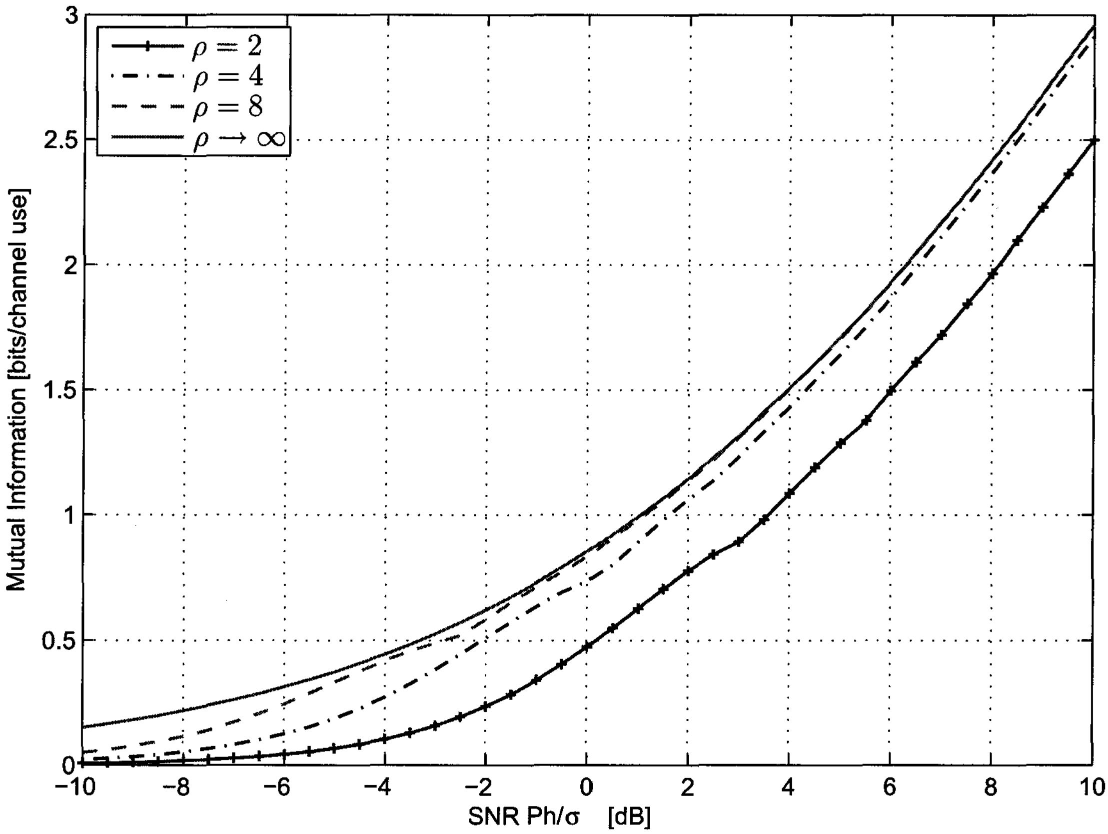

Figure 4.7: Peak and average power constraints. Mutual information versus SNR for different ρ using the input distribution $\bar{q}_X^*(x; \bar{K})$ in (4.6).

4.5 Conclusion

The capacity of optical intensity channels with peak and average optical power constraints is analyzed. The capacity-achieving input distribution is found through numerical solution for a non-linear optimization problem. A closed form for a capacity-approaching distribution based on entropy maximization is presented. In addition to the substantial complexity reduction in generating this distribution as compared to the optimum distribution, a negligible gap between the resulting mutual information and the channel capacity is noticed. Unlike the capacity-achieving distribution where for each SNR a different input distribution is obtained, the maxentropic input distribution that maximizes the mutual information is fixed over a range of SNRs. For given peak amplitude, average optical power and noise variance, an approximate closed form expression is provided for the number of mass points. Over a practical range of SNR, the number of probability mass points in the maxentropic distribution is less than that in the capacity-achieving distribution, reducing implementation complexity. The derived capacity-approaching distributions serve as a useful tool not only to bound the channel capacity but to guide the development of channel coding and modulation schemes for such optical wireless channels.

As discussed, non-uniform discrete input distributions are shown to be essential for optical intensity channels. In the following chapter, a practical algorithm for communication with non-uniform distributions is presented. Multilevel coding and a deterministic mapper are utilized to induce non-uniform distributions at the channel input and multistage decoding is employed at the receiver. Performance evaluations compared to uniform input distributions are also presented.

Chapter 5

Coding for Optical Channels: Non-Uniform Distributions

In this chapter an algorithm to realize non-equally likely symbols is presented. The non-uniform distribution is considered due to the significant gain in rates achieved compared to uniform distribution as shown in Chapters 3 and 4. The distribution is induced using a deterministic mapper at the transmitter. Given equally likely input bits, each N-tuple bits are mapped to a symbol in the input alphabet set. Each individual bit within the N-tuple is protected through an error correcting code where N encoders are utilized. The encoders are arranged in a multi-level coding (MLC) structure. The received codeword is decoded sequentially using multi-stage decoding (MSD). The algorithm presented in [88] using MLC/MSD is considered.

The novelty of the work presented in this chapter is the application of [88] to induce non-uniform distributions for wireless optical channels. However, modified input distributions with quantized mass point probabilities are developed to simplify the implementation. Furthermore, numerical simulations are conducted showing that non-uniform distributions and practical codes outperform uniform distributions with capacity-achieving codes.

5.1 Introduction

A majority of communication channels consider uniform input distribution since it is shown to be a capacity-achieving distribution. Even for some classes of channels when the capacity-achieving input distribution is not uniform (e.g. Z-channel [84]) the mutual information using a uniform distribution is shown to be close to the channel capacity. Coding for channels with uniform input distributions has been addressed in the literature for decades where binary linear codes are utilized. The use of binary linear codes was motivated by the fact that most data sources are modeled as uniformly distributed.

However, the situation is different for the optical channels, where the capacity-achieving input distribution is discrete and non-uniform [67,69–74,114–116] as shown in Chapters 3 and 4. Furthermore and unlike the RF channels, in wireless optical channels a remarkable gap between the channel capacity, i.e., using non-uniform distribution, and the mutual information of the uniform distributions exists.

Inducing a non-uniform input distribution is not straightforward compared to the uniform distribution which is induced directly using linear codes. Coding for channels with non-uniform input distributions was first presented by Gallager [83]. Gallager used a deterministic mapper at the output of a binary encoder where each N-bits are mapped to a symbol from the input channel alphabet such that the output symbols have a non-uniform distribution. However, Gallager wrote
"*Unfortunately, the problem of finding decoding algorithms is not so simple*" [83].

McEliece [84] suggested using a linear encoder and considered an iterative mesage-passing algorithm with the "*hope*" [84] that this structure solves the decoding problem mentioned by Gallager. Analysis and design examples were not given in [84] to strengthen the suggestion. Later MacKay *et al* [85] investigated the performance of binary low density parity-check (LDPC) codes with a mapper as suggested in [84].

Simulations showed that this method did not generally perform well. Another approach for inducing a non-uniform distribution is presented in [85] where LDPC codes are designed over GF(q) with $q > 2$. As an example, when $q = 3$ the LDPC symbols are $\{0, 1, 2\}$ and in order to induce channel input with probability of one, i.e., $p(1)$, equal to 1/3 the following mapping is considered $\{0, 1, 2\} \rightarrow \{010, 100, 001\}$. Although a substantial performance improvement was reported, the higher complexity in both code design and decoding process limits the employment of such techniques. An alternative approach is presented in [117] where an inverse Huffman code type mapper is proposed to induce the non-uniform distribution. However, mapping each input symbol to a different number of bits may cause catastrophic decoding errors. In addition to this drawback, the complexity of soft decoding limits the utilization of this scheme. A method to realize the channel capacity when the source distribution is non-uniform is to employ a multi-level coding (MLC) structure followed by a deterministic mapper at the transmitter and at the receiver a multi-stage decoding (MSD) is considered [88]. Even when the mapping is not a one-to-one function, this structure achieves the channel information rate [88].

In this chapter, the MLC/MSD technique in [88] is utilized, however, only mass point probabilities with multiples of $1/2^N$ can be realized. Therefore, the non-uniform distributions developed in Chapters 3 and 4 are modified such that the mass point probabilities are quantized to one of $1/2^N$ levels. Thus, the term "*quantized-level distribution*" is utilized. The smaller the number of encoders, N, the lower the system complexity, however, the higher the performance degradation. We demonstrate that utilizing two or three encoders/decoders results in a substantial reduction in complexity with rate that is significantly close to the channel capacity. Design examples to approach the promising rates using finite length low density parity check (LDPC) codes are presented.

$$\text{bit stream} \longrightarrow \underbrace{[W_1,\ldots,W_N]}_{\boldsymbol{W}} \longrightarrow \boxed{\text{Mapper } \mathcal{M}} \longrightarrow X \longrightarrow \boxed{\begin{array}{c}\text{Gaussian}\\ \text{Channel}\end{array}} \longrightarrow Y$$

Figure 5.1: Illustrative diagram for optical channels including mapper

5.2 Generating Non-uniform Distribution

In this chapter the method presented in [88] is applied to realize non-uniform distributions. The algorithm can be divided into two parts: mapping and encoding/decoding algorithm. The mapper is discussed here while the coding algorithm is discussed in Section 5.3. A simple illustrative diagram for the system is shown in Fig. 5.1. In this system each group of N-bits from the independent equally likely input bits in the stream $\boldsymbol{W} = [W_1, \ldots, W_N]$ are mapped to a constellation symbol X from the channel input alphabets $\mathcal{X}$ through the mapping function $\mathcal{M}$ such that these symbols have non-uniform probabilities. Notice that in this technique the realized probability takes the form $m/2^N$ where $m = 1, \ldots, 2^N - 1$ is an integer. Clearly, for a given N there exists a set of non-uniform distributions that can be induced at the channel input. Note that the mapping $\boldsymbol{W} \xrightarrow{\mathcal{M}} X$ is not necessarily a one-to-one mapping. However, in spite of this fact, the mutual information, $\mathbb{I}(X;Y)$, between channel input and output is unaffected as presented in the following Lemma.

Lemma 5.1 *Given a Markov chain $\boldsymbol{W} \to X \to Y$ and a deterministic mapper $\mathcal{M}(\boldsymbol{W}) = X$, then*

$$\mathbb{I}(X;Y) = \mathbb{I}(\boldsymbol{W};Y).$$

Proof.(see [88])

Consider the following mutual information expansion,

$$\begin{aligned}\mathbb{I}(\boldsymbol{W};X,Y) &= \mathbb{I}(\boldsymbol{W};X) + \mathbb{I}(\boldsymbol{W};Y|X),\\ &= \mathbb{I}(\boldsymbol{W};Y) + \mathbb{I}(\boldsymbol{W};X|Y).\end{aligned}$$

Applying the Markov chain properties,

$$\mathbb{I}(\boldsymbol{W};Y|X) = 0.$$

Also note that, since X is a deterministic function of $\boldsymbol{W}$ then

$$\mathbb{H}(X|\boldsymbol{W}) = 0, \quad \text{and} \quad \mathbb{H}(X|\boldsymbol{W},Y) = 0,$$

where $\mathbb{H}(\cdot)$ is the entropy. Hence $\mathbb{I}(\boldsymbol{W};Y)$ is given by,

$$\begin{aligned}\mathbb{I}(\boldsymbol{W};Y) &= \mathbb{I}(\boldsymbol{W};X) - \mathbb{I}(\boldsymbol{W};X|Y),\\ &= [\mathbb{H}(X) - \mathbb{H}(X|\boldsymbol{W})] - [\mathbb{H}(X|Y) - \mathbb{H}(X|\boldsymbol{W},Y)],\\ &= \mathbb{H}(X) - \mathbb{H}(X|Y),\\ &= \mathbb{I}(X;Y).\end{aligned}$$

■

This result indicates that, given a deterministic mapping function, $\mathcal{M}$, the information rate can be realized and achieved even when the mapping is not one-to-one, i.e., non-reversible.

5.3 Coding Scheme for Optical Channel

Consider the combination of MLC with a deterministic mapper which is used to ensure that the appropriate non-uniform distribution is induced at the channel input. Figure 5.2 shows a block diagram for the MLC system including the mapper [86,87]. Assume a stream of independent equally likely input bits. Consider k-bits from the stream that are divided to N sub-streams each with k_i bits where $i = 1, \ldots, N$ such that $k = \sum_{i=1}^{N} k_i$. The i^{th} sub-stream is protected by a linear binary code of rate R_i. For convenience, the output codeword length of each encoder is fixed to $n = k_i/R_i$. The output of the encoders are the bits $\boldsymbol{W} = [W_1, \ldots, W_N]$, where W_i denotes the i^{th} encoder output bit. The vector $\boldsymbol{W}$ is mapped to a constellation point in the input alphabet using a deterministic mapper $\mathcal{M}$. Applying the chain rule, the mutual information can be expressed in terms of the sub-channel rates as follows,

$$\mathbb{I}(\boldsymbol{W}; Y) = \sum_{i=1}^{N} \mathbb{I}(W_i; Y | W_1, \ldots, W_{i-1}),$$

where the sub-channel rates are given by

$$R_i = \mathbb{I}(W_i; Y | W_1, \ldots, W_{i-1}).$$

The received codeword is decoded sequentially to extract the transmitted data bits. Figure 5.3 shows a block diagram for the multi-stage decoding MSD technique illustrating the sequential decoding strategy of the MSD. The first decoder utilizes the received signal, Y, to obtain the estimate $\hat{W}_1$. Given that the codeword is decoded correctly, i.e., $\hat{W}_1 = W_1$, the second decoder utilizes both Y and $\hat{W}_1$ to get the estimate $\hat{W}_2$ since the second encoder operates at $R_2 = \mathbb{I}(W_2; Y | W_1)$. This process is repeated sequentially till $\hat{W}_N$ is estimated. Note that if a codeword is decoded incorrectly an error event occurs and propagates resulting in decoding error in the estimated transmitted data. Considering the sequential technique used in MSD, an increase in the decoding time, i.e., latency, is expected compared to binary codes.

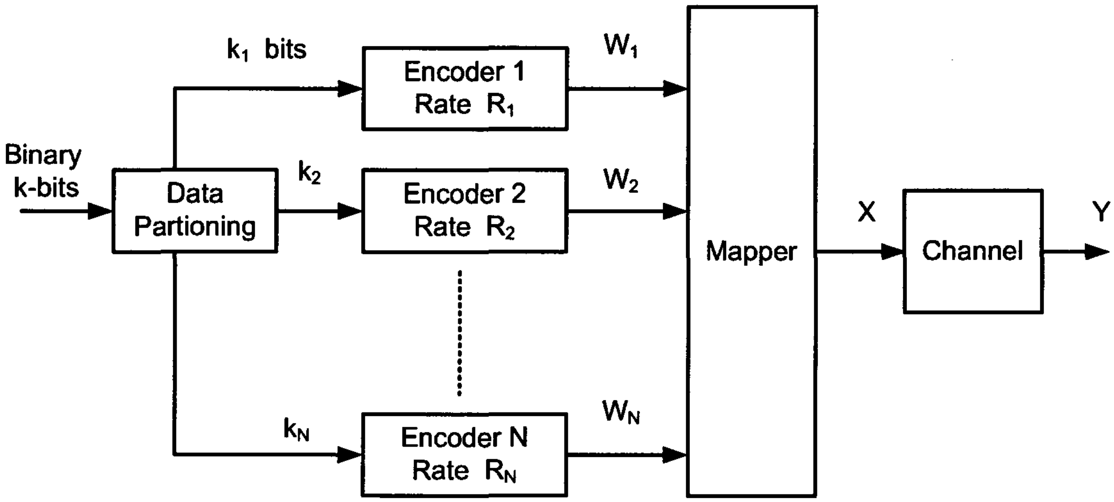

Figure 5.2: Schematic block diagram for multilevel coding (MLC) and mapping scheme for optical intensity channels with non-uniform channel input distribution.

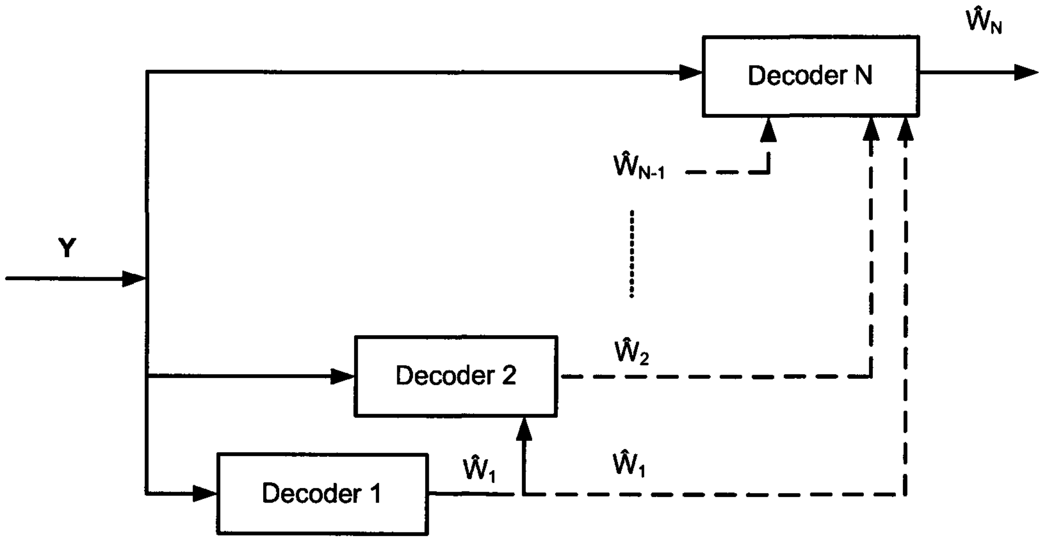

Figure 5.3: Schematic block diagram for multi-stage decoders (MSD).

5.4 The Mapper and the Equivalent Channel

Consider the individual sub-channels in the MLC structure. In order to design the i^{th} sub-channel rate $R_i = \mathbb{I}(W_i; Y|W_1, \ldots, W_{i-1})$ it is required to accurately model the channel between W_i and Y. This channel is a cascade of two channels, a virtual channel between W_i and X representing the mapper followed by a physical channel, i.e., Gaussian channel as shown in Fig. 5.1. The mapper equivalent channel is different for each bit W_i.

To illustrate how the channel is modeled, consider two mass points where the input alphabet is $\mathcal{X} = \{0, 1\}$ with probabilities $p(0) = 7/8$ and $p(1) = 1/8$. This system can be constructed using $N = 3$ encoders where the deterministic mapping function $\mathcal{M}$ is given by

$$\boldsymbol{W} = [W_1, W_2, W_3] \overset{\mathcal{M}}{\longmapsto} X : X = \begin{cases} 1 & \text{if } W_1 = W_2 = W_3 = 1, \\ 0 & \text{otherwise.} \end{cases} \tag{5.1}$$

An expanded and detailed diagram for the mapping function is presented in Fig. 5.4 as an illustrative tool to be used to model the channel between W_i and X. To design the rate $R_1 = \mathbb{I}(W_1; Y)$, consider the following channel between W_1 and X. The bit $W_1 = 0$, i.e., most significant bit in Fig. 5.4, is mapped to $X = 0$ in all cases while $W_1 = 1$ is mapped to $X = 0$ exactly 3/4 times. Therefore, the equivalent channel between W_1 and X is a Z-channel with cross-over probabilities as shown in Fig. 5.5. Hence the equivalent channel between the input bit W_1 and the output Y is a Z-channel followed by a Gaussian channel as shown in Fig. 5.6

In general, and based on the mapping function $\mathcal{M}$, the equivalent channel between W_i and X is a binary asymmetric channel as shown in Fig. 5.7. Notice that, this channel, i.e., cross-over probabilities (p_{W_i}, q_{W_i}), is different for each input bit W_i. The equivalent channel for W_2 is determined based on W_1. If $W_1 = 1$, the equivalent channel for W_2 is also a Z-channel with $q_{W_2} = 0$ and $p_{W_2} = 1/2$. If $W_1 = 0$, the

$$
\left.\begin{array}{ccc}
W_1 & W_2 & W_3 \\
\mathbf{0} & 0 & 0 \\
\mathbf{0} & 0 & 1 \\
\mathbf{0} & 1 & 0 \\
\mathbf{0} & 1 & 1 \\
\mathbf{1} & 0 & 0 \\
\mathbf{1} & 0 & 1 \\
\mathbf{1} & 1 & 0
\end{array}\right\} \xrightarrow{\mathcal{M}} X = 0 \qquad p(0) = 7/8
$$

$$
\left.\begin{array}{ccc}
\mathbf{1} & 1 & 1
\end{array}\right\} \xrightarrow{\mathcal{M}} X = 1 \qquad p(1) = 1/8
$$

Figure 5.4: Mapping function over $\mathcal{X} = \{0, 1\}$ to induce $p(0) = 7/8$

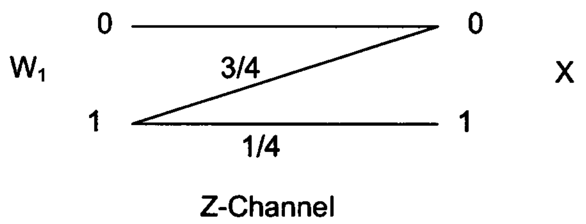

Figure 5.5: Equivalent Z-Channel seen by W_1 when $N = 3$ and $p(0) = 7/8$

$$
W_1 \longrightarrow \boxed{\text{Z-Channel}} \longrightarrow X \longrightarrow \boxed{\text{Gaussian channel}} \longrightarrow Y
$$

Figure 5.6: Equivalent Channel between W_1 and Y

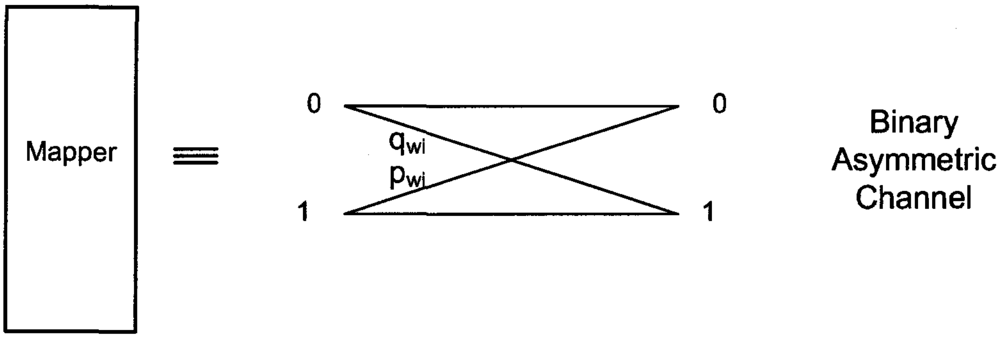

Figure 5.7: Equivalent channel for the mapper as seen by the individual bit W_i.

equivalent channel for W_2 is a binary asymmetric channel (BAC) with $q_{W_2} = 0$ and $p_{W_2} = 1$. Hence, the equivalent channel for the proposed system is composed of two cascaded channels, asymmetric channel followed by a Gaussian noise channel. Although code design should consider this detail, it was shown that LDPC codes optimized for Gaussian channels also perform well over many asymmetric channels [118]. For the MLC/MSD system considered, each sub-channel encoder is realized using an "off-the-shelf" LDPC code that was originally designed for Gaussian channels [119].

5.5 Quantized-Level Distributions

In this section, the coding scheme in Section 5.4 is applied to induce the maxentropic capacity-approaching input distributions presented in Chapters 3 and 4. Since this coding scheme can be applied to input distributions with quantized mass probabilities of the form $m/2^N$, it cannot be directly applied to the maxentropic distributions. Modified input distributions with quantized mass point probabilities are developed such that they are close to the maxentropic distribution in some measure and realizable using the MLC/MSD structure.

The maxentropic input distribution has, in general, the form

$$q(x) = \sum_k a_k \, \delta(x - k\ell).$$

Consider quantizing each probability mass amplitude to one of 2^N permissible quantization levels such that $a_k \in \mathcal{A}$ where $\mathcal{A}$ is the set of rational numbers of the form,

$$\mathcal{A}_N = \left\{ a : a = \frac{i}{2^N},\ i \in \{1, \ldots, 2^N - 1\} \right\}.$$

5.5.1 Average Power Constraint

Recall that the maxentropic input distribution under non-negativity and average optical power constraints is given by (see (3.5)),

$$q_\ell(x) = \sum_{k=0}^{\infty} \underbrace{\frac{\ell}{\ell + P} \left(\frac{P}{\ell + P} \right)^k}_{a_k} \delta(x - k\ell),$$

where $\{a_k\}$ is the collection of weights for each mass point. Although the mutual information using the source distribution $q_\ell(x)$ is close to the channel capacity the implementation of such a distribution is clearly impractical. As a result, consider a probability distribution with a finite number of mass points and quantized probability masses. Let M denote the number of mass points in the distribution and 2^N denote the number of quantization levels, i.e., $a_k \in \mathcal{A}_N$. Notice that the elements of $\{a_k\}$ satisfy

$$\forall i < j, \quad a_i > a_j$$

Based on this intuition, define the set $\tilde{\mathcal{Q}}_{\ell'}^{M,N}$ as follows,

$$\tilde{\mathcal{Q}}_{\ell'}^{M,N} = \left\{ \tilde{q}_{\ell'}(x) : a_k \in \mathcal{A}_N,\ a_k \geq a_{k+1},\ \sum_{k=0}^{M-1} \ell' k a_k \leq P,\ \tilde{q}_{\ell'}(x) = \sum_{k=0}^{M-1} a_k \delta(x - k\ell') \right\}.$$

Note that the mass point spacing ℓ' in this case is not a free parameter and is assigned so that the average optical power constraint is met, i.e.,

$$\ell' = \frac{P}{\sum_{k=0}^{M-1} k \, a_k}.$$

In this case the transmitter alphabet is

$$\mathcal{X} = \{0, \ell', 2\ell', \dots, (M-1)\ell'\}.$$

The optimum distribution within the set $\tilde{\mathcal{Q}}_{\ell'}^{M,N}$ is defined as the one that maximizes the mutual information $\mathbb{I}(X;Y)$ between the channel input and output, i.e.,

$$\tilde{q}_{\ell'}^{*}(x) \triangleq \arg \max_{f_X(x) \in \tilde{\mathcal{Q}}_{\ell'}^{M,N}} \mathbb{I}(X;Y). \tag{5.2}$$

For every SNR and choice of M and N, an exhaustive search is performed over $\tilde{\mathcal{Q}}_{\ell'}^{M,N}$ to find $\tilde{q}_{\ell'}^{*}(x)$. Notice that with the descending mass point probabilities order, the number of distribution in $\tilde{\mathcal{Q}}_{\ell'}^{M,N}$ is reduced and hence the search complexity can be reduced greatly. As an example, consider the case when $M = 2$ input symbols, i.e., $\mathcal{X} = \{0, \ell'\}$, with probabilities $\{q_0, q_{\ell'}\}$ and 2^N quantization levels. The permissible values for this pair are as follows,

$$\{q_0, q_{\ell'}\} \in \left\{ \frac{2^N - i}{2^N}, \frac{i}{2^N} \right\}, \quad i = 1, \dots, 2^{N-1},$$

where the size of $\tilde{\mathcal{Q}}_{\ell'}^{M,N}$ is approximately reduces to half with ordering.

5.5.1.1 Mutual Information of Quantized-levels distributions

In order to quantify the gain achieved by the proposed non-uniform discrete distributions, it is convenient to present bounds on the capacity of wireless optical channel to compare with. The lower bound C_{L} in (3.7), the tight upper bound at high SNR $H\&K_{\mathrm{U}}$ in [60] and the tight upper bound at low SNR C_{U} in (3.18) are presented in Fig. 5.8. For the sake of comparison, the mutual information for uniform 2-PAM and 4-PAM are also presented.

The mutual information between channel input and output considering the binary amplitude alphabet $\mathcal{X} = \{0, \ell'\}$ with $N = 2$, 3 and 4 encoders are shown by squares, circles and points respectively. Consider the case when $M = 2$ and $N = 2$ encoders,

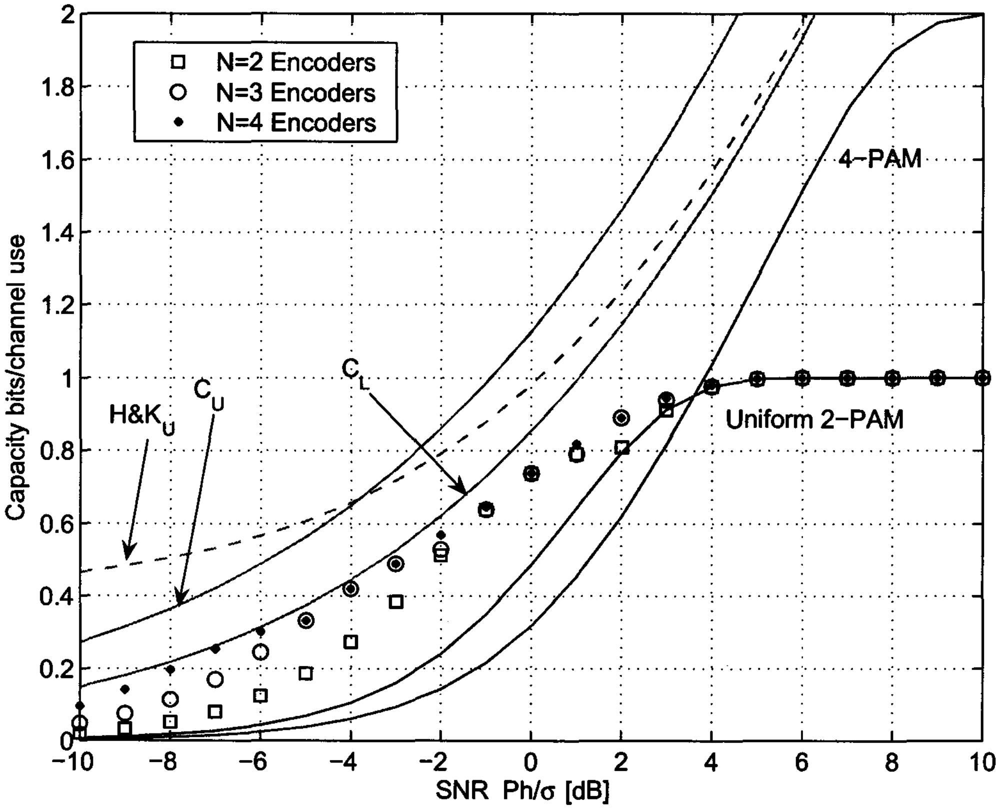

Figure 5.8: Average power constraint. Upper, $H\&K_{\text{U}}$ and C_{U} (3.18), and lower, C_{L} (3.7), bounds on the channel capacity and the mutual information using the quantized-level distributions for $N = 2, 3$ and 4 encoders, i.e., 4-, 8-, and 16-quantization levels respectively.

Table 5.1: Optimum Distribution and Peak Amplitudes for $M = 2$ and $N = 4$

SNR dB	-10...-6	-5...-3	-2...-1	0	1	2	3...4	5
q_0	$\frac{15}{16}$	$\frac{14}{16}$	$\frac{13}{16}$	$\frac{12}{16}$	$\frac{13}{16}$	$\frac{10}{16}$	$\frac{9}{16}$	$\frac{8}{16}$
Peak Amp. ℓ'/P	16	8	5.3	4	3.2	2.7	2.3	2

clearly two input distributions only exist in the set $\tilde{Q}_{\ell'}^{M,N}$ each with two mass points given by the pairs, $\{q_0, q_{\ell'}\} \in \left\{ \left\{\frac{1}{2}, \frac{1}{2}\right\}, \left\{\frac{3}{4}, \frac{1}{4}\right\} \right\}$. Over the range SNR $= [-10, 2]$ dB, the non-uniform input distribution $\left\{\frac{3}{4}, \frac{1}{4}\right\}$ achieves higher mutual information compared to the uniform 2-PAM signaling. Notice also that the mutual information approaches the channel capacity when the number of the quantization levels increases. This result is achieved with an increase in system complexity where the number of encoders is increased.

Consider the case when $M = 2$ and $N = 4$, the distribution $\tilde{q}_{\ell'}^{*}(x)$ that maximizes the mutual information at different SNRs is shown in Table 5.1 where integer values for SNR are considered. The points reported in the Table show the position where the distribution is changed, i.e., $\{q_0, q_{\ell'}\} = \{15/16, 1/16\}$ when SNR$\in \{-10, \ldots, -6\}$ dB. Notice that as SNR decreases, the resulting distribution becomes increasingly non-uniform tending to send zero amplitudes more often. Also notice that, the normalized peak amplitude, ℓ'/P, also increases as SNR decreases. Qualitatively, at low SNR the transmitter "saves" the average optical power constraint over longer periods of times and sends a one-shot high intensity, high entropy output infrequently. Of course, there is a limit to the applicability of such techniques since in general the peak output power is limited by safety standards.

At low SNR, increasing the quantization levels, 2^N, i.e., number of encoders in MLC, results in a higher mutual information with an increase in the encoding/decoding complexity in the MLC/MSD system. Although it might be expected that increasing the quantization levels number results in a higher mutual information, this is not exactly true in all cases. As an example, the mutual information when $N = 3$ and $N = 4$ are the same when SNR=-4 dB as shown in Fig. 5.8 where $q_0 = 7/8 = 14/16$, i.e., realizable when $N = 3$ and 4 respectively. Furthermore, when SNR=-1 dB the non-uniform distributions with $N = 2, 3$ and 4 have mutual information that is close to the lower bound C_{L}. As a result, two encoders, $N = 2$, can be utilized with reduced complexity compared to $N = 3$ and 4 encoders.

5.5.1.2 Non-uniform Signaling Algorithm

A remarkable gap in the mutual information can be noticed between the uniform and the non-uniform input distributions at low SNR. For example, consider designing a system at SNR=-6 dB with $M = 2$ mass points and $N = 3$ encoders. In this case, the non-uniform discrete distribution achieves approximately 0.24 bits/channel use with $\{q_0, q_1\} = \{7/8, 1/8\}$ while uniform 2-PAM achieves approximately 0.04 bits/channel use. Notice that the maxentropic input distribution, $q_\ell^*(x)$ in (3.6), achieves mutual information, i.e., C_{L}, of approximately 0.3 bits/channel use. In order to induce the input distribution with $q_0 = 7/8$, the deterministic mapper $\mathcal{M}$ is given as,

$$\boldsymbol{W} = [W_1, W_2, W_3] \overset{\mathcal{M}}{\longmapsto} X : X = \begin{cases} 1 & \text{if } W_1 = W_2 = W_3 = 1, \\ 0 & \text{otherwise.} \end{cases} \tag{5.3}$$

The sub-channels rates $\mathbb{I}(W_1; Y)$, $\mathbb{I}(W_2; Y|W_1)$ and $\mathbb{I}(W_3; Y|W_1, W_2)$ and the total mutual information $\mathbb{I}(W; Y)$ versus SNR are shown in Fig. 5.9. Notice that unlike MLC/MSD systems for RF channels where some bits may be transmitted uncoded, it is not possible to transmit any uncoded bits this example. Clearly, all rates R_i approach their maximum value at approximately the same SNR. From Fig. 5.9 and at SNR $= -6$ dB, the total rate $\mathbb{I}(\boldsymbol{W}; Y) = \mathbb{I}(X; Y) = 0.24$ bits/channel use is divided over the sub-channels as follows: $\mathbb{I}(W_1; Y) = 0.05$, $\mathbb{I}(W_2; Y|W_1) = 0.07$ and

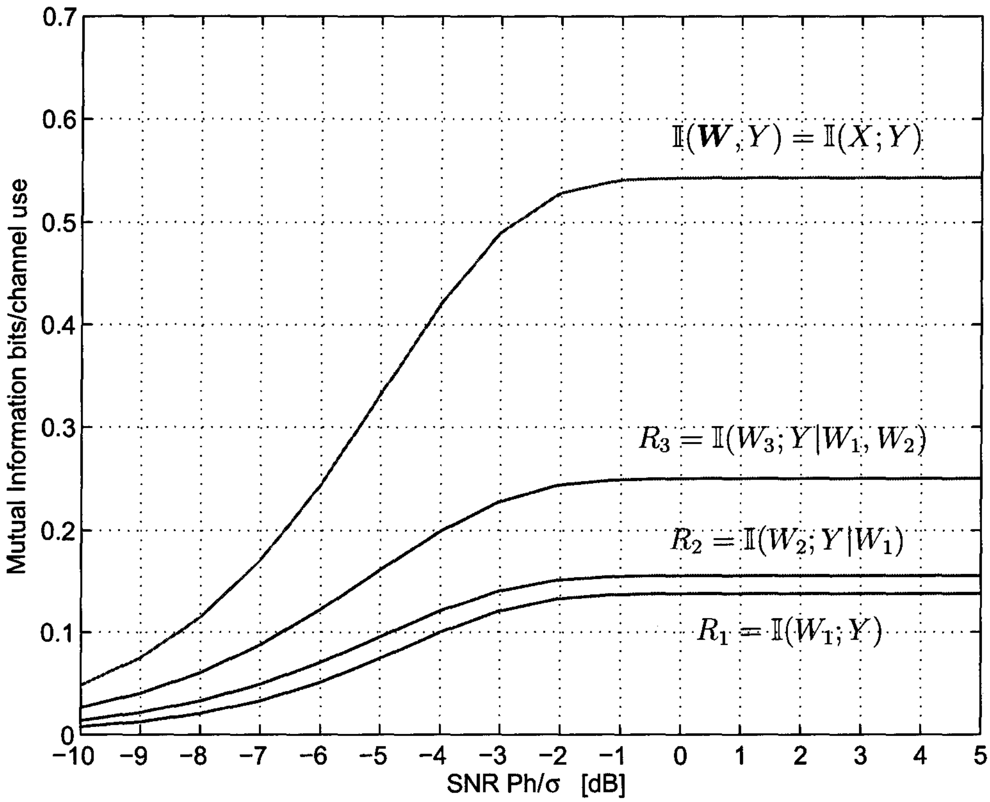

Figure 5.9: Average power constraint. The mutual information versus SNR for each sub-channel in the MLC system using $N = 3$ encoders to generate input distribution $\{q_0, q_1\} = \{7/8, 1/8\}$. The rates are given by $R_1 = \mathbb{I}(W_1;Y)$, $R_2 = \mathbb{I}(W_2;Y|W_1)$ and $R_3 = \mathbb{I}(W_3;Y|W_1,W_2)$.

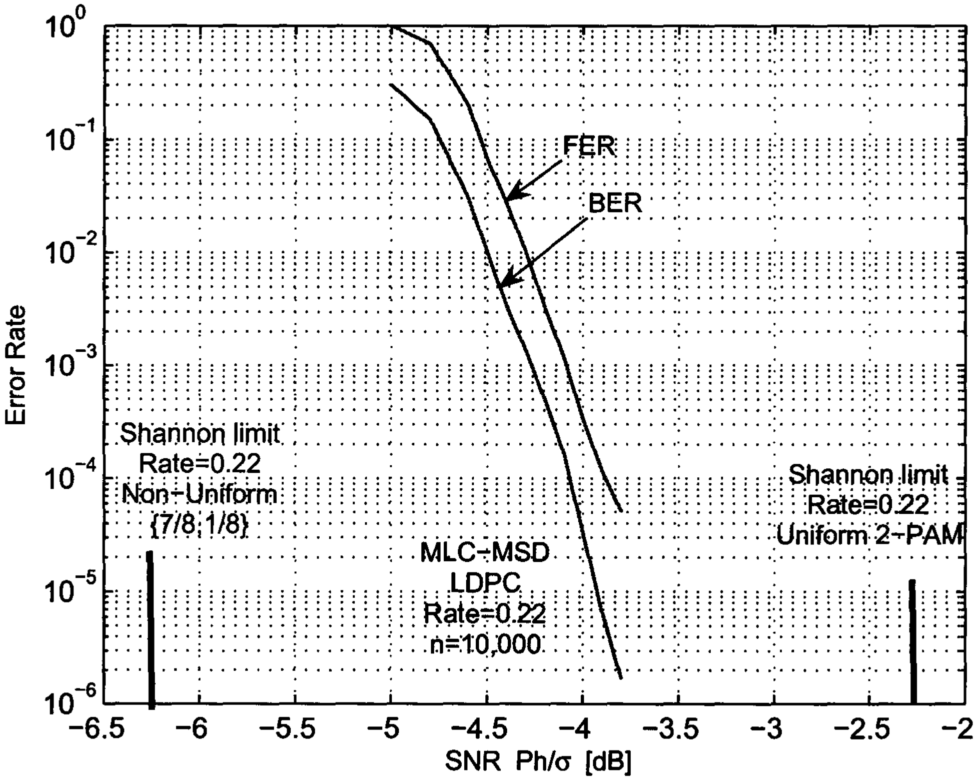

Figure 5.10: Average power constraint. BER and FER for MLC system using LDPC codes with rate $R_1 = R_2 = 0.05$ and $R_3 = 0.12$. The Shannon limit for both the uniform 2-PAM and the non-uniform distributions with $N = 3$ is shown.

$\mathbb{I}(W_3; Y|W_1, W_2) = 0.12$ bits/channel use.

However, capacity achieving codes are required to achieve these rates at SNR = -6 dB. Finite-length LDPC codes with codeword length $n = 10,000$ are utilized with rates $R_1 = 0.05$, $R_2 = 0.05$ and $R_3 = 0.12$, i.e., the total rate is $R = \sum_i R_i = 0.22$ bits/channel use. The parity check matrices are constructed according to a degree distribution that is designed for Gaussian channels at each rate [119].

Figure 5.10 shows the performance of the MLC system using practical finite length LDPC codes for different SNRs. The bit error rate (BER) versus SNR is presented as a performance measure. The Shannon limit for a given rate is defined as the minimum SNR at which there exists a code such that the received codeword is decoded reliably, i.e., arbitrary small probability of error. The Shannon limits at rate $R = 0.22$ bits/channel use for both the uniform 2-PAM and the non-uniform distributions with $N = 3$ are shown in Fig. 5.10 and are given by -2.3 dB and -6.25 dB respectively. The non-uniform distribution using finite LDPC codes outperforms the uniform 2-PAM with a capacity-achieving code. Quantitively, the non-uniform distribution with practical LDPC codes achieves BER $= 3 \times 10^{-5}$ at SNR =-4 dB which is 1.7 dB below the Shannon limit using a uniform input distribution. As a result, non-uniform signaling is the solution for high data rate communication over optical channel.

5.5.2 Peak and Average Power Constraints

In this section quantized-level distributions for the non-uniform input distributions presented in Chapter 4 are developed where both peak and average power constraints is considered.

Recall (4.9) and the fact that $0 < t_0 < 1$ as shown in Lemma F.1, then the elements of $\{\bar{a}_k\}$ have a descending order, i.e., for all $i < j$ then $\bar{a}_i > \bar{a}_j$. Define the set $\breve{\mathcal{Q}}_K$ as the set of all discrete input distributions with $K + 1$ equally spaced mass points with descending quantized mass amplitudes satisfying both peak and average power constraints as follows,

$$\breve{\mathcal{Q}}_K^N = \left\{ \breve{q}_X(x;K) : a_k \in \mathcal{A}_N,\ a_k \geq a_{k+1}, \ell > 0,\ \sum_{k=0}^{K} k\ell a_k \leq P,\ \ell \leq \frac{A}{K}, \right.$$
$$\left. \breve{q}_X(x;K) = \sum_{k=0}^{K} a_k \delta(x - k\ell) \right\}.$$

Define the set $\breve{\mathcal{Q}}^N$ as the collection of all input distributions for all K,

$$\breve{\mathcal{Q}}^N = \bigcup_{K=1} \breve{\mathcal{Q}}_K^N$$

For a given SNR, the search for the distribution that maximizes the mutual information within the set $\breve{\mathcal{Q}}^N$ is difficult. Based on the intuition that, for a given K, the input distribution in $\breve{\mathcal{Q}}^N$ that closely resembles the maxentropic input distribution, $\bar{q}_X(x;K)$ (4.8), would perform well, consider the set $\tilde{\mathcal{Q}}^N$ given by,

$$\tilde{\mathcal{Q}}^N = \bigcup_{K} \tilde{\mathcal{Q}}_K^N.$$

where

$$\tilde{\mathcal{Q}}_K^N = \left\{ \tilde{q}_X(x;K) \in \breve{\mathcal{Q}}^N :\ \tilde{q}_X(x;K) = \arg\min_{\breve{q} \in \breve{\mathcal{Q}}_K^N} \mathcal{D}\Big(\bar{q}_X(x;K) || \breve{q}_X(x;K)\Big) \right\}, \quad (5.4)$$

and $\mathcal{D}$ is the relative entropy (Kullback-Leibler distance) defined as

$$\mathcal{D}\Big(\bar{q}_X(x;K) || \breve{q}_X(x;K)\Big) = \sum_{k=0}^{K} \bar{a}_k \log\left(\frac{\bar{a}_k}{\breve{a}_k}\right).$$

where $\bar{q}_X(x;K)$ is defined in (4.8). Once $\tilde{\mathcal{Q}}^N$ is formed, the input distribution that maximizes the mutual information is selected, i.e.,

$$\tilde{q}_X^*(x;\tilde{K}) = \arg \max_{\tilde{q}_X(x;K) \in \tilde{\mathcal{Q}}^N} \mathbb{I}(X;Y|H=h), \quad (5.5)$$

where $\tilde{K}+1$ is the number of mass points associated with $\tilde{q}_X^*(x;\tilde{K})$.

The saving in computation arises due to the following facts. For a given K a unique input distribution $\bar{q}_X(x;K)$ (4.8) is obtained since t_0 is unique (see Appendix F). Consequently and unlike $\breve{\mathcal{Q}}_K^N$, for a given K there exists a smaller number of input distributions in $\tilde{\mathcal{Q}}_K^N$. Hence the number of input distributions in $\tilde{\mathcal{Q}}^N$ is much smaller than that in $\breve{\mathcal{Q}}^N$. As a result, searching for the distribution that maximizes the mutual information at a given SNR within $\tilde{\mathcal{Q}}^N$ is much simpler than within $\breve{\mathcal{Q}}^N$. Furthermore, computing the relative entropy, $\mathcal{D}$, is much simpler than numerically simulating the mutual information for all input distributions in $\breve{\mathcal{Q}}_K^N$.

In order to emphasize the computational savings, consider the following example. The mass points probabilities of the input distributions in $\breve{\mathcal{Q}}_2^3$, i.e., $2^N = 8$ quantization levels and $K+1 = 3$ mass points, when $\rho = 4$ are given by,

$$\underbrace{\left[\frac{3}{4},\frac{1}{8},\frac{1}{8}\right],\left[\frac{5}{8},\frac{1}{4},\frac{1}{8}\right]\left[\frac{1}{2},\frac{3}{8},\frac{1}{8}\right]\left[\frac{1}{2},\frac{1}{4},\frac{1}{4}\right]\left[\frac{3}{8},\frac{3}{8},\frac{1}{4}\right]}_{K=2 \text{ and } \rho=4}. \tag{5.6}$$

Note that for a given K and ρ a unique maxentropic distribution $\bar{q}_X(x;K)$ exists (see Proposition 4.1). When $K = 2$ and $\rho = 4$ the mass points probabilities of $\bar{q}_X(x;K)$ are given by,

$$\underbrace{\left[0.6162, 0.2676, 0.1162\right]}_{K=2 \text{ and } \rho=4},$$

as shown in Fig. 4.3. Applying the Kullback-Leibler distance criterion in (5.4) to this example results in a single input distribution in $\tilde{\mathcal{Q}}_2^3$ when $\rho = 4$ given by,

$$\underbrace{\left[\frac{5}{8},\frac{1}{4},\frac{1}{8}\right]}_{K=2 \text{ and } \rho=4}. \tag{5.7}$$

Note that the input distributions in $\breve{\mathcal{Q}}_K^N$ and $\tilde{\mathcal{Q}}_K^N$ are not a function of SNRs. In general, a computational saving is obtained when $\tilde{\mathcal{Q}}^N$ is considered. Note that, the spacing ℓ is set such that both peak and average power constraints are satisfied. The input distribution within $\tilde{\mathcal{Q}}^N$ that maximizes the mutual information in (5.5) is then selected. However, selecting input distributions based on relative entropy to form the set $\tilde{\mathcal{Q}}^N$ can lead to mutual information degradations since there is a probability that other distributions in $\breve{\mathcal{Q}}^N$ may have higher mutual information. In the following section the mutual information using the input distributions in $\tilde{\mathcal{Q}}^N$ is analyzed to emphasis the effects of both, the relative entropy approach and the quantization technique, on the rate loss.

5.5.2.1 Channel Capacity and Mutual Information

The channel capacity and the mutual information, in bits/channel use, are shown in Fig. 5.11 for the 4- and 8-quantized-levels distributions at peak-to-average optical power ratio $\rho = 4$. For comparison, the uniform input distribution is also presented. Notice that the mass points for the uniform distributions utilized in the simulation are equally distributed in the interval $[0, 2P]$ which guarantees that both the peak and the average power constraints are satisfied as given in (4.12). The mass points probability of the non-uniform distributions in $\breve{\mathcal{Q}}^2$ with $2^N = 4$ quantization levels are given by,

$$\underbrace{\left[\frac{3}{4}, \frac{1}{4}\right], \left[\frac{1}{2}, \frac{1}{2}\right]}_{K=1} \underbrace{\left[\frac{1}{2}, \frac{1}{4}, \frac{1}{4}\right]}_{K=2} \underbrace{\left[\frac{1}{4}, \frac{1}{4}, \frac{1}{4}, \frac{1}{4}\right]}_{K=3} \tag{5.8}$$

Fig. 5.11 presents the maximum mutual information for the 4- and 8-quantized-levels input distributions in $\tilde{\mathcal{Q}}^2$ and $\tilde{\mathcal{Q}}^3$ respectively. Notice that, the mutual information for 4- and 8-quantized levels distributions at low SNR coincide with the channel capacity. This occurs since the capacity-achieving input distribution $f_X^*(x)$ obtained via solving the optimization problem numerically is given as, $f_X^*(x) = 0.75\,\delta(x) + 0.25\,\delta(x - A)$ which can be realized using both the 4- and 8-quantization levels distributions. When SNR$\in [-6, -1]$, the non-uniform distribution approximately achieves double the rate compared to the uniform input distribution. These rates can be realized using only two encoders in the MLC structure compared to one

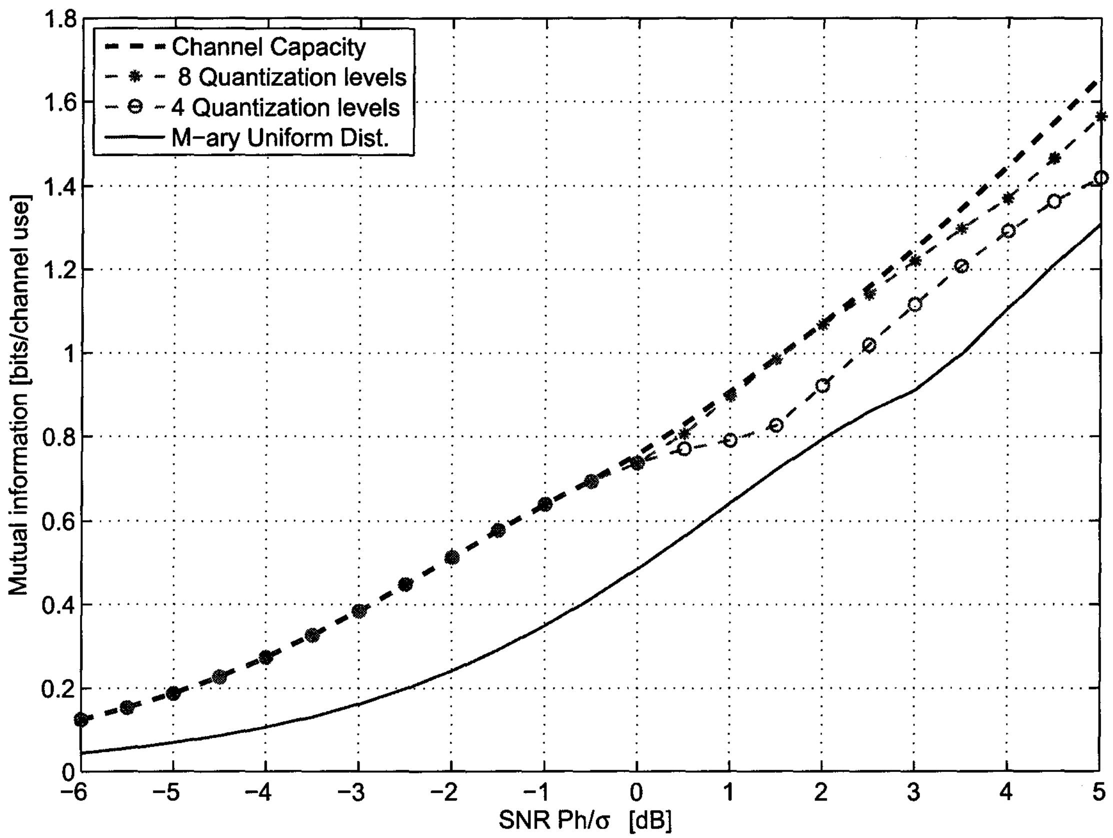

Figure 5.11: Peak and average power constraints. Channel capacity and mutual information for the M-ary uniform and the quantized input distribution with 4- and 8-quantization levels for $\rho = 4$.

encoder utilized in case of uniform input distribution and hence double the rate is achieved with relatively higher complexity. When SNR increases to SNR$\in [1, 4]$ dB, the 8 quantized-level distributions are capable to closely approach the channel capacity. However, the 4 quantized-level distributions incur a rate degradation on the order of 0.1 bits/channel use.

For comparison, the mutual information, in bits/channel use, using the relative entropy and the exhaustive search methods, i.e., input distributions in $\tilde{\mathcal{Q}}^3$ and $\breve{\mathcal{Q}}^3$

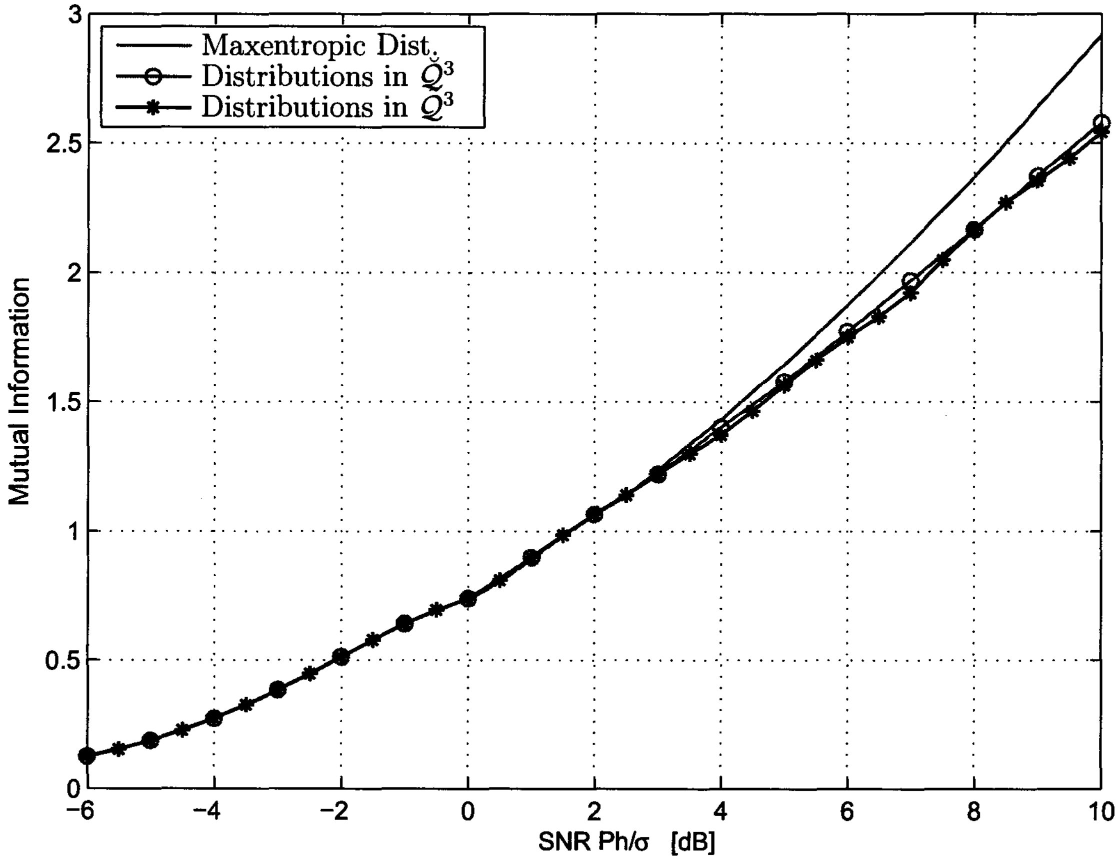

Figure 5.12: Peak and average power constraints. Mutual information using, the maxentropic input distribution $\bar{q}_X^*(x; K)$ (4.6), the 8-quantized level distribution in $\check{Q}^3$, and the 8-quantized level distribution in $\tilde{Q}^3$ for $\rho = 4$.

respectively, is shown in Fig. 5.12. The mutual information is computed over $\breve{\mathcal{Q}}^3$ using exhaustive search over all input distributions where the mass points spacing, ℓ, is set such that both peak and average power constraints are satisfied. As shown at low SNRs the two methods result in a close mutual information, however, at high SNR a small degradation can be noticed. Note that, at high SNR a large gap can be seen between the mutual information using these two methods and the mutual information using the maxentropic input distributions $\bar{q}_X(x; K)$ showing that a larger number of quantization levels is required. As a result, the relative entropy method provides a higher computational saving and a negligible degradation in mutual information compared to the exhaustive search method.

5.5.2.2 Number of Mass Points

In order to provide more insights to the capacity results, the number of mass points that maximizes the mutual information in Fig. 5.11 for each case is presented in Fig. 5.13 versus SNR. The number of mass points $\bar{K}+1$ in the maxentropic input distribution $\bar{q}^*(x;\bar{K})$ and $\tilde{K}+1$ in the the 4- and 8-quantized levels distributions $\tilde{q}^*(x;\tilde{K})$ those maximize the mutual information for different SNRs are shown in Fig. 5.13. The simulation is carried out over a range of SNR$\in[-4,5]$ dB with step size 0.5 dB. When SNR varies in the range $[-4,0]$ dB, clearly two mass points can achieve the highest mutual information. When SNR increases and unlike the 4-quantized-levels distribution, the maxentropic and the 8-quantized-levels distributions have the same number of mass points, however, the mass points amplitudes are different.

The input mass point amplitudes for 4- and 8-quantized-levels distributions are presented in Table 5.2 and Table 5.3 respectively. For a given SNR range, the number, the probabilities and the spacing of the mass points are presented. Although from Fig. 5.13 and at SNR=2 dB, three mass points are utilized for both 4- and 8-quantized-level distributions, the quantized distribution is not the same where from

Table 5.2: Input distribution $2^N = 4$ quantization levels

SNR	Number of Mass Points	Mass Points Probabilities	Mass Points Spacing ℓ
[-4,1]	2	$\{0.75, 0.25\}$	A
[1.5,5]	3	$\{0.5, 0.25, 0.25\}$	$A/3$

Table 5.3: Input distribution $2^N = 8$ quantization levels

SNR	Number of Mass Points	Mass Points Probabilities	Mass Points Spacing ℓ
[-4,0]	2	{ 0.75, 0.25 }	A
[-0.5,2.5]	3	{ 0.625, 0.25, 0.125 }	$A/2$
[3,4]	4	{ 0.625, 0.125, 0.125, 0.125 }	$A/3$
[4.5,5]	5	{ 0.5, 0.125, 0.125, 0.125, 0.125 }	$A/5$

Table 5.2 and Table 5.3 the mass points amplitudes are given by $\{0.5, 0.25, 0.25\}$ and $\{0.625, 0.25, 0.125\}$ respectively where the mass points are spaced by $A/3$ and $A/2$ respectively. At SNR=2 dB, the 4- and 8-quantized-levels distributions achieve rates of 0.92 bits/channel use and 1.06 bits/channel use where two and three encoders are employed in the MLC system respectively. Thus, in system design, rate and complexity tradeoff controls which method will be considered.

5.5.2.3 Algorithm Performance

In this part we consider the design of MLC/MSD system to achieve the rates reported in the previous section. Since the main concern in wireless optical system is the operation at low SNR regime, e.g fog weather condition, we consider system design

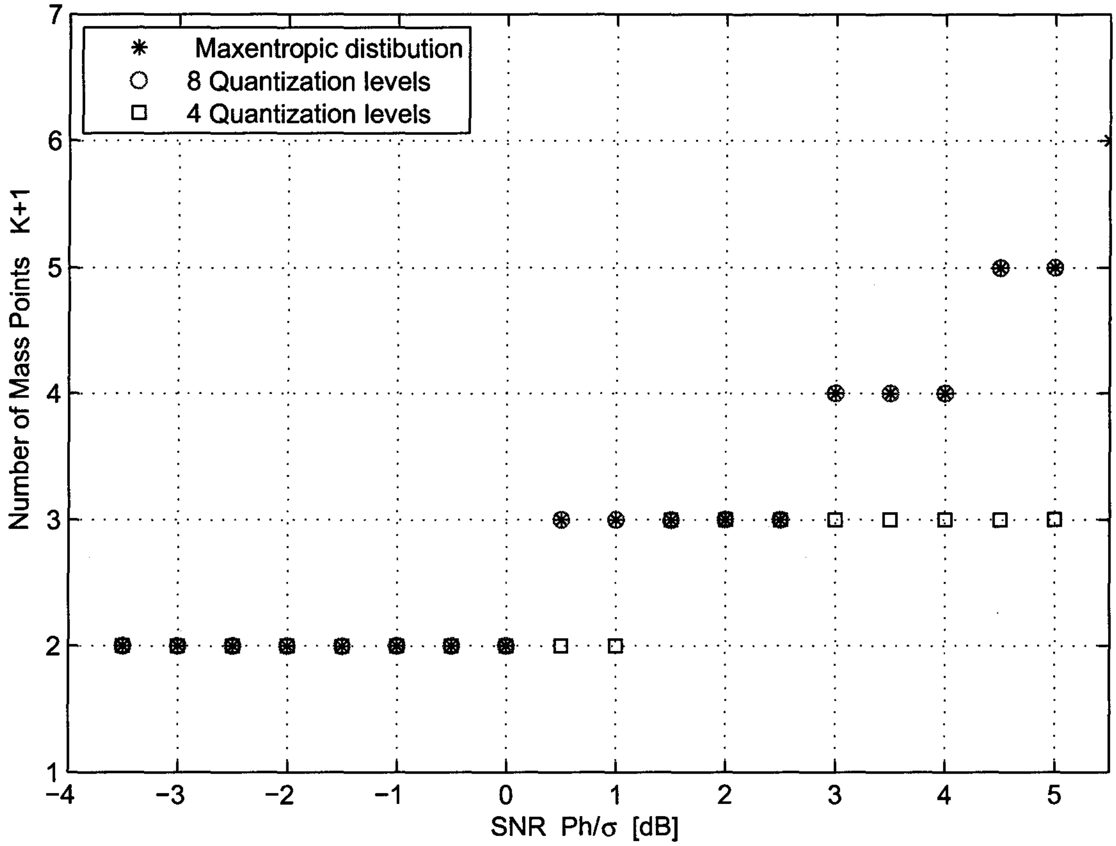

Figure 5.13: Peak and average power constraints. Number of mass points versus SNR at 4- and 8- quantization levels. The number of mass points using the maxentropic input distribution $\bar{q}_X^*(x, K)$ with real valued amplitudes is also shown $\rho = 4$.

at SNR=-5 dB where the performance will be compared with the conventional uniform distribution that is used in current commercial systems. The corresponding channel capacity at SNR=-5 dB is 0.187 bits/channel use (Fig. 5.11), which is achievable using 4- and 8-quantization level input distributions. This rate is achieved when employing the input distribution $q^*(x;1) = 0.75\ \delta(x) + 0.25\ \delta(x-A)$ which can be implemented using two encoders followed by a mapper with a mapping function,

$$\boldsymbol{W} = [W_1, W_2] \overset{\mathcal{M}}{\longmapsto} X : X = \begin{cases} 1 & \text{if } W_1 = W_2 = 1, \\ 0 & \text{otherwise.} \end{cases} \tag{5.9}$$

The sub-channels rates $R_1 = \mathbb{I}(Y;W_1)$, and $R_2 = \mathbb{I}(Y;W_2|W_1)$ and the total rate $\mathbb{I}(X;Y) = R_1 + R_2$ are shown in Fig. 5.14 versus SNR. At SNR=-5 dB, the sub-channels mutual information are $\mathbb{I}(W_1;Y) = 0.066$ and $\mathbb{I}(W_2;Y|W_1) = 0.121$ bits/channels use with total information rate $\mathbb{I}(X;Y) = R_1 + R_2 = 0.187$ bits/channels use. Since it is not straightforward to generate LDPC codes with rates $R_1 = 0.066$ and $R_2 = 0.121$, a simple approach is considered where LDPC codes with rates $R_1 = 0.05$ and $R_2 = 0.12$ with length $n = 10,000$ are designed. This step is proposed since a degree distribution for LDPC codes with the mentioned rates can be found in [119], and hence the system is designed to operate at rate $R_0 = 0.17$ bits/channel use.

The performance of the MLC/MSD wireless optical intensity system using practical finite length LDPC codes in terms of bit-error-rate (BER) versus SNR is shown in Fig. 5.15. Shannon limit at rate 0.17 (bits/channel use) for both non-uniform input distribution, i.e., $q(x) = 0.75\ \delta(x) + 0.25\ \delta(x-A)$ and the uniform input distribution, i.e., $q(x) = 0.5\ \delta(x) + 0.5\ \delta(x-2P)$, are plotted and given by -5.25 dB and -2.8 dB respectively.

These limits can be deduced from Fig. 5.11 directly. The proposed non-uniform distribution with practical LDPC codes achieves BER $= 3 \times 10^{-6}$ at SNR=-3.7 dB that is approximately 1.55 dB higher than the Shannon limit of the non-uniform

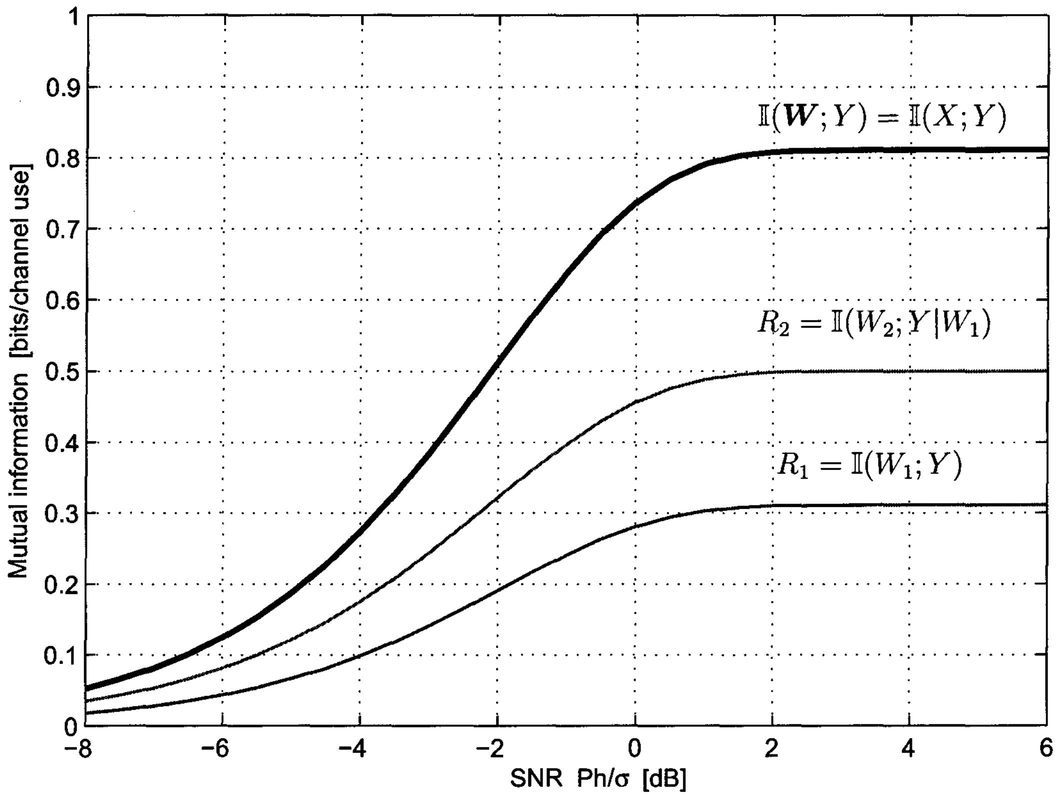

Figure 5.14: Peak and average power constraints. Sub-channels rate for the MLC system using two mass points with probabilities $[\frac{3}{4}, \frac{1}{4}]$ at $\rho = 4$.

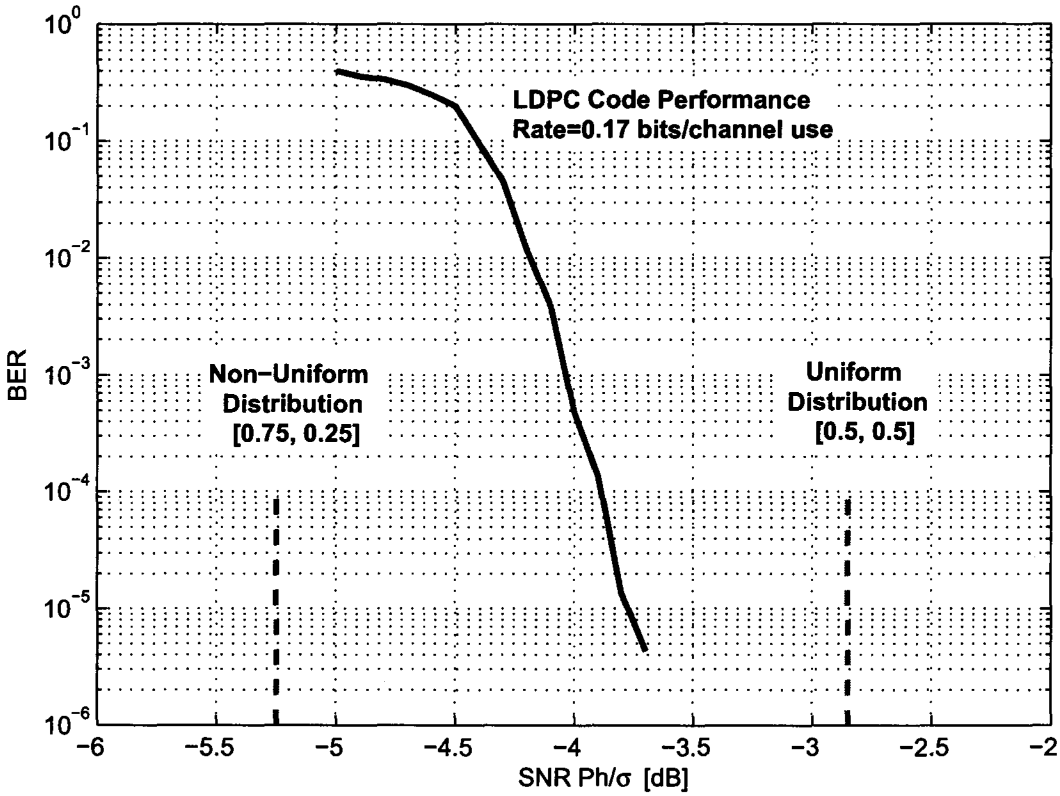

Figure 5.15: Peak and average power constraints. The optimum and the proposed input distribution for different SNRs with $\rho = 4$.

distribution. The non-uniform distribution using finite length LDPC codes is smaller than the Shannon limit of the uniform distribution by 0.9 dB. Hence non-uniform distributions are important for optical channels.

5.6 Conclusion

In [88] it was shown that non-uniform distributions can be induced using a deterministic mapper where the encoding/decoding is realized using a multi-level coding and a multi-stage decoding structure.

In this chapter, the algorithm in [88] is applied to realize the non-uniform input distributions proposed for optical intensity channels. Modified non-uniform input distributions with quantized probabilities are developed such that they can be realized with small number of encoders. We demonstrate that with three encoders the realized rates are close to the channel capacity over a wide range of SNRs. Design examples of non-uniform optical intensity systems are presented. The performance of the system is analyzed through BER versus SNR measure using LDPC codes and two input symbols. It is shown that, the performance of finite length LDPC codes with non-uniform signaling outperform the Shannon limit of the uniform signaling.

In Chapters 3 and 4 information theoretic limits for wireless optical intensity channels are developed for a given channel state realization. In the following chapter these results will be used to study the free-space optical channels with time varying fading. Since a slow-fading model is considered for the FSO channel, the channel capacity subject to outage is analyzed. Both atmospheric turbulence and misalignment fading effects are considered through the statistical channel models developed in Chapter 2.

Chapter 6

Capacity and Outage for Fading FSO Channels

In Chapters 3 and 4, the instantaneous channel capacity at a given channel realization is analyzed for optical intensity channels. An algorithm to realize the achievable rates is presented in Chapter 5. In this chapter, the design and performance of FSO communication links over slow-fading channels from an information theory perspective are investigated. In particular, the transmitted rate and the associated probability of outage over fading FSO channels is computed. These two quantities together define the *outage capacity*. The combined effects of atmospheric turbulence and pointing errors are considered and expressions for the outage probability are derived for a variety of atmospheric conditions. For given weather and misalignment conditions, the beamwidth is optimized to maximize the rate subject to an outage probability. Large gains in achievable rates are realized using the optimum beamwidth versus a fixed nominal beamwidth at a given outage probability. In addition, comparisons between the uniform and the non-uniform signaling developed in Chapters 3 and 4 are presented showing significant gains in rates and reduction in probability of outage.

6.1 Introduction

Misalignment fading has gained much attention due to its significant impact on the terrestrial FSO links performance. BER and power minimization over turbulence-free channels was studied in [52]. This work was extended to include atmospheric turbulence fading in [51]. Numerical analysis for target tracking was also considered in [55]. Probability density functions considering atmospheric turbulence and misalignment for point receivers were developed in [54] for extremely long distance communications.

Since an FSO channel can be well modeled as a slow-fading channel, outage capacity for Poisson noise model has been derived in the absence of misalignment errors [120]. Extension to the multiple-input multiple-output case was developed in [121]. Also for Gaussian noise channel the outage capacity was analyzed for OOK in [36]. The performance of different spatial and temporal detection techniques to mitigate atmospheric turbulence were given in [31] and [122] where only the atmospheric turbulence fading is considered. Bounds on the pairwise codeword error probability were developed and utilized to derive upper bound on bit error rate for atmospheric turbulence channels [78, 82].

The performance of FSO channels has been investigated either under atmospheric turbulence or misalignment fading and rarely have these effects been combined. Also the analysis and design of FSO links are confined to uniform signaling either using OOK (2-PAM) or higher constellation, e.g., M-ary PAM. Even the term *channel capacity* in the previous work was commonly focused on OOK signaling, e.g., [36, 80]. Furthermore, the joint design of code rate and beamwidth to maximize the channel capacity has not been considered.

This chapter presents a formal method to jointly design the beamwidth and code rate for FSO channels impaired by turbulence and misalignment induced fading. For given atmospheric and misalignment fading statistics, the channel is engineered by selecting the beamwidth that maximizes the outage capacity. Since the channel state varies on the order of millions of symbol intervals, we adopt a slow fading channel model and derive expressions for the outage probability for weak and strong turbulence conditions. A key novelty of this work is the consideration of beamwidth optimization to maximize the channel capacity in FSO systems. For a given outage probability the beamwidth which maximizes the achievable rate for uniform on-off keying (OOK) is selected. It is shown that by selecting the optimum beamwidth versus a nominal one used in a commercial system gives large increases in achievable rates. Well-known error control codes with appropriate rates and complexity are then applied to the channel and shown to realize a large portion of the promised gains. This work is also extended where the outage capacity is optimized over the non-uniform input distributions developed for FSO channels in previous chapters. We demonstrate that non-uniform signaling achieves higher outage capacity compared to uniform for a variety of FSO fading channels when both atmospheric turbulence and misalignment fading are considered.

6.2 Outage Capacity

Since typical time scales of the FSO fading processes varies approximately in the range $10^{-3} - 10^{-2}$ sec [31], then for high bit rate transmission, in order of Gbps, it is more realistic to model the FSO channel as a slow-fading channel. In this case a transmitted block approximately spans a coherence time where the channel gain is constant over a block. Notice that the use of interleaving to allow for averaging over a large number of fading states is impractical in this case. Two scenarios are considered for transmission over slow fading channels either utilizing a fixed or a variable rate at the transmitter. When a fixed rate is utilized channel state information at the receiver is required which can be estimated by transmitting a training sequence, i.e., pilot symbols. In order to increase the average rate, rate adaptation can be employed at the transmitter, however, channel state information at the transmitter is required which can be sent from the receiver through a feedback link [36]. In this chapter the fixed rate scenario is considered. For a given fixed transmission rate, there is a finite probability that the transmitted rate exceeds the instantaneous mutual information of the channel leading to an outage event. The outage event is mathematically described by the probability of outage, i.e., the probability that the transmitted rate exceeds the instantaneous mutual information of the channel. Since each data rate has a corresponding probability of outage, these two pairs are grouped to define the *outage capacity*, i.e., a given rate can be reliably transmitted over a slow-fading channel with an associated probability of outage.

Recall the mutual information expression given in (3.2) and let $\mathcal{R}(h)$ denotes the instantaneous mutual information at a given signal-to-noise ratio, $\mathrm{SNR}(h)$, i.e., channel state h, with input distribution $f_X(x)$ as,

$$\mathcal{R}(h) = \mathbb{I}(X; Y|H = h),$$

where the received optical $\mathrm{SNR}(h)$ is random and is given as,

$$\mathrm{SNR}(h) = \eta R_v \frac{Ph}{\sigma}. \tag{6.1}$$

The responsivity R_v and the optics efficiency η, discussed in Chapter 2, are considered to introduce the attenuation effect of a practical FSO transmitter and receiver. For a given rate R_0, the probability of outage is given by,

$$P_{\mathrm{out}}(R_0) = \mathrm{Prob}\Big(\mathcal{R}(h) < R_0\Big).$$

In this context the *outage capacity* is defined as the pair (R_0, P_{out}). Consider the monotonic increase of $\mathcal{R}(h)$ with h, i.e., SNR for a given P and σ, as shown in Chapters 3 and 4. The outage probability can be rewritten as,

$$P_{\mathrm{out}}(R_0) = \mathrm{Prob}(h < h_0),$$

where the threshold h_0 is given by,

$$\mathcal{R}(h_0) = R_0.$$

The probability of outage is the cumulative density function of H evaluated at h_0 and is expressed as,

$$P_{\text{out}}(R_0) = \int_0^{h_0} f_H(h; w_o, \phi) dh. \tag{6.2}$$

where $f_H(h; w_o, \phi)$ is the channel probability density function presented in Chapter 2. Notice that, the tradeoff between R_0 and P_{out} is parametrized by the beamwidth w_o.

In the following analysis the outage capacity is optimized over beamwidth and input distribution selection. Under weak turbulence conditions both log-normal and Gamma-Gamma density functions can be used to describe the intensity fluctuation. However, a closed form expression for $P_{\text{out}}(R_0)$ can be obtained when log-normal fading is considered. Recall the log-normal distribution discussed in Chapter 2 and using the identity [123, Sec 3.2]

$$\int e^{bu} \operatorname{erfc}(au)\, dz = \frac{1}{b}\left[e^{bu}\operatorname{erfc}(au) - e^{\frac{b^2}{4a^2}} \operatorname{erf}\left(\frac{b}{2a} - au\right)\right],$$

the outage probability is expressed as,

$$P_{\text{out}}(R_0) = \frac{1}{2}\left[e^{\gamma^2\Xi - 2\sigma_\chi^2\gamma^4} \operatorname{erfc}\left(\frac{\Xi}{\sqrt{8}\sigma_\chi}\right) + \operatorname{erfc}\left(\frac{4\sigma_\chi^2\gamma^2 - \Xi}{\sqrt{8}\sigma_\chi}\right)\right],$$

where $\Xi = \ln(h_0/A_0 h_\ell) + 2\sigma_\chi^2(1 + 2\gamma^2)$. For strong turbulence regime the Gamma-Gamma density function is substituted into (6.2) and $P_{\text{out}}(R_0)$ is computed numerically. In all cases, the aperture averaging effect is taken into account and Gaussian beam is considered.

6.3 FSO Link Design Criteria

A tradeoff between the achievable rate, R_0, and the corresponding probability of outage $P_{\text{out}}(R_0)$ exists. This tradeoff is governed by both the statistical fading model through the beamwidth and the input distribution. For a given R_0, the beamwidth and the input distribution are selected to minimize P_{out}. Alternatively, for a required target P_{out}, the achievable code rate R_0 can be maximized. The design approach considered in this chapter is summarized as follows. For a given transmitted rate R_0, the optimum beamwidth w_o^{opt} that minimizes the outage probability is selected. The optimum beamwidth is defined as

$$w_o^{\text{opt}} = \arg \min_{w_o \in \mathcal{W}} P_{\text{out}}(R_0; w_o). \tag{6.3}$$

where $\mathcal{W}$ denotes the set of permissible beamwidths at the transmitter. The minimum probability of outage for a given rate R_0 is given by

$$P_{\text{out}}(R_0; w_o^{\text{opt}}) = \min_{w_o \in \mathcal{W}} P_{\text{out}}(R_0; w_o) \tag{6.4}$$

This approach is presented in the following steps,

$$\text{Given } R_0 \longrightarrow \text{Obtain } h_0 \xrightarrow{\text{Substitute}} P_{\text{out}}(R_0; w_o) \xrightarrow[w_o \ Eq. \ (6.3)]{\text{Select}} P_{\text{out}}(R_0; w_o^{\text{opt}})$$

A rate R_0 is termed *achievable* if there exists a family of codes of code rate R_0 which can realize any, arbitrarily small, probability of error. Of course, practical fixed length codes will have a non-zero probability of error, however, good finite length codes approaching Shannon's capacity have been found. Thus, our goal is to first engineer the channel to have a high capacity through optimizing the beamwidth w_o and then to apply error correcting codes to approach these information theoretic limits. Even after optimization, however, not all pairs of (R_0, P_{out}) are achievable. In this work we define the *unachievable region* as the set of pairs (R_0, P_{out}) for which it is impossible to find reliable codes. The boundary of this region quantifies the optimum tradeoff between P_{out} and R_0 and can be approached by utilizing the optimum beam widths and input distribution. Note that, the optimum beamwidth, w_o^{opt}, and input distribution, are in general different for each point on the optimum tradeoff curve between P_{out} and R_0. In the following section examples of the application of this information theory based criterion to FSO channel design are presented for different weather conditions.

After finding the optimal tradeoff between P_{out} and R_0 for a given weather condition, the communication link is designed such that it meets a certain minimum requirement in terms of P_{out}, i.e., link reliability. For a given P_{out} the maximum achievable rate R_0 is obtained from the optimal tradeoff curve and the system is designed to communicate at this rate. In order to increase the average rate, rate adaptation at the transmitter can be employed. Notice that rate adaptation on the order of the coherence time, i.e., hundreds of millisecond, increases system complexity due to the need for extensive feedback. For practical systems, rate adaptation can be performed for each weather conditions which occurs on the order of few hours.

6.4 Weather and System Parameters

As discussed in Chapter 2, the effect of weather conditions on optical link performance is characterized by two parameters, the refractive-index structure parameter C_n^2 and the attenuation coefficient μ. In the following analysis the outage capacity is optimized considering both clear and light fog weather conditions. The parameters for these two weather conditions are presented in Table 6.1 [17,124]. These two weather conditions are selected since they correspond to strong and weak turbulence regimes respectively. Note that, the attenuation coefficient can also be computed mathematically through empirical formulas that are expressed in terms of visibility [17]. These empirical formulas provide a close agreement with the practical measurements over a wide range of weather conditions.

The physical parameters of the FSO link under investigation are presented in Table

Table 6.1: Weather parameters

Condition	$C_n^2 \times 10^{-14}$ $\mathrm{m}^{-2/3}$	σ_R^2	Attenuation Coefficient μ km^{-1}	h_ℓ	Attenuation dB/km
Clear	50	10	0.4	0.675	1.7
Light fog	1	0.2	3.5	0.03	15

6.2 [106,125]. Propagation distance of $z = 1$ km and wavelength $\lambda = 1550$ nm are considered. Typical values for receiver sensitivity S_v and noise standard deviation σ taken from a commercial transimpedance amplifier [126]. The transmitter and receiver optics efficiencies $\eta_T = 0.8$ and $\eta_R = 0.8$ are scaling factors for the received optical power. The jitter angle standard deviation at the transmitter is set to $\sigma_{\theta_s} = 0.4$ mrad resulting in a jitter standard deviation at the receiver of $\sigma_s \approx \sigma_{\theta_s} z = 40$ cm. A Gaussian-beam wave is considered where the beam waist at the transmitter varies from $w_o = 1$ to 3 cm with a step size $\Delta w_o = 0.1$ cm forming the set $\mathcal{W} = \{1, 1.1, \ldots, 3\}$ cm. The optimum beamwidth w_o^{opt} is found for each case through an exhaustive search over the discrete set $\mathcal{W}$. The nominal beam waist is set to $w_o = 2$ cm. A circular receiver of radius $a = 5$ cm is deployed which represent a typical commercial receiver (SONAbeam 1250-E) [13].

The Gamma-Gamma model is utilized to analyze the system under clear weather condition. The parameters α and β are computed using (2.5), (2.6) and (2.7) with the parameters given in Table 6.2. The scintillation index is computed using (2.8). The log-normal distribution is utilized for light fog weather condition (weak turbulence $\sigma_{\mathrm{R}}^2 < 0.3$) where the variance σ_χ^2 is computed from the scintillation index expression through (2.3). In all cases aperture averaging effect is considered in the analysis. Considering the values in Table 6.2, it is noticed that the scintillation index relative deviation $\Delta\sigma_{I_{\mathrm{a}}}^2(r, z)$, given by (2.10), changes within 1% at the extreme misalignment

Table 6.2: System Parameters

Parameter	Symbol	Value
Transmitted optical power	P	40 mW (16 dBm)
Combined Tx/Rx optics efficiency	η	0.64
Responsivity	R_v	0.5 A/W
Wavelength	λ	1550 nm
Noise standard deviation (1 Gbps)	σ	5×10^{-7} A
Receiver radius	a	5 cm
Link distance	z	1000 m
Beam waist radius (Transmitter)	w_o	1-3 cm
Beam waist radius increment	Δw_o	0.1 cm
Phase front radius	F_o	-10 m
Jitter angle standard deviation	σ_θ	0.4 mrad
Set of permissible beamwidths	$\mathcal{W}$	$\{1, 1.1, \ldots, 3\}$ cm

deviation point (radial displacement $r \cong 3\sigma_s$) compared to the beam center point ($r = 0$). Based on this results, the intensity variance is considered fixed over the beamwidth and set equal to the variance at the beam center. After establishing the appropriate channel statistical model that describes the intensity fluctuations at the receiver, the outage capacity is computed.

6.5 Uniform Signaling and Outage Capacity

In this section, the outage capacity of FSO systems using uniform OOK is optimized over beamwidth selection following the design approach presented in Section 6.3. Channel capacity in this section refers to the the mutual information when the input distribution has two equiprobable mass points. However, in the subsequent sections comparisons between different signaling schemes are conducted.

6.5.1 Probability of Outage

For a given average optical power, P, the beamwidth w_o is chosen to minimize P_{out} when the transmitter is constrained to have a fixed code rate R_0. Qualitatively, beamwidth optimization balances the impact of atmospheric and misalignment fading on the probability of outage. Widening the beam mitigates pointing errors at the expense of a received power reduction. However, narrowing the beam limits the geometric loss but increases the impact of misalignment.

The probability of outage versus P for clear weather is shown in Fig. 6.1 for a code rate $R_0 = 0.5$ (bits/channel use). The Gamma-Gamma fading distribution is utilized to compute the outage probability (6.2) via numerical integration. For a given P, the optimum beamwidth, w_o^{opt}, is selected to minimize $P_{\text{out}}(0.5; w_o)$. Figure 6.2 presents the optimum beamwidth w_o^{opt} versus average power. Notice that the optimum beamwidth increases as P increases. Intuitively, in this strong turbulence regime the

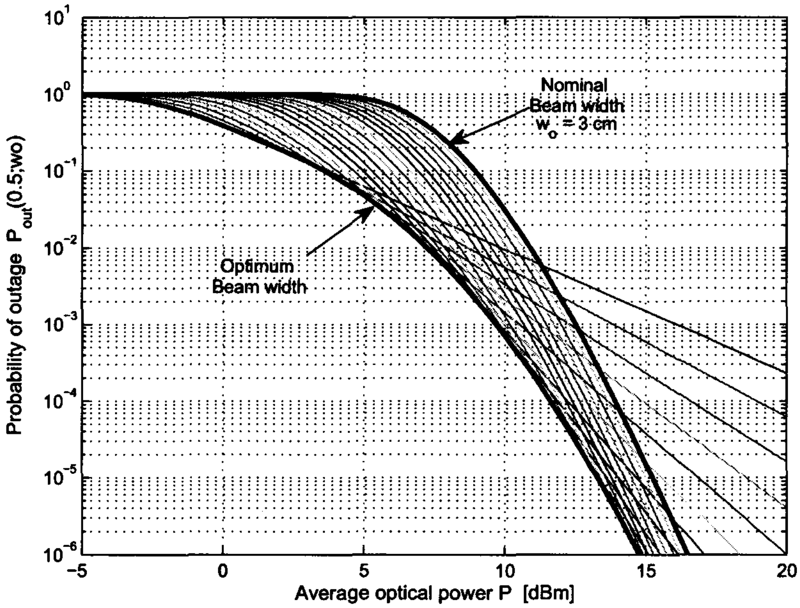

Figure 6.1: P_{out} versus P for clear weather and $R_0 = 0.5$ bits/ch. use.

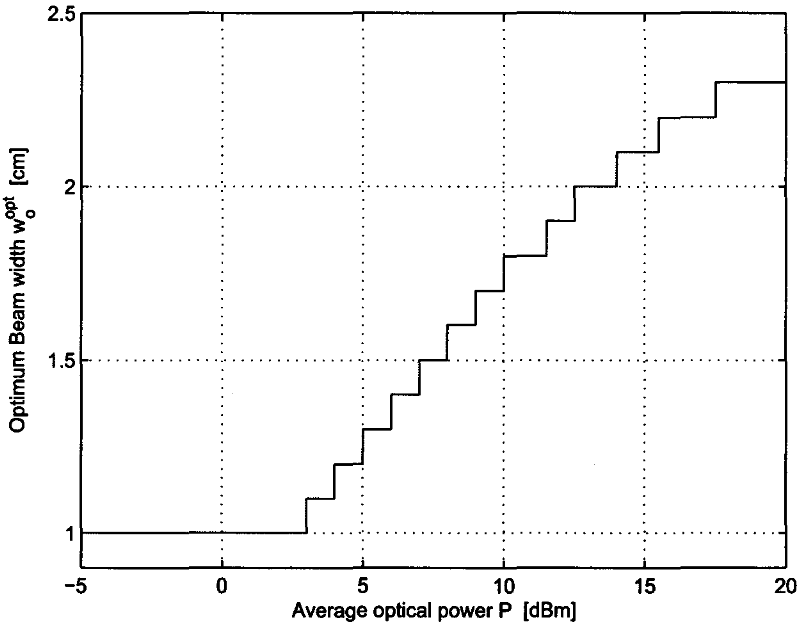

Figure 6.2: Beamwidth versus P for clear weather and $R_0 = 0.5$ bits/ch. use.

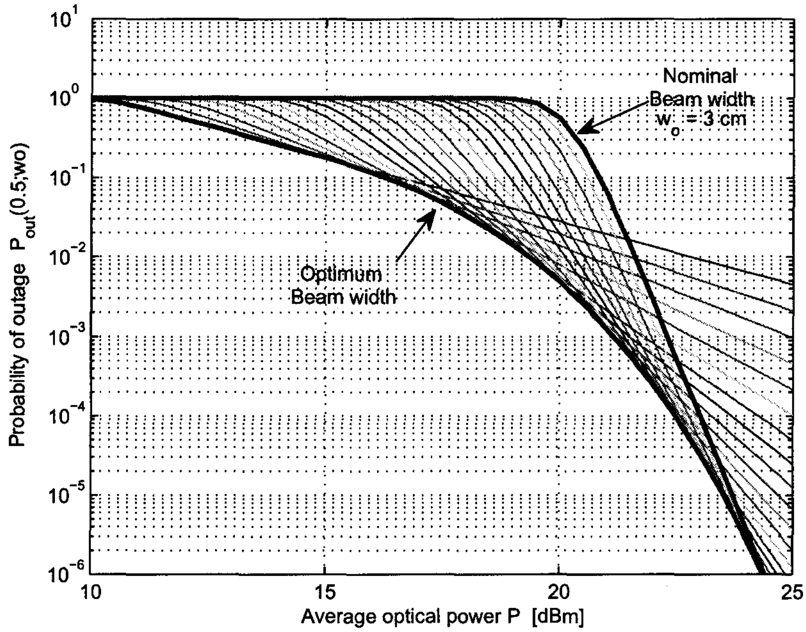

Figure 6.3: P_{out} versus P for light fog and $R_0 = 0.5$ bits/ch. use.

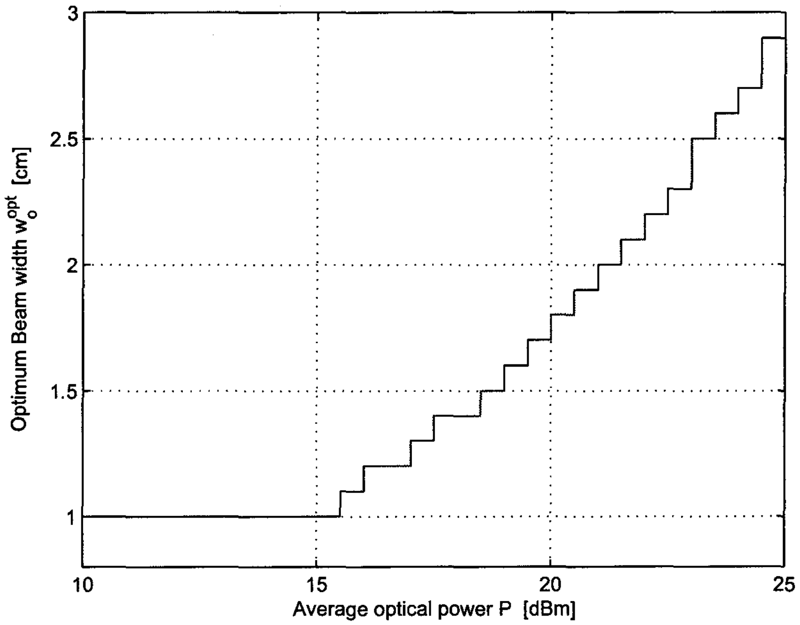

Figure 6.4: Beamwidth versus P for light fog and $R_0 = 0.5$ bits/ch. use.

increase in the optical power is utilized to combat both atmospheric and misalignment fading. At $P_{\text{out}} = 10^{-4}$, a gain of approximately 2 dB in the optical power is realized by optimizing the beamwidth. Furthermore, for a given R_0 a significant reduction in the outage probability is achieved using beamwidth optimization.

The probability of outage for the light fog weather condition is presented in Fig. 6.3 with $R_0 = 0.5$ (bits/channel use). From the figure, at $P_{\text{out}} = 10^{-2}$ a gain of approximately 2 dB is obtained. The behavior of this system is in contrast to the strong fading case discussed earlier. The optimum beamwidth changes rapidly with P as shown in Fig. 6.4 where the corresponding values for the optimum beamwidths w_o^{opt} are presented. This increased sensitivity to misalignment fading can be justified due to the weak fading and high attenuation in this channel. Qualitatively, increases in P are traded-off for increases in the beamwidth to mitigate the impact of pointing errors. Transmitters designed for these channels need to have accurate control of their beamwidths as significant gains can be made with the proper selection of w_o.

6.5.2 Probability of Outage and Achievable Rates

In this section, the tradeoff between the outage probability, P_{out}, and the maximum achievable rate is analyzed for light fog weather condition using the optimum and the nominal beamwidths. Figure 6.5 illustrates this tradeoff when the optimum beamwidth and the fixed nominal beamwidth, $w_o = 2$ cm, are employed. Note that the value of w_o^{opt} varies for each point on the curve. As discussed in Section 6.3, not all pairs (R_0, P_{out}) are achievable, resulting in an unachievable region. For pairs in the unachievable region, reliable communication is not possible. Thus, the $P_{\text{out}}(R_0; w_o^{\text{opt}})$ curve is the optimum tradeoff between outage probability and achievable rate when OOK is utilized for light fog weather condition. Note that the term "optimum tradeoff" here is associated with the definition of w_o^{opt} given in (6.3).

It is clear from Fig. 6.5 that for a given probability of outage there is a significant gain in the achievable rate when utilizing the optimum beam over the nominal beam. For example, if the system is designed to meet $P_{\text{out}} = 10^{-1}$ then the maximum code rate that can be reliably transmitted over this channel using the nominal beamwidth is $R_0 = 0.24$ bits/channel use while when utilizing the optimum beam is $R_0 = 0.44$, with an increase of 83% in the achievable rate.

Although beamwidth optimization increases R_0, these achievable rates represent the maximum rates for which reliable communications is possible. Error control codes must be applied to approach these R_0 values with practical complexity. Well-known error control codes with k data bits per codeword and block length n are applied to the channel and their performances are shown in Fig. 6.5. For the simulations, an outage is defined as the event that the decoded BER is greater than 10^{-6}. The SNR corresponding to BER= 10^{-6} is found for each code through simulation and, via (6.1), the corresponding h_0 is computed. For the code rate $R_0 = k/n$ substituting h_0 and the w_o^{opt} into (6.2) results in the corresponding probability of outage. At low rates, hardware based Turbo codes for space communications [127] as well as low-density parity-check (LDPC) [128] codes with large n approach the optimal $P_{\text{out}}(R_0; w_o^{\text{opt}})$. At higher rates, Reed-Solomon [129] and low-complexity LDPC codes for fiber optical applications [130–132] can also be designed to operate close to the $P_{\text{out}}(R_0; w_o^{\text{opt}})$ curve. Of notable interest is the performance using a hardware implemented rate-$\frac{1}{2}$ LDPC code [133]. From Fig. 6.5, the code achieves a $P_{\text{out}} = 1.4 \times 10^{-1}$ while at this probability of outage value the maximum rate is $R_0 = 0.58$ bits/channel use. Thus, this practical code can realize approximately 86% of the maximum rate. An important conclusion from this analysis is that the codeword length can greatly affect the achievable outage capacity. As an example, the LDPC^7 with $k = 1024$ and rate 2/3 achieves $P_{\text{out}} = 0.3$ where the optimum is $P_{\text{out}} = 0.2$ while the LDPC^5 with $k = 190$ and rate 0.75 achieves $P_{\text{out}} = 0.5$ where the optimum is $P_{\text{out}} = 0.22$. In the following section it will be shown that these outage probabilities can be further minimized

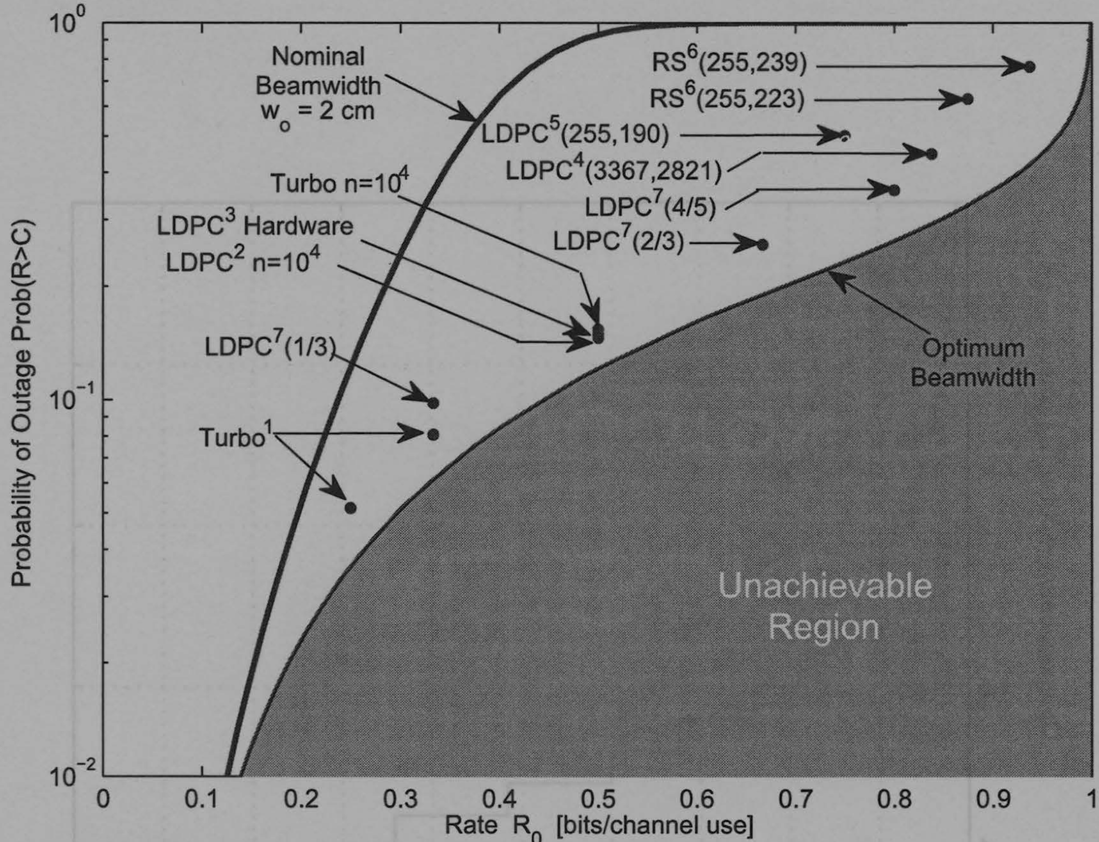

Figure 6.5: Probability of outage versus achievable rate for nominal ($w_o = 2$ cm) and optimum beamwidths for light fog using uniform OOK. A variety of error control codes with rate k/n are applied to this channel where k bits are sent per codeword of length n symbols and the performance presented at BER$=10^{-6}$. Hardware implemented Turbo^1 codes with $R_0 = \{1/4, 1/3\}$ and $k = 8920$ [126]. LDPC^2 and Turbo^2 with rate 1/2 and $n = 10^4$ [127]. Hardware implementation for LDPC^3 with $R_0 = 1/2$ and $k = 4096$ [132]. LDPC^4 [129] and LDPC^5 of code rate 0.75 [130]. High rate Reed-Solomon codes RS^6 with $R_0 = 0.874$ and 0.937 [128]. LDPC^7 with $k = 1024$ [131].

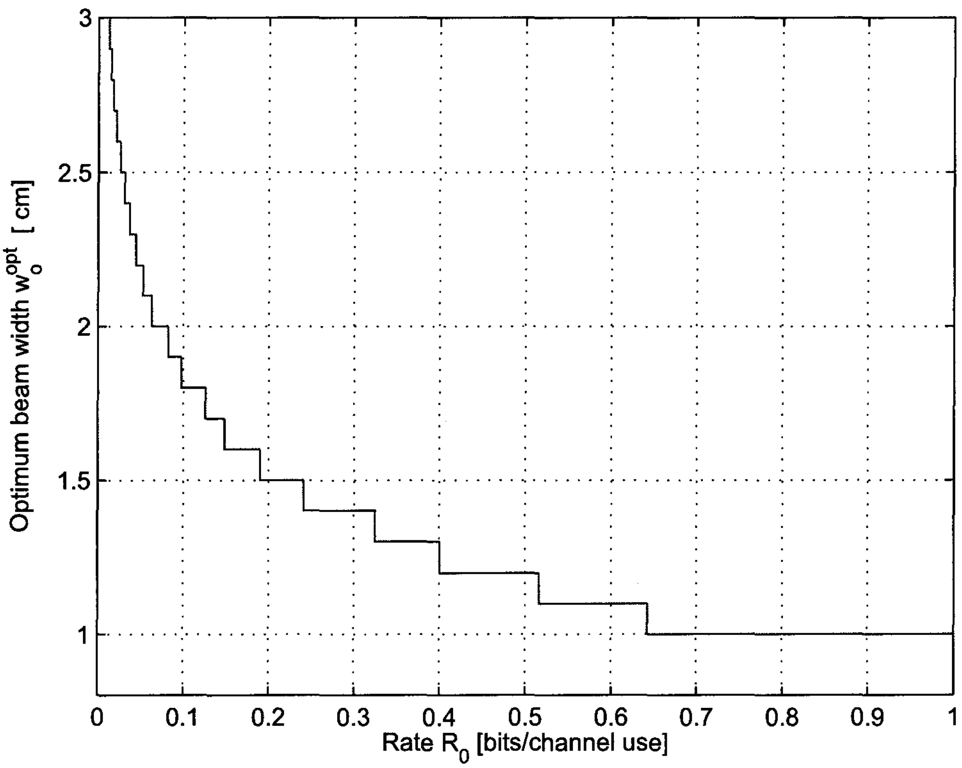

Figure 6.6: Optimum beamwidth, w_o^{opt}, versus rate, R_0, for light fog weather condition where w_o varies from 1 to 3 cm.

when non-uniform distributions are utilized. As shown in Fig. 6.5, significant gains in achievable rate are available by beam optimization and the optimal tradeoff between P_{out} and R_0 derived here can be used as a design guide when selecting code rates in practical FSO channels.

Also the optimum beamwidth versus rate is presented in Fig. 6.6. As shown, when R_0 increases a narrow beamwidth is utilized. Notice that this tradeoff is analyzed under fixed optical power P given in Table 6.2. Thus to increase the rate R_0 an increase in the received power is required. This can be achieved using a narrow beamwidth. On the other hand, narrowing the beamwidth increases the impact of misalignment and hence a higher probability of outage is obtained.

6.6 Non-Uniform Signaling and Outage Capacity

Since the non-uniform distributions developed in Chapters 3 and 4 can achieve much higher data rates compared to uniform distributions, they are considered in this section where outage capacity is optimized over input distribution and beamwidth selection. We demonstrate that non-uniform signaling significantly increases the outage capacity compare to the uniform signaling.

6.6.1 Average Power Constraint

The outage capacity, i.e., the pair (R_0, P_{out}), under an average power constraint is analyzed using the non-uniform distributions developed in Chapter 3. The upper and lower bounds developed on the channel capacity are utilized to characterize the outage capacity boundary using the criteria described in Section 6.3. The parameters presented in Table 6.2 are considered in the analysis. Figure 6.7 shows the tradeoff between the rate, R_0, and the probability of outage, P_{out}, for light fog weather condition. Bounds on the outage probability are presented by using C_{L} (3.7) and C_{U}

(3.18) developed in Chapter 3. Note, the lower bound on P_{out} is achievable when the input distribution follows $q_\ell^*(x)$ in (3.6) where for a given P and σ, the mass point spacing is optimized to maximize C_{L} for each channel state. The uncertainty region presents a collection of pairs (R_0, P_{out}) where it is not known whether they are achievable or not. Furthermore, any pair (R_0, P_{out}) in the unachievable region can not be realized in practice. For comparison, uniform 2-PAM signaling is considered and the resulting maximum achievable rate is presented. In addition, for practical implementation considerations, the performance of the quantized-levels distributions with $M = 2$ symbols and different permissible quantization-levels, $2^N = 4$ and 32, are presented. As shown significant gain in rate and reduction in probability of outage are noticed when non-uniform signaling is employed compared to uniform 2-PAM signaling. In addition, the gain increases when the number of permissible quantization levels increases

As shown in Fig. 6.7, at $P_{\text{out}} = 10^{-3}$ uniform 2-PAM signaling achieves approximately a rate of 0.05 bits/channel use while employing the non-uniform input distribution $q_\ell^*(x)$ in (3.6) a rate of approximately 0.38 bits/channel use can be achieved. Clearly a significant gain in rate is obtained when the non-uniform signaling is considered. The performance of the quantized-levels distributions are presented for comparisons. The input distribution $\tilde{q}_{\ell'}^*(x)$ in (5.2) with M=2 symbols and $2^N = 4$ and 32 levels are considered where rates of approximately 0.17 and 0.36 bits/channel use are achieved respectively. Although rate degradation is noticed when the number of quantization levels is reduced, the implementation becomes simpler.

Similarly, at $R_0 = 0.2$ bits/channel use an order of magnitude reduction in the outage probability is obtained when the non-uniform is compared to the uniform 2-PAM distributions. Notice that the outage probability using non-uniform quantized-level distributions with 4 and 32 quantization levels is the same in the range $0.69 \leq R_0 \leq 0.75$. This results can be explained by finding the input distributions over this

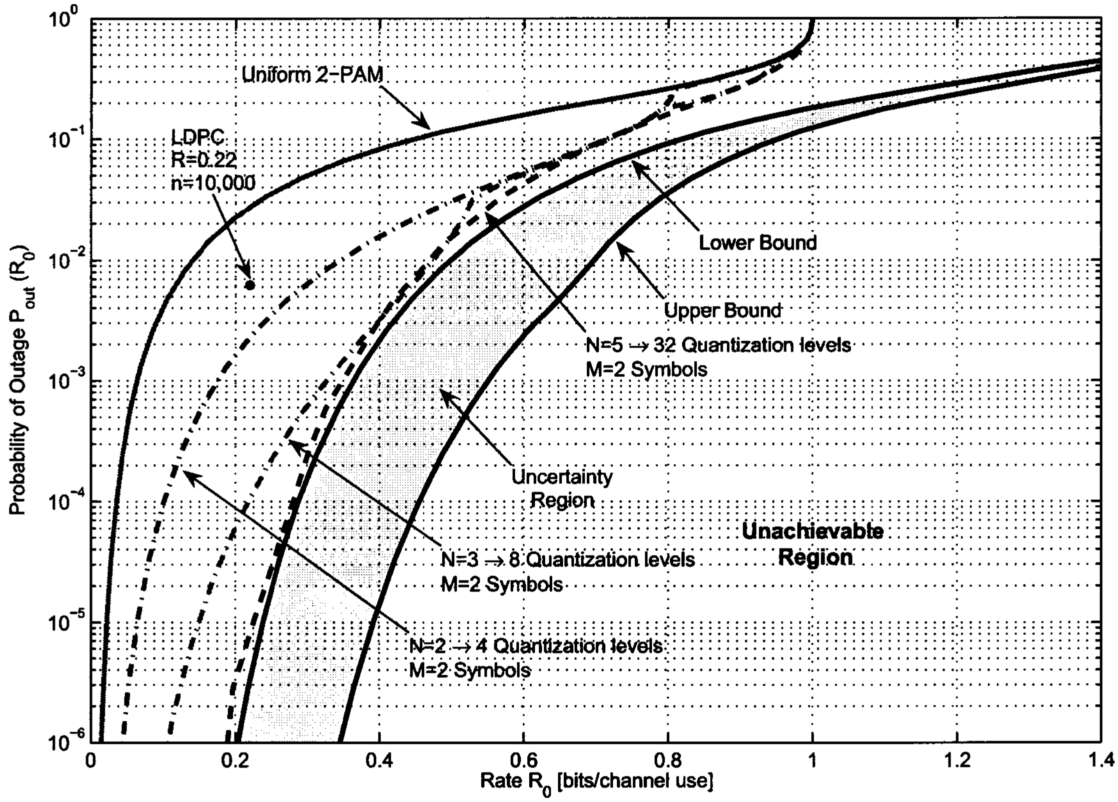

Figure 6.7: Average power constraint. Probability of outage P_{out} versus rate R_0 in bits/channel use for light fog weather condition. The non-uniform distribution with $M = 2$ mass points and $2^N = 4$ and 32 quantization levels are presented in addition to uniform 2-PAM. Optimum beamwidth is considered in the analysis.

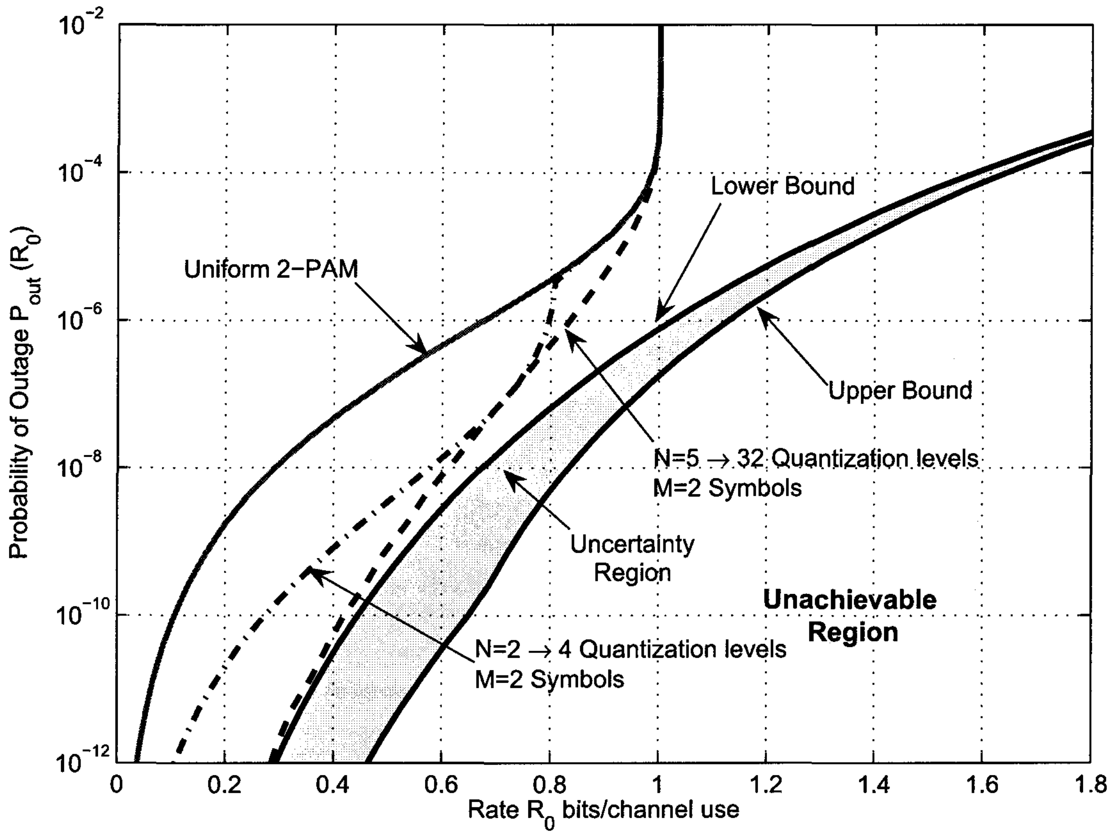

Figure 6.8: Average power constraint. Probability of outage P_{out} versus rate R_0 in bits/channel use for clear weather condition. The non-uniform distribution with $M = 2$ mass points and $2^N = 4$ and 32 quantization levels are presented in addition to uniform 2-PAM. Optimum beamwidth is considered in the analysis.

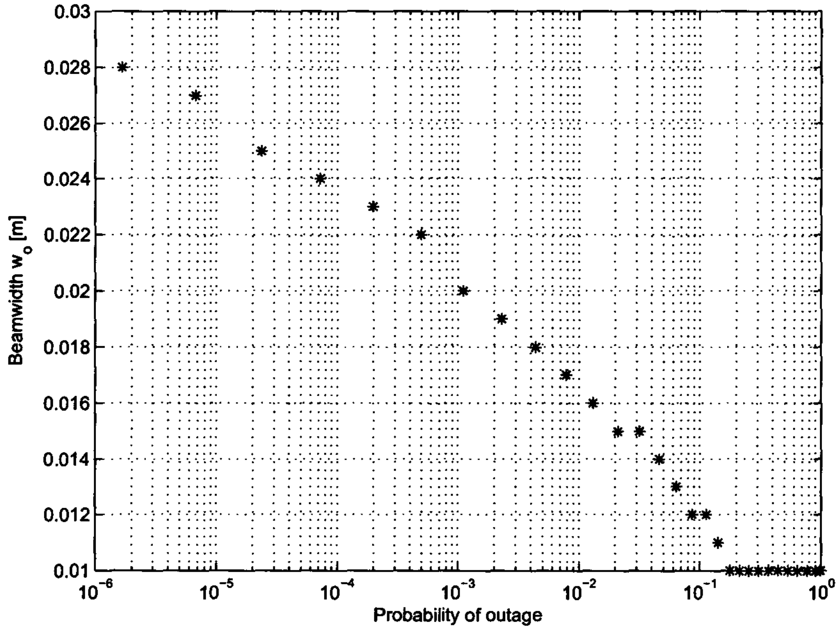

Figure 6.9: Average power constraint. Beamwidth versus P_{out} for light fog weather.

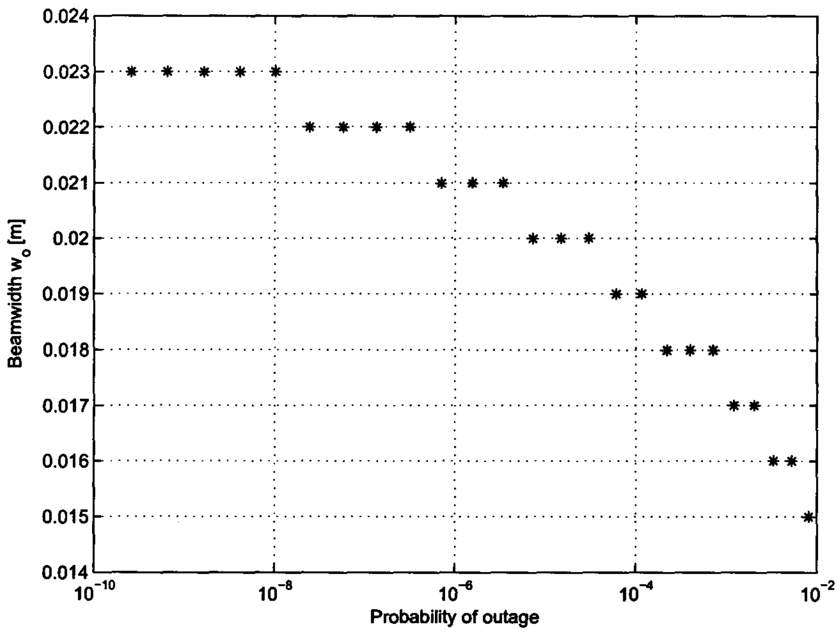

Figure 6.10: Average power constraint. Beamwidth versus P_{out} for clear weather.

range which are given by $\{\frac{3}{4}, \frac{1}{4}\}$ and $\{\frac{24}{32}, \frac{8}{32}\}$ respectively and hence the performance coincide over the given range of data rate.

The low density parity check (LDPC) codes and the non-uniform distribution presented in Fig. 5.10 with codeword length $n = 10,000$ are considered and their performances is shown in Fig. 6.5. For the simulations, an outage is defined as the event that the decoded BER is greater than 10^{-6}. The SNR corresponding to this BER is found from Fig. 5.10 and, via (6.1), the corresponding h_0 is computed. Substituting h_0 and the w_o^{opt} into (6.2) results in the corresponding probability of outage. Compared to the uniform signaling and at $P_{\text{out}} = 6 \times 10^{-3}$, approximately double the rate can be achieved. Furthermore, a reduction in probability of outage is noticed at $R_0 = 0.22$ bits/channel use.

Figure 6.8 presents the outage capacity, i.e., the pair (R_0, P_{out}), for the clear weather conditions. As shown similar gain in rate and reduction in outage probability are noticed between the non-uniform and the uniform 2-PAM. Note that when $R_0 = 1$ bits/channel use, uncoded transmission can be utilized with acceptable performance. Furthermore, at $R_0 = 1$ the non-uniform signaling with $M > 2$ symbols can achieve $P_{\text{out}} = 10^{-6}$ as shown from the lower bound. This performance improvement is achieved at the expenses of a higher complexity in system implementation.

The corresponding optimum beamwidth, w_o^{opt} versus probability of outage for both light fog and clear weather conditions is presented in Fig. 6.9 and Fig. 6.10 respectively. A common conclusion is that as the beamwidth decreases higher power is obtained within the beam and hence higher rates, however, with the existence of misalignment fading higher probability of outage is noticed.

6.6.2 Peak and Average Power Constraints

In this section, the outage capacity under both peak and average power constraints is analyzed. We consider the light fog weather condition with the parameters presented in Table 6.1. The system parameters are set to the values given in Table 6.2 and a peak-to-average power ratio of $\rho = 4$ is considered. The outage capacity is analyzed using the capacity-achieving, the maxentropic, and the uniform 2-PAM input distributions.

The capacity-achieving input distribution is obtained by solving the optimization problem (4.2) numerically. Then the outage capacity is computed where for a given rate, R_0, the beamwidth is optimized to minimize the associated probability of outage. The pairs (R_0, P_{out}) form the boundary of the unachievable region in the P_{out} versus R_0 domain. The outage capacity using the input distribution $\bar{q}_X^*(x; K)$ (4.6) is also computed and shown in Fig. 4.3. For comparison the uniform 2-PAM input distribution is considered such that both the peak, $X \leq A$, and the average optical power, $\mathbb{E}\{X\} \leq P$, constraints are satisfied where $\rho = A/P = 4$. As a result, the uniform input distribution is given by $q(x) = 0.5\,\delta(x) + 0.5\,\delta(x - 2P)$.

Probability of outage $P_{\text{out}}(R_0)$ versus rate R_0 is shown in Fig. 6.11. The grey area represents the unachievable region, that is any pair (P_{out}, R_0) in this region cannot be realized with any input distribution satisfying the peak and the average power constraints. The outage capacity boundary is computed using the capacity-achieving distribution. The outage capacity using the maxentropic distribution is also shown. Notice that the performance with $\bar{q}_X(x; 1) = 0.75\,\delta(x) + 0.25\,\delta(x - A)$ coincides with the capacity boundary when $0 < R_0 < 0.75$. When the rate increases to $0.75 < R_0 < 1.15$, the maxentropic distribution with three mass points has a higher outage capacity compared to all other distributions. As shown its performance is significantly close to the unachievable region boundary. When $1.15 < R_0 < 1.4$, the maxentropic distribution with four mass points is considered. Compared to the uniform 2-PAM distribution for a given rate $R_0 < 1$, an order of magnitude reduction in the outage probability is noticed when the non-uniform distribution is utilized. As an example, an FSO link operating at rate $R_0 = 0.5$ (bits/channel use) achieves $P_{\text{out}} = 1.5 \times 10^{-1}$ when the uniform distribution is utilized while it achieves $P_{\text{out}} = 3 \times 10^{-2}$ when the non-uniform distribution with two mass points is utilized. Notice that the implementation of the non-uniform distribution given above can be realized using the MLC/MSD system discussed in Chapter 5 with only two encoders. As a result, significant reduction in probability of outage can be achieved with a moderate increase in system complexity compared to signaling with uniform distribution. Similar gain can be achieved in terms of rate, as an example, at $P_{\text{out}} = 10^{-2}$ the non-uniform distribution achieves $R_0 = 0.35$ bits/channel use while the uniform distribution achieves $R_0 = 0.15$ (bits/channel use), i.e., more than double the rate is achieved in this case.

In addition, the LDPC codes utilized in Fig. 5.15 are considered to evaluate the performance of the fading FSO channels. Figure 6.11 shows that practical LDPC codes with combined rate $R = 0.17$ and codeword length $n = 10,000$ using a non-uniform input distribution outperform uniform distributions from both rate and reliability perspectives. For the simulations, an outage is defined as the event that the decoded BER is greater than 10^{-5}. The SNR corresponding to this BER is found from Fig. 5.15 and, via (6.1), the corresponding h_0 is computed. Substituting h_0 and the w_o^{opt} into (6.2) results in the corresponding probability of outage. To quantify, in Fig. 6.11 at $R = 0.17$, bits/channel use, the LDPC codes with non-uniform distribution can achieve $P_{\text{out}} = 5 \times 10^{-3}$ while the uniform distribution can achieve $P_{\text{out}} = 2 \times 10^{-2}$ that is approximately an order of magnitude reduction in outage probability.

The corresponding optimum beamwidth, w_o^{opt} versus probability of outage for light fog weather condition is presented in Fig. 6.12. As concluded in previous Sections, higher data rates can be achieved with narrow beamwidth, however, higher probability of outage is obtained since the impact of the misalignment fading is increased.

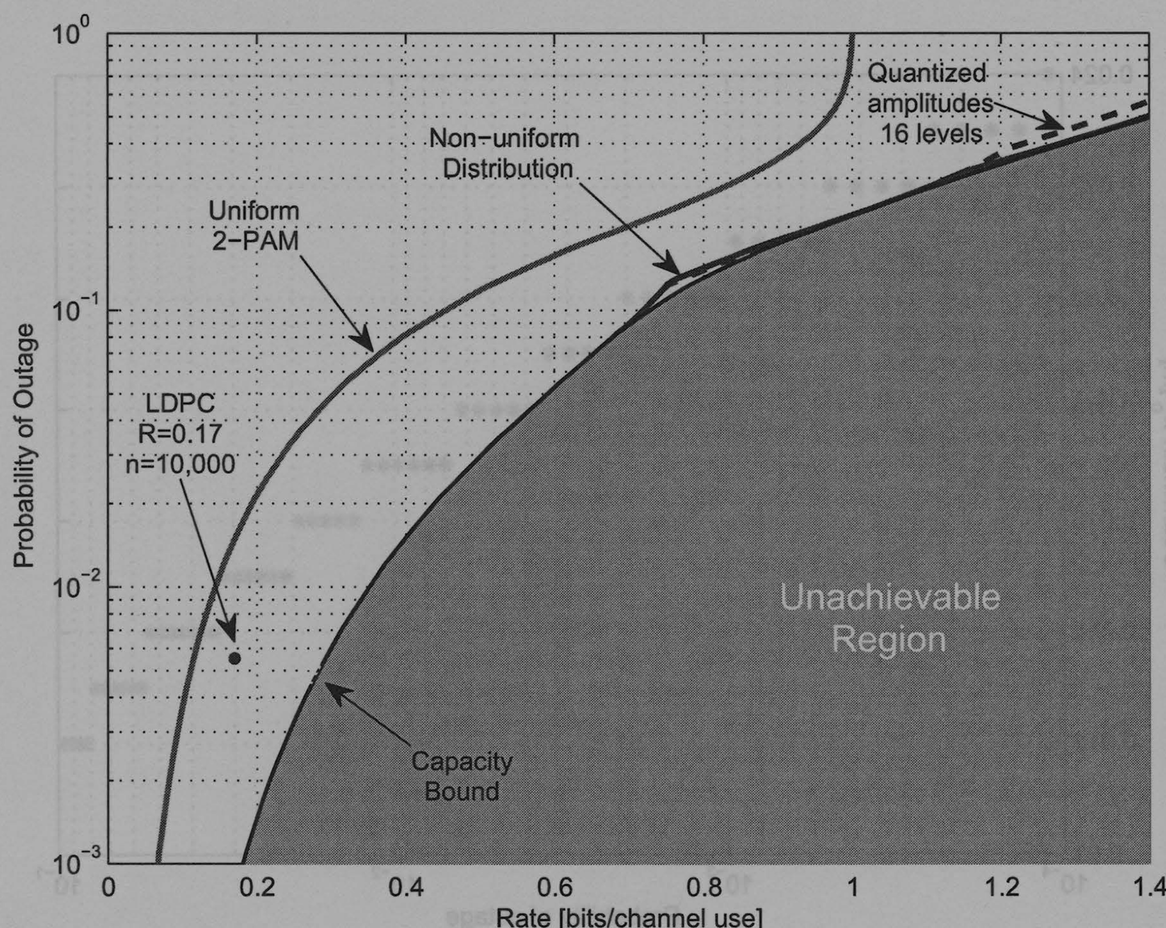

Figure 6.11: Peak and average power constraints with $\rho = 4$. Probability of outage versus rate, R_0, for uniform 2-PAM distribution, non-uniform $\bar{q}^*(x; \bar{K})$ (4.6), quantized distribution $\tilde{q}^*(x; \tilde{K})$ (5.5), and the capacity bounds for light fog weather condition.

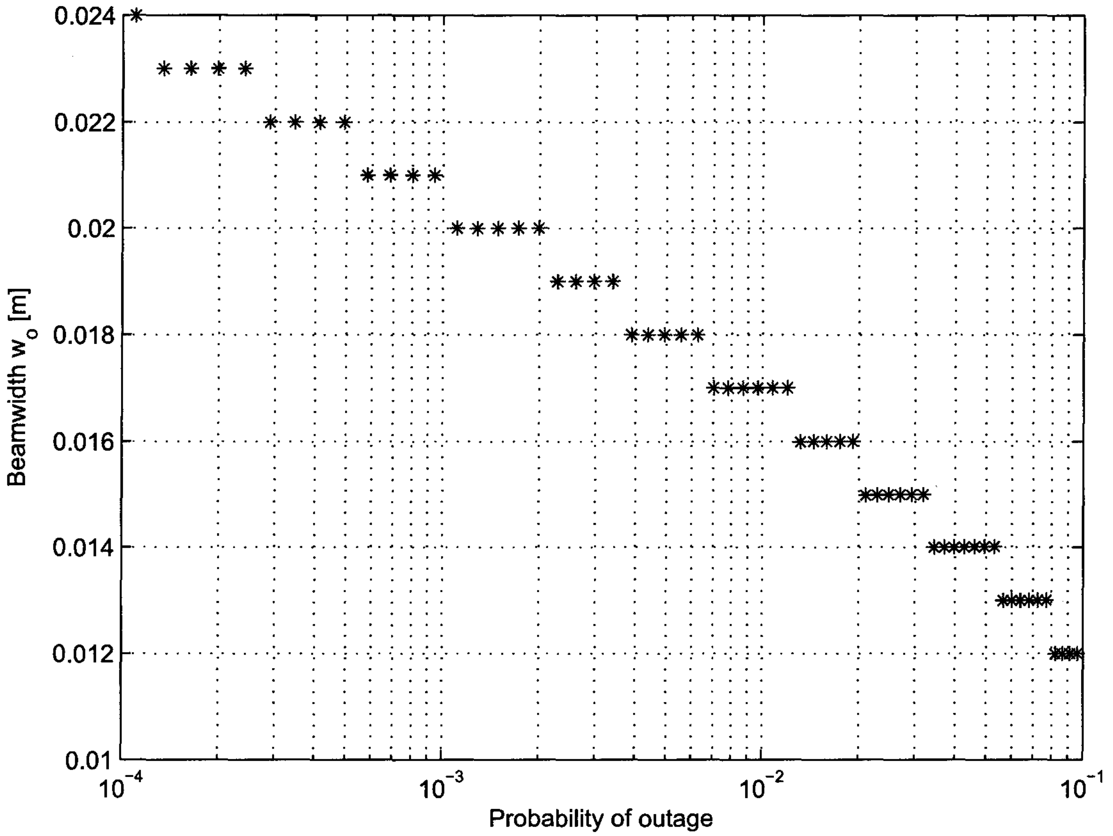

Figure 6.12: Peak and average power constraints with $\rho = 4$. Beamwidth versus P_{out} for light fog weather condition.

6.7 Conclusion

The design of FSO links corrupted by atmospheric turbulence and pointing errors from an information theory perspective is analyzed. The developed statistical channel model in Chapter 2 is utilized to derive fundamental limits on the outage probability and the achievable rates for FSO channels. In particular, the outage capacity is investigated where the outage probability is minimized over both input distribution and beamwidth selection. Given uniform OOK signaling, it is shown that the optimum beamwidth achieves higher outage capacity compared to the nominal beamwidth. This conclusion applies for both weak and strong turbulence regimes. Furthermore, for a given average power the optimum beamwidth achieves higher rates which is shown to approach 80% at $P_{\text{out}} = 10^{-1}$. Error correcting codes are then applied, and previously reported hardware implementations of LDPC code can achieve 86% of the maximum rate.

A framework to design the outage capacity for FSO systems under non-uniform signaling is presented. A significant increase in the rate is noticed when employing the non-uniform input signaling compared to the uniform 2-PAM for different weather conditions. In addition, for a given rate, an order of magnitude reduction in the probability of outage is noticed at low SNR where most FSO systems operate. For practical implementation, non-uniform distributions with quantized-level probabilities are shown to achieve most of the outage capacity gain.

It has been demonstrated that beamwidth optimization leads to significant increases in the channel capacity subject to outage. Furthermore, most of the achievable rate can be realized using realistic and practical error correcting codes. Thus, this work provides a design guide for FSO communication systems.

Chapter 7

Conclusions and Future Directions

7.1 Conclusion

This thesis presents techniques to improve the performance of wireless optical intensity channels. Four major contributions are presented in the following areas: 1) statistical channel model; 2) channel capacity; 3) signaling design and implementation algorithm; and 4) FSO system optimization with joint rate and beamwidth design.

Statistical models for FSO channels corrupted by atmospheric turbulence and misalignment fading are presented. Unlike previous models where the detector size is considered to be negligible with respect to the beam footprint at the receiver, the detector size is taken into account in the developed models as well as transmitter beamwidth. These models are used to accurately design FSO systems and provide fundamental limits on the system performance.

To investigate the ultimate performance that can be achieved from FSO channels, it is essential to study the channel capacity. The capacity of optical PAM intensity channels under non-negativity and average power constraints is investigated where tight lower and upper bounds at low and high SNR regime are developed. Analytical expressions for the upper bound is derived with numerical evaluation for the lower bound. Non-uniform signaling is also proposed as a capacity-approaching distribution. Compared to uniform signaling, a significant gain in rate is noticed over a range of SNRs especially at low SNR. Since a majority of FSO systems operate at relatively low SNRs, the tightness of the derived bounds at low SNRs provides a useful benchmark for FSO communication systems design.

The channel capacity under peak power constraint in addition to the non-negativity and average power constraints is also analyzed. The capacity-achieving input distribution is found through numerical solution for a non-linear optimization problem. A closed form for a capacity-approaching distribution based on entropy maximization is presented. In addition to the substantial complexity reduction in generating this distribution compared to the optimum distribution, a negligible gap between the resulting mutual information and the channel capacity is noticed. Unlike the capacity-achieving distribution where for each SNR value a different input distribution is obtained, the proposed input distribution is fixed over a range of SNRs. In addition, for a given SNR, the number of probability mass points in the developed distribution is less than the capacity-achieving distribution for the SNR range considered, reducing the implementation complexity. Finally, the derived capacity-approaching distributions serve as a useful tool not only to bound the channel capacity but to guide the development of channel coding and signaling schemes for optical wireless channels.

An algorithm to induce a non-uniform distribution is applied from previous work providing a guideline on system implementation. Multi-level coding followed by a deterministic mapper at the transmitter and multi-stage decoding at the receiver are utilized. Numerical simulations were undertaken to demonstrate that good codes with finite length using non-uniform signaling can be found to approach the channel capacity. Also it is shown that this setup outperforms capacity-achieving codes employed with uniform input distribution.

Finally, the outage capacity is analyzed over the slow-fading FSO channels where the rate and the associated outage probability are derived for both weak and strong turbulence regimes in the presence of misalignment fading. It has been demonstrated that beamwidth optimization can significantly increase the channel capacity subject to outage. Most of the achievable rates can be realized using realistic and practical error correcting codes. In addition, it is shown that, non-uniform distribution can achieve higher rate and an order of magnitude reduction in outage probability compared to the widely used uniform distribution. Thus, this work presents a formal method for joint design of beamwidth, signaling and code rate for FSO communication systems.

7.2 Future Directions

The FSO channel model presented in Chapter 2 is valid when the intensity variance seen by the detector at the maximum misalignment displacement is negligibly deviated from the variance at the beam centre. However, extensive investigation is required to study how the intensity variation within the received beam can affect the system performance. Although a wave optics based approach is utilized to study this effect numerically [134], a mathematically tractable analysis is not available. This point will lead to a better understand for FSO system performance under different misalignment conditions. In particular, in mobile communication, e.g. unmanned aerial vehicle (UAV), where misalignment can severely deteriorate the link performance.

In Chapter 5, an algorithm using MLC/Mapper/MSD to realize the non-uniform distributions developed in Chapters 3 and 4 is presented. Building this system to operate at a fixed transmission rate is simple where the sub-channels encoders/decoders can be realized easily. One of the conventional strategies to increase the system throughput is to adapt the transmission rate, assuming channel state information is available at the transmitter. In this case it is required to design encoders/decoders to operate at different rates. One of the solution is to consider variable rate code for each encoder. However, system complexity will be increased. Thus, investigation for the complexity-performance tradeoff is required to decide whether rate adaptation or fixed rate strategy is better for FSO systems.

In Chapter 6 FSO performance is optimized over beamwidth selection. This step requires an adaptive component at the transmitter and hence higher complexity. It would be of interest to study the performance when a fixed beamwidth is assigned over a range, i.e., group, of operating conditions. As an example, the outage capacity was analyzed for a discrete rate in the range $0 < R_0 < 1$, this range can be divided into a subset ranges where the performance of the FSO system with a fixed beamwidth in each range can be optimized. In this case a lower complexity will be achieved. However, performance degradation will be also noticed. System design can optimally balance between complexity and performance degradation.

As discussed, the performance of the FSO links is a weather dependent where the main severe impact is the attenuation due to fog. This impairment limits the link range and may lead to outage in case of long range links. On the other hand, the main concern in radio-frequency RF communications is the rain. As a promising direction to overcome this problem is to consider a hybrid RF/FSO link which can perform well over different weather conditions [135–137]. However, in point-to-point communication switching between these technologies is not simple where different strategies can be considered. In addition, hybrid RF/FSO links can be deployed in wide area network. However, terminal position allocation is a difficult optimization problem [138].

While in this thesis a single transmitter and a single receiver is considered, multiple-input multiple-output (MIMO) can be deployed over FSO channels to combat the channel fading. The MIMO technique has been widely utilized in RF systems and significant improvements in system performance have been achieved. In this technique, the degrees of freedom provided by the MIMO structure can be utilized efficiently to increase the link reliability. A simple structure for the MIMO is to use a number of transmitters emitting the same signal. This technique is currently available in commercial systems where a number of laser sources can be arranged in one FSO terminal, e.g. "SONAbeam$^{\text{TM}}$ 1250-M" [13]. A key element in FSO MIMO channels is the design of simple yet efficient signaling algorithm that can be decoded easily at Gbps communication.

Finally, a major step in FSO system design is to verify the theoretical results with practical measurements. Currently, an FSO system at McMaster University is being installed which will establish a communication link of approximately 1.5 km. This link can be utilized to verify most of the results presented in this thesis. In particular, the importance of the non-uniform input distribution at low SNRs when an input distribution with two mass points is considered. The achievable gain in rate compared to the uniform distribution can be measured easily.

Appendices

Appendix A

$h_p(r)$ Approximation

Consider approximating the integration in (??) by an integration over a square of equal area to the detector, i.e., with side length $\sqrt{\pi}a$. It follows that, (??) can be approximated as,

$$h_p(r) \approx \int_{-\sqrt{\pi}a/2}^{\sqrt{\pi}a/2} \frac{\sqrt{2}E}{\sqrt{\pi w_z^2}} \exp\left(-\frac{2(x'-r)^2}{w_z^2}\right) dx',$$

where $E = \operatorname{erf}\left(\frac{\sqrt{\pi}a}{\sqrt{2}w_z}\right)$ and $\operatorname{erf}(x) = \frac{2}{\sqrt{\pi}}\int_0^x e^{-u^2}du$ is the error function. Expanding the exponential term into its Taylor series, integrating and simplifying results in,

$$h_p(r) \approx \frac{\sqrt{2}aE}{w_z} + \frac{2E}{\sqrt{\pi}} \sum_{\substack{m=3\\ odd}}^{\infty} \sum_{\substack{\ell=0\\ even}}^{m} \frac{(-1)^{(m-1)/2}}{(m)\left(\frac{m-1}{2}\right)!} \times \binom{m}{\ell} \left(\sqrt{2}\frac{r}{w_z}\right)^{\ell} \left(\frac{\sqrt{\pi}a}{\sqrt{2}w_z}\right)^{m-\ell} \tag{A.1}$$

In addition, (A.1) can be rearranged with respect to ℓ and written in the compact form

$$h_p(r) \approx \sum_{\substack{\ell=0\\ even}}^{\infty} A_\ell \left(\frac{\sqrt{2}\,r}{w_z}\right)^{\ell} \tag{A.2}$$

where A_ℓ's are given by,

$$A_\ell = \frac{2E}{\sqrt{\pi}} \sum_{\substack{m=\ell+1 \\ odd}}^{\infty} \frac{(-1)^{(m-1)/2}}{(m)\left(\frac{m-1}{2}\right)!} \begin{pmatrix} m \\ \ell \end{pmatrix} \left(\frac{\sqrt{\pi}a}{\sqrt{2}w_z}\right)^{m-\ell}.$$

Defining $v = (\sqrt{\pi}a)/(\sqrt{2}w_z)$ and simplifying gives,

$$A_0 = [\text{erf}(v)]^2, \qquad A_2 = \frac{-2}{\sqrt{\pi}} \text{erf}(v) \; \left[v \exp(-v^2)\right].$$

Equating the first two terms of the Taylor expansion of a Gaussian pulse equal to the same terms in (A.2) gives (??),

$$h_p(r) \approx A_0 \exp\left(-\frac{2r^2}{w_{z_{eq}}^2}\right),$$

where, $w_{z_{eq}}^2 = w_z^2 A_0/|A_2|$.

Appendix B

Upper Bound on γ_m

Recall the given expression for γ_m as,

$$\gamma_m = \binom{n}{m}\frac{1}{2^{n-m}} + \binom{n}{m+1}\frac{m+1}{\sqrt{\pi}} \times \int_0^\infty e^{-(1+m)x^2}\left[1-\frac{1}{2}\mathrm{erfc}(x)\right]^{n-m-1} dx.$$

Consider the second term and define $\mathcal{G}$ as,

$$\mathcal{G} = \frac{m+1}{\sqrt{\pi}}\int_0^\infty e^{-(1+m)x^2}\left[1-\frac{1}{2}\mathrm{erfc}(x)\right]^{n-m-1} dx.$$

Substituting with the inequality,

$$\left[1-\frac{1}{2}\mathrm{erfc}(x)\right] \geq \frac{1}{2}, \qquad x \geq 0,$$

results in

$$\begin{aligned}
\mathcal{G} &> \frac{m+1}{\sqrt{\pi}}\int_0^\infty e^{-(1+m)x^2}\left(\frac{1}{2}\right)^{n-m-1} dx, \\
&= \frac{1}{2^{n-m}}\sqrt{m+1}\left[\frac{\sqrt{\pi}}{2}\int_0^\infty e^{-t^2}dt\right], \\
&= \frac{1}{2^{n-m}}\sqrt{m+1}, \\
&\geq \frac{1}{2^{n-m}}.
\end{aligned}$$

Thus γ_m can be upper bounded as,

$$\begin{aligned}
\gamma_m &= \binom{n}{m}\frac{1}{2^{n-m}} + \binom{n}{m+1}\mathcal{G} \\
\gamma_m &< \left[\binom{n}{m} + \binom{n}{m+1}\right]\mathcal{G}, \\
&< \binom{n+1}{m+1}\mathcal{G}
\end{aligned}$$

Consider the following inequality for the erfc(x) function (see Appendix C),

$$\mathrm{erfc}(x) > \frac{2}{e}\, e^{-2x^2} \Longrightarrow e^{-x^2} < \sqrt{\frac{e}{2}\,\mathrm{erfc}(x)},$$

then γ_m can be further upper bounded as follows,

$$\begin{aligned}
\gamma_m &< \binom{n+1}{m+1}\mathcal{G} \\
&= \binom{n+1}{m+1}\frac{m+1}{\sqrt{\pi}}\int_0^\infty e^{-(1+m)x^2}\left[1-\frac{1}{2}\mathrm{erfc}(x)\right]^{n-m-1} dx \\
&< \binom{n+1}{m+1}\frac{m+1}{\sqrt{\pi}}\int_0^\infty e^{-x^2}\left[\frac{e}{2}\,\mathrm{erfc}(x)\right]^{\frac{m}{2}}\left[1-\frac{1}{2}\mathrm{erfc}(x)\right]^{n-m-1} dx.
\end{aligned}$$

Substitute with $\mathrm{erfc}(x) = 2u$ we get,

$$\begin{aligned}
\gamma_m &< \binom{n+1}{m+1}(m+1)(\sqrt{e})^m \int_0^{1/2} u^{\frac{m}{2}}(1-u)^{n-m-1}du, \\
&< \binom{n+1}{m+1}(m+1)(\sqrt{e})^m \underbrace{\int_0^1 u^{\frac{m}{2}}(1-u)^{n-m-1}du}_{\mathrm{B}\left(\frac{m}{2}+1,n-m\right)}.
\end{aligned}$$

where $\mathrm{B}(\cdot,\cdot)$ is the Beta function,

$$\mathrm{B}\left(\frac{m}{2}+1, n-m\right) = \frac{\Gamma(\frac{m}{2}+1)\Gamma(n-m)}{\Gamma(n-\frac{m}{2}+1)}.$$

Finally, γ_m is upper bounded as

$$\begin{aligned}\gamma_m &< \binom{n+1}{m+1}(m+1)(\sqrt{e})^m \frac{\Gamma(\frac{m}{2}+1)\Gamma(n-m)}{\Gamma(n-\frac{m}{2}+1)},\\ &= \frac{\Gamma(n+2)}{\Gamma(m+2)}(m+1)(\sqrt{e})^m \frac{\Gamma(\frac{m}{2}+1)}{\Gamma(n-\frac{m}{2}+1)},\\ &= \lambda_m.\end{aligned}$$

Appendix C

Erfc(x) Lower Bound

Theorem C.1

$$\operatorname{erfc}(x) > \frac{2}{e}\, e^{-2x^2}, \quad x \geq 0,$$

Proof. The inequality clearly holds at x=0. Let $s > 0$ and define $f(x)$ as,

$$f(x) = \operatorname{erfc}(x) - s\, e^{-2x^2} > 0, \quad x \geq 0. \tag{C.1}$$

Consider the general case of find $s > 0$, such that (C.1) is satisfied. Equivalently, this problem can be reformulated as: find $s > 0$ such that

$$f(x_i) = \operatorname{erfc}(x_i) - s\, e^{-2x_i^2} > 0, \quad \forall x_i \geq 0, \tag{C.2}$$

where x_i is the location of the i^{th} extremum of $f(x)$, i.e., the i^{th} root of $f'(x)$.

Lemma C.1 *$f(x)$ has a minima at $x = x_1$ and a maxima at $x = x_2$ when $s > \sqrt{e/2\pi}$ where $0 < x_1 < \frac{1}{\sqrt{2}} < x_2$.*

Proof. The locations of the extrema can be found by considering the derivative $f'(x)$ given by,

$$f'(x) = \frac{2}{\sqrt{\pi}}\, e^{-x^2} \left[2\sqrt{\pi} s x\, e^{-x^2} - 1\right]. \tag{C.3}$$

Solving for $f'(x_i) = 0$ results in,

$$s = \frac{e^{x_i^2}}{2\sqrt{\pi}\, x_i}. \tag{C.4}$$

Define

$$g(x) = \frac{e^{x^2}}{2\sqrt{\pi}\, x}, \qquad x > 0,$$

and consider the derivative $\partial g(x)/\partial x$ as

$$\frac{\partial g(x)}{\partial x} = \frac{(2x^2-1)}{2\sqrt{\pi}\, x^2} e^{x^2} = \begin{cases} \text{negative} & x < \frac{1}{\sqrt{2}}, \\ \text{positive} & x > \frac{1}{\sqrt{2}}. \end{cases}$$

Clearly, $g(x)$ is monotonically decreasing then monotonically increasing with x where the limiting point is $x_0 = 1/\sqrt{2}$ and the corresponding $g(x_0) = \sqrt{e/2\pi}$. Recall (C.4), when $s > \sqrt{e/2\pi}$ there are two solutions for (C.4) located at $x_1 < \frac{1}{\sqrt{2}}$ and $x_2 > \frac{1}{\sqrt{2}}$ as shown in Fig. C.1, i.e., two extrema for $f(x)$. In order to distinguish the location of the minima, consider the second derivative

$$f''(x) = \frac{2e^{-x^2}}{\sqrt{\pi}} \left[2\sqrt{\pi} s e^{-x^2}(1-2x^2) + 2x\right].$$

Since $0 < x_1 \leq \frac{1}{\sqrt{2}}$, $f''(x_1) > 0$, i.e., a minima for $f(x)$ exists at x_1. As a result, $f(x)$ has a minima at x_1 followed by a maxima at x_2. ■

As a result, it is sufficient to prove that $f(x_1) > 0$ where $0 < x_1 \leq \frac{1}{\sqrt{2}}$. Substituting s from (C.4) into (C.2) the problem can be reformulated as proving the following,

$$\mathrm{erfc}(x_1) > \frac{e^{-x_1^2}}{2\sqrt{\pi} x_1}, \qquad 0 < x_1 < \frac{1}{\sqrt{2}}. \tag{C.5}$$

Lemma C.2 $\mathrm{erfc}(y) > \frac{e^{-y^2}}{2\sqrt{\pi} y}$ *when* $y = \frac{1}{\sqrt{\pi+2}} < \frac{1}{\sqrt{2}}$.

Proof. Consider the following lower bound on $\mathrm{erfc}(x)$ with $a = 1/\pi$ and $b = 2\pi$ [139],

$$\mathrm{erfc}(x) > \frac{1}{\sqrt{\pi}} e^{-x^2} \left[\frac{1}{(1-a)x + a\sqrt{x^2 + b/2}}\right], \tag{C.6}$$

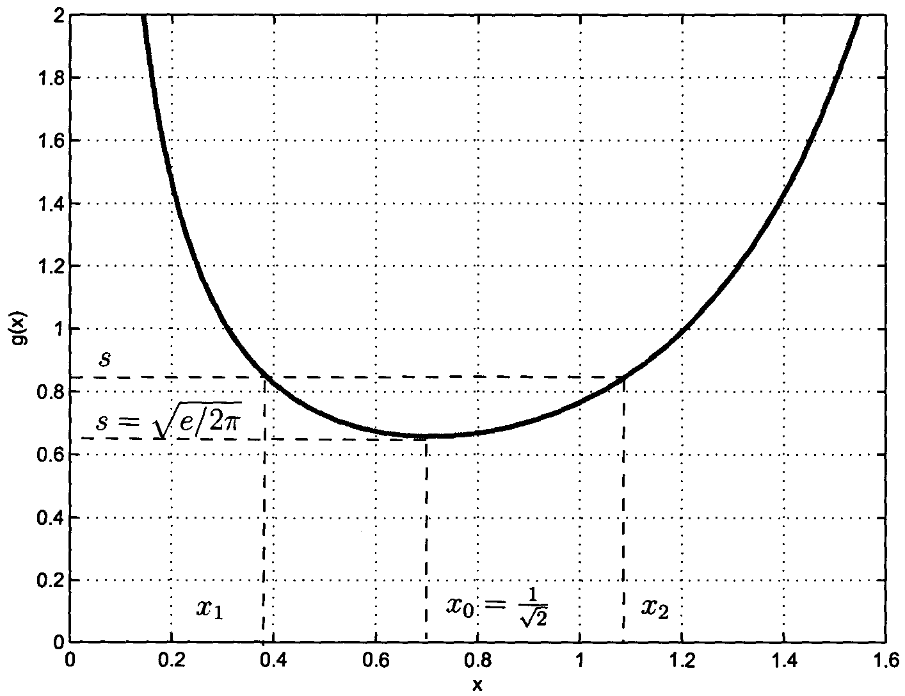

Figure C.1: A plot for $g(x)$ versus x. For a given $s > \sqrt{e/2\pi}$ two roots x_1 and x_2 exist.

Notice that,

$$\frac{e^{-y^2}}{\sqrt{\pi}}\left[\frac{1}{(1-a)y+a\sqrt{y^2+b/2}}\right]=\frac{e^{-y^2}}{2\sqrt{\pi}y}.$$

when

$$y=\frac{1}{\sqrt{\pi+2}}<\frac{1}{\sqrt{2}}.$$

Therefore,

$$\operatorname{erfc}(y)>\frac{e^{-y^2}}{2\sqrt{\pi}y},\qquad \text{when}\qquad y=\frac{1}{\sqrt{\pi+2}}.$$

■

Substituting $x_1=\frac{1}{\sqrt{\pi+2}}<\frac{1}{\sqrt{2}}$ into (C.4) gives

$$s=s^*=\sqrt{\frac{\pi+2}{4\pi}}\,e^{1/(\pi+2)}.$$

By substituting s^* into (C.2) and following Lemma C.2,

$$f(x_1)=\operatorname{erfc}(x_1)-s^*\,e^{-2x_1^2}>0. \tag{C.7}$$

Since $f(x_1)>0$, at the minima x_1, as shown in (C.7), then $f(x)>0$ for all $x\geq 0$, i.e.,

$$f(x)=\operatorname{erfc}(x)-s^*\,e^{-2x^2}>0,\qquad x\geq 0.$$

Since $2/e<s^*$, then

$$\operatorname{erfc}(x)>\frac{2}{e}\,e^{-2x^2},\qquad x\geq 0$$

as substituted in Appendix B.

■

Appendix D

Limit of $\phi(\alpha, n)$

Consider the expression for $\phi(\alpha, n)$ given by

$$\phi(\alpha, n) = \frac{1}{n}\log_2\left[\frac{\kappa_{(1-\alpha)n}\,\lambda_{\alpha n}}{\kappa_n\,\Gamma(\alpha n+1)}\left(\frac{nP}{\varrho}\right)^{\alpha n}\right].$$

Substituting with

$$\lambda_{\alpha n} = \frac{\Gamma(n+2)}{\Gamma(\alpha n+2)}\frac{\Gamma(\frac{\alpha n}{2}+1)}{\Gamma(n-\frac{\alpha n}{2}+1)}(\alpha n+1)(\sqrt{e})^{\alpha n},$$

$$\kappa_n = \frac{\pi^{n/2}}{\Gamma(\frac{n}{2}+1)},$$

and

$$\varrho = \sqrt{n\sigma},$$

results in

$$\phi(\alpha, n) = \frac{1}{n}\log_2\left[\frac{\Gamma(\frac{n}{2}+1)\Gamma(n+2)\Gamma(\frac{\alpha n}{2}+1)\left(\sqrt{\frac{n\,e}{\pi}}\right)^{\alpha n}}{(\Gamma(\alpha n+1))^2\,\Gamma\left(\frac{(1-\alpha)}{2}n+1\right)\Gamma\left((1-\frac{\alpha}{2})n+1\right)}\left(\frac{P}{\sigma}\right)^{\alpha n}\right].$$

The Gamma functions in $\phi(\alpha, n)$ can be substituted using Stirling's approximation [140, Eq. 11] given as

$$\underbrace{\sqrt{2\pi n}\left(\frac{n}{e}\right)^n e^{\left(\frac{1}{12n+1}\right)}}_{L_\Gamma} < \Gamma(n+1) < \underbrace{\sqrt{2\pi n}\left(\frac{n}{e}\right)^n e^{\left(\frac{1}{12n}\right)}}_{U_\Gamma}.$$

Substituting $\Gamma(\cdot)$ by L_Γ in the numerator (denominator) and U_Γ in the denominator (numerator) results in a lower (upper) bound on $\phi(\alpha, n)$ denoted by $\phi_1(\alpha, n)$ $(\phi_2(\alpha, n))$ respectively. This can be expressed as follows,

$$\phi_1(\alpha, n) \leq \phi(\alpha, n) \leq \phi_2(\alpha, n)$$

Consider the limit of $\phi_1(\alpha, n)$ as $n \to \infty$ and simplifying the expression results in,

$$\lim_{n\to\infty} \phi_1(\alpha, n) = \lim_{n\to\infty} \frac{1}{n} \log_2 \left[\left(\sqrt{\frac{e^2}{4\pi}}\right)^{\alpha n+1} \left(\frac{P}{\sigma}\right)^{\alpha n} \frac{\left(\sqrt{n}\right)^{2\alpha-3}}{\alpha^{\frac{3}{2}\alpha n+\frac{1}{2}} \cdot (1-\alpha)^{\frac{3+(1-\alpha)n}{2}} \cdot (1-\frac{\alpha}{2})^{\frac{1}{2}+(1-\frac{\alpha}{2})n}} \right],$$

which can be written as,

$$\lim_{n\to\infty} \phi_1(\alpha, n) = \lim_{n\to\infty} \frac{1}{n} \log_2 \left[\left(\sqrt{\frac{e^2}{4\pi}}\right)^{\alpha n} \left(\frac{P}{\sigma}\right)^{\alpha n} \frac{1}{(\Theta(\alpha))^n} \right] +$$
$$\underbrace{\lim_{n\to\infty} \frac{1}{n} \log_2 \left[\left(\sqrt{\frac{e^2}{4\pi}}\right) \frac{\left(\sqrt{n}\right)^{2\alpha-3}}{\alpha^{\frac{1}{2}} \cdot (1-\alpha)^{\frac{3}{2}} \cdot (1-\frac{\alpha}{2})^{\frac{1}{2}}} \right]}_{0},$$

where

$$\Theta(\alpha) = \alpha^{\frac{3\alpha}{2}} \, (1-\alpha)^{\frac{(1-\alpha)}{2}} \left(1 - \frac{\alpha}{2}\right)^{(1-\frac{\alpha}{2})}.$$

Then

$$\lim_{n\to\infty} \phi_1(\alpha, n) = \log_2 \left[\left(\sqrt{\frac{e^2}{4\pi}}\right)^{\alpha} \left(\frac{P}{\sigma}\right)^{\alpha} \frac{1}{\Theta(\alpha)} \right] = L_\alpha.$$

Following the same steps it can be shown that,

$$\lim_{n\to\infty} \phi_1(\alpha, n) = \lim_{n\to\infty} \phi_2(\alpha, n) = L_\alpha$$

where L_α exist for all $\alpha \in [0, 1]$.

Squeeze Theorem [141]: *Given that*

$$g(x) \leq f(x) \leq h(x)$$

and

$$\lim_{x \to a} g(x) = \lim_{x \to a} h(x) = L,$$

then

$$\lim_{x \to a} f(x) = L.$$

Applying the *squeeze theorem* results in

$$\lim_{n \to \infty} \phi(\alpha, n) = L_\alpha,$$

i.e., the limit of $\phi(\alpha, n)$ as $n \to \infty$ exists for all $\alpha \in [0, 1]$.

Appendix E

Limit of the Supremum

Given that the limit of $\phi(\alpha, n)$ as $n \to \infty$ exists for any α, i.e., (see Appendix D),

$$\lim_{n\to\infty} \phi(\alpha, n) = L_\alpha.$$

Then for any $\alpha \in (0,1)$ and $\epsilon > 0$ there exist an n_α such that

$$|\phi(\alpha, n) - L_\alpha| < \epsilon, \qquad n > n_\alpha.$$

Let $n^*_\alpha = \sup_\alpha \{n_\alpha\}$ then,

$$|\phi(\alpha, n) - L_\alpha| < \epsilon, \qquad n > n^*_\alpha,$$

that is

$$L_\alpha - \epsilon < \phi(\alpha, n) < L_\alpha + \epsilon, \qquad n > n^*_\alpha.$$

Since ϵ is a constant and the above inequality is valid for any α, then considering the supremum of each side results in,

$$\sup_\alpha[L_\alpha] - \epsilon < \sup_\alpha[\phi(\alpha, n)] < \sup_\alpha[L_\alpha] + \epsilon, \qquad n > n^*_\alpha. \tag{E.1}$$

On the other hand, let L_s denote the limit of the supremum as follows,

$$\lim_{n\to\infty}\left[\sup_\alpha \ \phi(\alpha, n)\right] = L_s.$$

Then for any $\delta > 0$ there exist an n_o such that

$$L_s - \delta < \sup_{\alpha} \; [\phi(\alpha, n)] < L_s + \delta, \qquad n > n_o \tag{E.2}$$

Consider the right hand side of (E.1) and the left hand side of (E.2) and for $n > \max\{n_o, n_\alpha^*\}$ we get,

$$L_s - \delta < \sup_{\alpha} \; [\phi(\alpha, n)] < \sup_{\alpha}[L_\alpha] + \epsilon,$$

and it follows that

$$L_s - (\delta + \epsilon) < \sup_{\alpha}[L_\alpha]. \tag{E.3}$$

Again consider the left hand side of (E.1) and the right hand side of (E.2) and for $n > \max\{n_o, n_\alpha^*\}$ we get,

$$\sup_{\alpha}[L_\alpha] - \epsilon < \sup_{\alpha} \; [\phi(\alpha, n)] < L_s + \delta,$$

and it follows that

$$\sup_{\alpha}[L_\alpha] < L_s + (\delta + \epsilon). \tag{E.4}$$

Combining (E.3) and (E.4) , the following inequality is obtained,

$$L_s - (\delta + \epsilon) < \sup_{\alpha} \; [L_\alpha] < L_s + (\delta + \epsilon), \quad n > \max\{n_o, n_\alpha^*\}, \tag{E.5}$$

Since (E.5) is valid for any $\delta > 0$ and $\epsilon > 0$ then

$$\sup_{\alpha} \; [L_\alpha] = L_s$$

which can be written in the original format as follows,

$$\sup_{\alpha} \left[\lim_{n \to \infty} \phi(\alpha, n) \right] = \lim_{n \to \infty} \left[\sup_{\alpha} \phi(\alpha, n) \right]$$

Appendix F

Uniqueness of the root t_0

Lemma F.1 *The polynomial $S(t)$ in* (4.10) *has a unique positive real root $t_0 \in [0, 1]$.*

Proof. Consider the polynomial

$$S(t) = \sum_{k=0}^{K} \left(1 - k\frac{\rho}{K}\right) t^k$$

where $\rho \geq 2$. It is straightforward to show

$$S(0) = 1, \quad \text{and} \quad S(1) = (K+1)\left(1 - \frac{\rho}{2}\right) \leq 0 \tag{F.1}$$

By the intermediate value theorem of continuous functions, there exists *at least* one real root for $S(t)$ in the interval $[0, 1]$. Note that a root at $t = 1$ exist when $\rho = 2$.

Consider ordering the coefficients of this polynomial in terms of ascending exponents of the variable t. Note that the first coefficient is positive and equal to one independent of ρ and K while the last coefficient is negative since $\rho \geq 2$. Notice also that the coefficients decay linearly with increasing exponent and thus there must exist a $k = k^*$ such that

$$\left(1 - k\frac{\rho}{K}\right) \Longrightarrow \begin{cases} \text{positive}, & k \leq k^*, \\ \text{negative}, & k > k^*. \end{cases}$$

More precisely, the number of variations in sign in this ordering of the coefficients of $S(t)$ is one. For completeness, consider the following well-known theorem.

> **Descartes' Rule of Signs** [142]: *Let $S(t)$ be a polynomial with real coefficients ordered in terms of ascending powers of the variable. The number of positive roots of $S(t)$ is either equal to the number of variations in sign of consecutive non-zero coefficients of $S(t)$ or less than this by a multiple of 2.*

Applying Descartes' Rule of Signs, $S(t)$ has a single root for $t \geq 0$. Since it has already been demonstrated that a real root exists in $[0, 1]$, thus $S(t)$ has a unique real root $t_0 \in [0, 1]$.

Bibliography

[1] M. P. Christensen, P. Milojkovic, M. J. McFadden, and M. W. Haney, "Multiscale optical design for global chip-to-chip optical interconnections and misalignment tolerant packaging," *IEEE Journal of Selected Topics in Quantum Electronics*, vol. 9, pp. 548–556, Mar. 2003.

[2] M. R. Pakravan and M. Kavehrad, "Indoor wireless infrared channel characterization by measurements," *IEEE Transactions on Vehicular Technology*, vol. 50, pp. 1053–1073, July 2001.

[3] S. S. Muhammad, P. Kohldorfer, and E. Leitgeb, "Channel modeling for terrestrial FSO links," in *Proceedings of the International Conference on Transparent Optical Networks*, Barcelona, Spain., 2005, pp. 407–410.

[4] M. A. Naboulsi, H. Sizun, and F. de Fornel, "Fog attenuation prediction for optical and infrared waves," *Optical Engineering*, vol. 43, pp. 319–329, Feb. 2004.

[5] "Unmanned airship solutions for integrated ISR and communications systems," http://www.sanswiretao.com/Sanswire-UAV.pdf, Sanswire Corporation, [online], last accessed: Mar. 30, 2009.

[6] A. Harris, J. J. Sluss, H. H. Refai, and P. G. LoPresti, "Alignment and tracking of a free-space optical communications link to a UAV," in *Proceedings of the 24th Digital Avionics Systems Conference (DASC)*, Oct. 2005, pp. 1.C.2 1–9.

[7] J. Horwath, N. Perlot, M. Knapek, and F. Moll, "Experimental verification of optical backhaul links for high altitude platform networks: Atmospheric turbulence and downlink availability," . *International Journal of Satellite Communications and Networking*, vol. 25, pp. 501–528, 2007.

[8] D. Giggenbach, J. Horwath, and B. Epple, "Optical satellite downlinks to optical ground stations and high-altitude platforms," *Proceedings of IEEE IST Mobile & Wireless Communication Summit*, pp. 1–4, 2007.

[9] C. C. Chen and C. S. Gardner, "Impact of random pointing and tracking errors on the design of coherent and incoherent optical intersatellite communication links," *IEEE Transactions on Communications*, vol. 37, pp. 252–260, Mar. 1989.

[10] A. Polishuk and S. Arnon, "Optimization of laser satellite communication system with an optical preamplifier," *Journal of Optical Society of America A*, vol. 21, pp. 1307–1315, July 2004.

[11] "The website for the defence industries-air force unmanned aerial vehicles (UAV)," http://www.airforce-technology.com/contractors/uav/, [online], last accessed: Mar. 30, 2009.

[12] J. C. Juarez, A. Dwivedi, A. R. Hammons, S. D. Jones, V. Weerackody, and R. A. Nichols, "Free-space optical communications for next-generation military networks," *IEEE Communications Magazine*, vol. 44, pp. 46–51, Nov. 2006.

[13] fSONA Optical Wireless. [Online]. Available: http://www.fsona.com

[14] MRV Communications Inc. [Online]. Available: http://www.mrv.com

[15] D. M. Forin, G. M. T. Beleffi, F. Curti, N. Corsi, V. D. Sanctis, V. Sacchieri, A. J. L. Teixeira, and G. Cincotti, "On field test of a wavelength division multiplexing free-space optics transmission at very high bit rates," in *Proceedings of the 9th International Conference on Telecommunications, ConTel*, Zagreb, Croatia, 2007, pp. 77–80.

[16] P. L. Chen and *et al*, "Demonstration of 16 channels 10 Gb/s wdm free space transmission over 2.16 km," in *Proceedings of the IEEE/LEOS Summer Topical Meetings*, Acapulco, Mexico, 2008, pp. 235–236.

[17] I. Kim, B. McArthur, and E. Korevaar, "Comparison of laser beam propagation at 785 nm and 1550 nm in fog and haze for optical wireless communications," *Proceedings SPIE*, vol. 4214, pp. 26–37, Feb. 2001.

[18] S. Ahmadi, "An overview of next-generation mobile WiMAX technology," *IEEE Communications Magazine*, vol. 47, pp. 84–98, 2009.

[19] S. J. Vaughan-Nichols, "Mobile WiMax: The next wireless battle ground," *IEEE Computer*, vol. 41, pp. 16–18, 2008.

[20] LightPointe^{TM}. [Online]. Available: http://www.lightpointe.com

[21] J. Wells, "WiFiber versus 60 GHz wireless," *GigaBeam white paper*, Aug. 2005.

[22] GigaBeam Corporation. [Online]. Available: http://www.gigabeam.com

[23] LaserOptronics, A Division of AIRLINX Communications, Inc. (2009). [Online]. Available: http://www.laseroptronics.com

[24] D. A. Rockwell and G. S. Mecherle, "Optical wireless: low-cost, broadband, optical access," *fSONA white paper*, 2001.

[25] LightPointe^{TM} Press. (2009, Apr.) Lightpointe unveils performance enhanced Flightlite^{TM}G FSO wireless bridging solution. [Online]. Available: http://www.lightpointe.com/company/pressrelease_04_15_09.cfm

[26] D. J. Heatley, D. R. Wisely, I. Neild, and P. Cochrane, "Optical wireless: the story so far," *IEEE Communications Magazine*, pp. 72–82, Dec. 1998.

[27] J. M. Kahn and J. R. Barry, "Wireless infrared communications," *Proceedings of the IEEE*, vol. 85, pp. 265–298, Feb. 1997.

[28] S. Karp, R. Gagliardi, S. Moran, and L. Stotts, *Optical Channels.* New York: Plenum, 1988.

[29] International Electrotechnical Commission. (2009). [Online]. Available: http://www.iec.ch

[30] M. Jeganathan and P. Ionov. Multi-gigabits-per-second optical wireless communications. [Online]. Available: http://www.freespaceoptic.com/WhitePapers

[31] X. Zhu and J. Kahn, "Free space optical communication through atmospheric turbulence channels," *IEEE Transactions on Communications*, vol. 50, pp. 1293–1300, Aug. 2002.

[32] E. A. Lee and D. G. Messerschmitt, *Digital Communication*, 2nd ed. Boston, MA, USA: Kluwer Academic Publishers, 1994.

[33] G. P. Agrawal, *Fiber-Optic Communication Systems*, 3rd ed. Toronto, Canada: John Wiley and Sons, 2002.

[34] S. Hranilovic, *Wireless optical communication systems.* New York: Springer, 2005.

[35] E. Biglieri, J. Proakis, and S. Shamai, "Fading channels: information-theoretic and communications aspects," *IEEE Transactions on Information Theory*, vol. 44, pp. 2619–2692, Oct. 1998.

[36] L. Jing and M. Uysal, "Optical wireless communications: System model, capacity and coding," in *IEEE 58th Veh. Tech. Conf.*, Florida, USA, Oct. 2003, pp. 168–172.

[37] L. Andrews and R. Phillips, *Laser Beam Propagation Through Random Media*, 2nd ed. Bellingham, Washington: SPIE, 2005.

[38] R. M. Gagliardi and S. Karp, *Optical Communication.* New York: John Wiley, 1976.

[39] R. J. Hill and G. R. Ochs, "Inner-scale dependence of scintillation variances measured in weak scintillation," vol. 9, pp. 1406–1411, Aug. 1992.

[40] L. C. Andrews, R. L. Phillips, C. Y. Hopen, and M. A. Al-Habash, "Theory of optical scintillation," *Journal of Optical Society of America A*, vol. 16, pp. 1417–1429, June 1999.

[41] M. A. Al-Habash, L. C. Andrews, and R. L. Philips, "Mathematical model for the irradiance probability density function of a laser propagating through turbulent media," *Optical Engineering*, vol. 40, pp. 1554–1562, Aug. 2001.

[42] L. C. Andrews and R. L. Phillips, "I-K distribution as a universal propagation model of laser beams in atmospheric turbulence," *Journal of Optical Society of America A*, vol. 2, pp. 160–163, Feb. 1985.

[43] S. M. Flatte, C. Bracher, and G. Y. Wang, "Probability density functions of irradiance for waves in atmospheric turbulence calculated by numerical simulations," *Journal of Optical Society of America A*, vol. 11, pp. 2080–2092, July 1994.

[44] J. H. Churnside and R. G. Frehlich, "Experimental evaluation of log-normally modulated Rician and I-K models of optical scintillation in the atmosphere," *Journal of Optical Society of America A*, vol. 6, pp. 1760–1766, Nov. 1989.

[45] F. S. Vetelino, B. Clare, K. Corbett, C. Young, K. Grant, and L. Andrews, "Characterizing the propagation path in moderate to strong optical turbulencee," vol. 45, pp. 3534–3543, May 2006.

[46] R. J. Hill and R. G. Frehlich, "Probability distribution of irradiance for the onset of strong scintillation," *Journal of Optical Society of America A*, vol. 14, pp. 1530–1540, July 1997.

[47] F. S. Vetelino, C. Young, L. Andrews, and J. Recolons, "Aperture averaging effects on the probability density of irradiance fluctuations in moderate-to-strong turbulence," vol. 46, pp. 2099–2108, Apr. 2007.

[48] J. D. Barry and G. S. Mecherle, "Beam pointing error as a significant parameter for satellite borne, free-space optical communication systems," *Optical Engineering*, vol. 24, pp. 1049–1054, Nov. 1985.

[49] G. A. Koepf, R. Peters, and R. G. Marshalek, "Analysis of brust error occurrence on optical intersatellite link (ISL) design," *Proc. SPIE Opt. Tech. Commun. Satellite Applications*, vol. 616, pp. 129–136, Jan. 1986.

[50] S. Arnon and N. S. Kopeika, "Laser satellite communication network vibration effect and possible solutions," *Proceedings of the IEEE*, vol. 85, pp. 1646–1661, Oct. 1997.

[51] S. Arnon, "Effects of atmospheric turbulence and building sway on optical wireless communication systems," *Optics Letters*, vol. 28, pp. 129–131, Jan. 2003.

[52] ——, "Optimization of urban optical wireless communication systems," *IEEE Transactions on Communications*, vol. 2, pp. 626–629, Nov. 2003.

[53] S. Arnon, S. Rotman, and N. S. Kopeika, "Beam width and transmitter power adaptive to tracking system performance for free-space optical communication," *Journal of Applied Optics*, vol. 36, pp. 6095–6101, Aug. 1997.

[54] K. Kiasaleh, "On the probability density function of signal intensity in free-space optical communications systems impaired by pointing jitter and turbulence," *Optical Engineering*, vol. 33, pp. 3748–3757, Nov. 1994.

[55] O. Steinvall, "Performance of laser tracking of small targets during turbulence and beam jitter," *Optical Engineering*, vol. 43, pp. 1609–1621, July 2004.

[56] C. E. Shannon, "A mathematical theory of communication," *Bell Syst. Tech. J.*, vol. 27, pp. 379–423, July/Oct 1948.

[57] T. M. Cover and J. A. Thomas, *Elements of Information Theory.* New York: Wiely, 1991.

[58] E. Telatar, "Capacity of multi-antenna Gaussian channels," in *Laboratories Internal Technical Memo*, AT&T-Bell, June 1995.

[59] A. A. Farid and S. Hranilovic, "Upper and lower bounds on the capacity of wireless optical intensity channels," in *Proceedings of the IEEE International Symposium on Information Theory*, Nice, France, 2007, pp. 2416–2420.

[60] S. Hranilovic and F. R. Kschischang, "Capacity bounds for power- and band-limited optical intensity channels corrupted by Gaussian noise," *IEEE Transactions on Information Theory*, vol. 50, pp. 784–795, May 2004.

[61] S. M. Moser, "Duality-based bounds on channel capacity," Ph.D. dissertation, Swiss Fedral Institute of Technology Zürich, 2005.

[62] A. Lapidoth, S. M. Moser, and M. A. Wigger, "On the capacity of free-space optical intensity channels," in *Proceedings of the IEEE International Symposium on Information Theory*, Toronto, Canada., 2008, pp. 2419–2423.

[63] C. E. Shannon, "Communication in the presence of noise," *Proc. IRE*, vol. 37, pp. 10–21, Jan. 1949.

[64] S. Hranilovic and F. R. Kschischang, "Optical intensity-modulated direct detection channels: Signal space and lattice codes," *IEEE Transactions on Information Theory*, vol. 49, no. 6, pp. 1385–1399, June 2003.

[65] R. You and J. M. Kahn, "Upper-bounding the capacity of optical IM/DD channels with multiple-subcarrier modulation and fixed bias using trigonometric momentspace method," *IEEE Transactions on Information Theory*, vol. 48, pp. 514–523, Feb. 2002.

[66] A. Lapidoth and S. M. Moser, "Capacity bounds via duality with applications to multiple-anntena systems on flat fading channels," *IEEE Transactions on Information Theory*, vol. 49, pp. 2426–2467, Oct. 2003.

[67] J. G. Smith, "The information capacity of amplitude and variance-constrained scalar Gaussian channels," *Inf. Contr.*, vol. 18, pp. 203–219, 1971.

[68] S. Shamai, "Capacity of a pulse amplitude modulated direct detection photon channel," *in Proceedings IEE Communication Speech and Vission*, vol. 137, pp. 424–430, Dec. 1990.

[69] S. Shamai and I. Bar-David, "The capacity of average and peak-power-limited quadrature Gaussian channels," *IEEE Transactions on Information Theory*, vol. 41, no. 4, pp. 1060–1071, July 1995.

[70] I. C. Abou-Faycal, M. D. Trott, and S. Shamai, "The capacity of discrete-time memoryless Rayleigh-fading channels," *IEEE Transactions on Information Theory*, vol. 47, no. 4, pp. 1290–1301, May 2001.

[71] M. Katz and S. Shamai, "On the capacity-achieving distribution of the discrete-time noncoherent additive white noise channel," in *Proceedings of the IEEE International Symposium on Information Theory*, Lausanne, Switzerland, June 2002, p. 165.

[72] A. Das, "Capacity-achieving distributions for non-Gaussian additive noise channels," in *Proceedings of the IEEE International Symposium on Information Theory*, Sorrento, Italy, June 2000, p. 432.

[73] M. C. Gursoy, H. V. Poor, and S. Verdú, "On the capacity-achieving distribution of the noncoherent Rician fading channel," in *Canadian Workshop on Information Theory*, Waterloo, ON, Canada, May 2003, pp. 24–27.

[74] T. H. Chan, S. Hranilovic, and F. R. Kschischang, "Capacity-achieving probability measure for conditionally Gaussian channels with bounded inputs," *IEEE Transactions on Information Theory*, vol. 51, pp. 2073–2088, June 2005.

[75] T. Ohtsuki, "Multiple-subcarrier modulation in optical wireless communications," *IEEE Communications Magazine*, vol. 41, pp. 74–79, Mar. 2003.

[76] Q. Lu and Q.Liu, "Subcarrier PSK intensity modulation for optical wireless communications through turbulent atmospheric channel," in *Proceedings of the IEEE International Conference on Communications*, Seoul Korea, May 2005, pp. 1761–1765.

[77] Q. Lu, Q.Liu, and G. S. Mitchell, "Performance analysis for optical wireless communication systems using subcarrier PSK intensity modulation through turbulent atmospheric channel," in *Proceedings of the IEEE Global Communications Conference*, Dallas, Texas, USA, Nov. 2004, pp. 1872–1875.

[78] X. Zhu and J. M. Kahn, "Performance bounds for coded free-space optical communications through atmospheric turbulence," *IEEE Transactions on Communications*, vol. 51, pp. 1233–1239, Aug. 2003.

[79] ——, "Pairwise codeword error probability for coded free-space opticalcommunication through atmospheric turbulence channels," in *Proceedings of the IEEE International Conference on Communications*, Helsinki, Finland, June 2001, pp. 161–164.

[80] J. A. Anguita, I. B. Djordjevic, M. Neifeld, and B. V. Vasic, "Shannon capacites and error-correction codes for optical atmospheric turbulent channels," *Journal of Optical Networking*, vol. 4, pp. 586–601, Sept. 2005.

[81] M. Uysal, S. M. Navidpour, and J. Li, "Error rate performance of coded free-space optical links over strong turbulence channels," *IEEE Communications Letters*, vol. 8, pp. 635–637, Oct. 2004.

[82] M. Uysal, L. Jing, , and Y. Meng, "Error rate performance analysis of coded free-space optical links over gamma-gamma atmospheric turbulence channels," *IEEE Transactions on Wireless Communications*, vol. 5, pp. 1229–1233, June 2006.

[83] R. Gallager, *Information Theory and Reliable Communication.* New York: John Wiley and Sons, 1968.

[84] R. J. McEliece, "Are turbo-like codes effective on nonstandard channels?" *IEEE Information Theory Society Newsletter*, vol. 51, pp. 1–8, Dec. 2001.

[85] E. A. Ratzer and D. MacKay, "Sparse low-density parity check codes for channels with cross-talk," in *Proceedings of IEEE Information Theory Workshop*, Paris, France, Mar. 2003, pp. 127–130.

[86] H. Imai and S. Hirakawa, "A new multilevel coding method using error-correcting codes," *IEEE Transactions on Information Theory*, vol. 23, pp. 371–377, May 1977.

[87] U. Wachsmann, R. Fischer, and J. Huber, "Multilevel codes: theoretical concepts and practical design rules," *IEEE Transactions on Information Theory*, vol. 45, pp. 1361–1391, 1999.

[88] J. Jiang and K. R. Narayanan, "Multilevel coding for channels with non-uniform inputs and rateless transmission over the BSC," in *Proceedings of the IEEE International Symposium on Information Theory*, Seattle, Washington, U.S.A., 2006, pp. 518–522.

[89] A. A. Farid and S. Hranilovic, "Outage capacity optimization for free-space optical links with pointing errors," *IEEE Journal of Lightwave Technology*, vol. 25, pp. 1702–1710, July 2007.

[90] ——, "Optimization of beam width, bit error rate and availability for free-space optical links," in *Proceedings of the 6th International Symposium on Communication Systems, Networks and Digital Signal Processing*, Graz, Austria, 2008, pp. 92–96.

[91] ——, "Link reliability, range and rate optimization for free-space optical channels," in *Proceedings of the 9th International Conference on Telecommunications, ConTel*, Zagreb, Croatia, 2009.

[92] ——, "Capacity bounds for wireless optical intensity channels with Gaussian noise," *Submitted to IEEE Transactions on Information Theory*, Nov. 2007.

[93] ——, "Channel capacity and non-uniform signalling for free-space optical intensity channels," *to appear IEEE Journal on Selected Areas in Communications, Special issue on Wireless Optical Communication*, Jan.-April 2010.

[94] ——, "Capacity of optical intensity channels with peak and average power constraints," in *Proceedings of the IEEE International Conference on Communications*, Dresden, Germany, 2009.

[95] ——, "Design of non-uniform capacity-approaching signaling for optical wireless intensity channels," in *Proceedings of the IEEE International Symposium on Information Theory*, Toronto, Canada, 2008, pp. 2327–2331.

[96] H. Sandalidis, T. A. Tsiftsis, G. Karagiannidis, and M. Uysal, "BER performance of FSO links over strong atmospheric turbulence channels with pointing errors," *IEEE Communications Letters*, vol. 12, pp. 44–46, Jan. 2008.

[97] N. Letzepis and A. G. Fabregas, "Outage probability of the Gaussian MIMO free-space optical channel with PPM," *to appear in IEEE Transactions on Communications (accepted Nov. 2008).*

[98] X. He, "Bit-interleaved coded modulation for hybrid RF/FSO systems," Master's thesis, ECE, University of British Columbia, 2009.

[99] N. Letzepis and A. G. Fabregas, "Outage probability of the free-space optical channel with doubly stochastic scintillation," *to appear in IEEE Trans. Commun. (accepted Nov. 2008).*

[100] Y. Y. Sun, A. Consortini, and Z. P. Li, "A new method for measuring the outer scale of atmospheric turbulence," *Journal of Waves in Random and Complex Media*, vol. 17, pp. 1–8, Feb. 2007.

[101] A. Consortini and K. A. O'Donnell, "Measuring the inner scale of atmospheric turbulence by correlation of lateral displacements of thin parallel laser beams," *Journal of Waves in Random and Complex Media*, vol. 3, pp. 85–92, Apr. 1993.

[102] L. C. Andrews, R. L. Phillips, and C. Y. Hopen, "Aperture averaging of optical scintillations: Power fluctuations and the temporal spectum," *Waves Random Media*, vol. 10, pp. 53–70, Jan. 2000.

[103] J. H. Churnside, "Aperture averaging of optical scintillations in the turbulent atmosphere," vol. 30, pp. 1982–1994, May 1991.

[104] J. H. Churnside and R. J. Hill, "Probability density of itrradiance scintillations for strong path-integrated refractive turbulence," *Journal of Optical Society of America A*, vol. 4, pp. 727–733, Apr. 1987.

[105] J. G. Frehlich, "Log-amplitude covariance for waves propagating through very strong turbulence," *Journal of Optical Society of America A*, vol. 4, pp. 2158–2161, Nov. 1987.

[106] D. Bushuev and S. Arnon, "Analysis of the performance of a wireless optical multi-input to multi-output communication system," *Journal of Optical Society of America A*, vol. 23, pp. 1722–1730, July 2006.

[107] B. E. A. Saleh and M. C. Teich, *Fundamentals of Photonics.* New York: John Wiley, 1991.

[108] R. You and J. Kahn, "Capacity bound of optical IM/DD channels using multiple-subcarrier modulation with fixed bias," in *Proceedings of the IEEE International Conference on Communications*, Helsinki, Finland, 2001, pp. 2757–2762.

[109] U. Betke and M. Henk, "Intrinsic volumes and lattice points of crosspolytope," *Monatsh. Mathematik*, vol. 115, pp. 27–33, 1993.

[110] R. W. D. Nickalls, "A new approch to solving the cubic: Cardan's solution revealed," *The Math. Gazette*, vol. 77, pp. 354–359, 1993.

[111] MathWorks. (2009). [Online]. Available: http://www.mathworks.com/

[112] S. C. Chapara and R. P. Canale, *Numerical Methods for Engineering*, 5th ed. New York, USA: McGraw-Hill, 2006.

[113] A. C. Boucouvalas, "Iec 825-1 eye safety classification for some consumer electronics products," in *Proceedings of the IEEE colloquium on optical free space communication links*, IEEE savoy Place, London, Feb. 1996, pp. 13/1–13/6.

[114] R. Palanki, "On the capacity achieving distributions of some fading channels," in *40th Annual Allerton Conference Communication, Control, and Computing*, Monticello, IL, USA, Oct. 2002, pp. 337–346.

[115] R. Nuriyev and A. Anastasopoulos, "Capacity characterization for the noncoherent block independent AWGN channel," in *Proceedings of the IEEE International Symposium on Information Theory*, Yokohama, Japan, June 2003, p. 373.

[116] P. Hou, B. J. Belzer, and T. R. Fischer, "On the capacity of the paritially coherent additive white Gaussian noise channel," in *Proceedings of the IEEE International Symposium on Information Theory*, Yokohama, Japan, June 2003, p. 372.

[117] E. A. Ratzer, "Sparse data blocks and multi-user channels," Technical report, University of Cambridge, June 2002.

[118] M. Franceschini, G. Ferrari, and R. Raheli, "Does the performance of LDPC codes depend on the channel?" *IEEE Transactions on Communications*, vol. 54, pp. 2129–2132, Dec. 2006.

[119] R. Urbanke, "LDPC degree distribution optimizer for Gaussian channel," http://lthcwww.epfl.ch/research/ldpcopt/, 2009.

[120] S. Haas and J. H. Shapiro, "Capacity of wireless optical communications," *IEEE Journal on Selected Areas in Communications*, vol. 21, pp. 1346–1357, Oct. 2003.

[121] S. M. Haas and J. H. Shapiro, "Capacity of the multiple-input multiple-output poisson channel," in *Proceedings of the IEEE International Symposium on Information Theory*, Lausanne, Switzerland, June 2002, p. 169.

[122] X. Zhu, J. M. Kahn, and J. Wang, "Mitigation of turbulence-induced scintillation noise in free-space optical links using temporal-domain detection techniques," *IEEE Photonics Technology Letters*, vol. 15, pp. 623–625, Apr. 2003.

[123] L. C. Andrews, *Special Functions of Mathematics for Engineers.* New York, USA: McGraw-Hill, 1992.

[124] E. J. McCartney, *Optics of the Atmosphere.* New York: John Wiley & Sons, 1976.

[125] I. Korevaar, I. Kim, and B. McArthur, "Atmospheric propagation characteristics of highest importance to commercial free space optics," *Proceedings SPIE*, vol. 4976, pp. 1–12, Apr. 2003.

[126] I. Maxim Integrated Products, "Transimpedance amplifier MAX3744," http://www.maxim-ic.com, 2006.

[127] Communications Systems and Research Section, JPL, "Turbo codes," http://www331.jpl.nasa.gov/public/, 2006.

[128] T. J. Richardson, M. A. Shokrollahi, and R. L. Urbanke, "Design of capacity-approaching irregular low-density parity-check codes," *IEEE Transactions on Information Theory*, vol. 47, pp. 619–637, Feb. 2001.

[129] S. Lin and D. J. Costello, *Error Control Coding.* NJ. USA: Pearson Prentice Hall, 2004.

[130] I. B. Djordjevic, S. Sankaranarayanan, and B. Vasic, "Irregular low-density parity-check codes for long-haul optical communications," *IEEE Photonics Technology Letters*, vol. 16, pp. 338–340, Jan. 2004.

[131] ——, "Projective-plane iteratively decodable block codes for WDM high-speed long-haul transmission systems," *IEEE Journal of Lightwave Technology*, vol. 22, pp. 695–702, Mar. 2004.

[132] D. Divsalar, S. Dolinar, and C. Jones, "Low-rate LDPC codes with simple protograph structure," in *Proceedings of the IEEE International Symposium on Information Theory*, Adelaide, Australia, 4-9 Sept. 2005, pp. 1622–1626.

[133] T. Richardson and R. Urbanke, "The renaissance of Gallager's low-density parity-check codes," *IEEE Communications Magazine*, pp. 126–131, Aug. 2003.

[134] D. Borah and D. Voelz, "Pointing error effects on free space optical communication links in the presence of atmospheric turbulence," *Journal of Lightwave Technology. Accepted for publication.*

[135] H. Izadpanah, T. Elbatt, V. Kukshya, F. Dolezal, and B. K. Ryu, "High-availability free space optical and RF hybrid wireless networks," *IEEE Wireless Communications*, vol. 10, pp. 45–53, Apr. 2003.

[136] S. Vangala and H. Pishro-Nik, "Optimal hybrid RF-wireless optical communication for maximum efficiency and reliability," *Proc. IEEE Annu. Conf. Inform. Sci. Syst.*, pp. 684–689, 2007.

[137] E. Leitgeb, M. Gebhart, U. Birnbacher, W. Kogler, and P. Schrotter, "High availability of hybrid wireless networks," *In Proc. SPIE*, vol. 5465, pp. 238–249, Apr. 2004.

[138] M. N. Smadi, S. Ghosh, A. F. Farid, T. D. Todd, and S. Hranilovic, "Free-space optical gateway placement in hybrid wireless mesh networks," *Journal of Lightwave Technology*, vol. 27, pp. 2688–2697, 2009.

[139] P. Borjesson and C.-E. Sundberg, "Simple approximations of the error function Q(x) for communications applications," *IEEE Transactions on Communications*, vol. 27, pp. 639–643, Mar. 1979.

[140] L. Gordon, "A stochastic approach to the gamma function," *The American Mathematical Monthly*, vol. 101, no. 9, pp. 858–865, Nov. 1994.

[141] G. Strang, *Calculus.* Wellesley, MA, USA: Wellesley-Cambridge Press, Distributed by SIAM, 1991.

[142] B. Anderson, J. Jackson, and M. Sitharam, "Descartes' rule of signs revisited," *The American Mathematical Monthly*, vol. 105, no. 5, pp. 447–451, May 1998.